Universidade de Aveiro
2015
Departamento de Engenharia de Materiais e Cerâmica

Ensieh Seyedhosseini

Piezoeletricidade e Ferroeletricidade em Aminoácido Glicina

Piezoelectricity and Ferroelectricity in Amino Acid Glycine

Universidade de Aveiro
2015
Departamento de Engenharia de Materiais e Cerâmica

Ensieh Seyedhosseini

Piezoeletricidade e Ferroeletricidade em Aminoácido Glicina

Piezoelectricity and Ferroelectricity in Amino Acid Glycine

Tese apresentada à Universidade de Aveiro para cumprimento dos requisitos necessários à obtenção do grau de Doutor em nanociências e nanotecnologia, realizada sob a orientação científica do Dr. Andrei Kholkin, Investigador Coordenador do Departamento de Fisica e do CICECO da Universidade de Aveiro, e do Dr. Igor Bdikin, Investigador do Departamento de Engenharia Mecânica da Universidade de Aveiro.

Dissertation submitted to the University of Aveiro, as the fulfilment of necessary requirements for obtaining the Ph.D. degree in Nanoscience and Nanotechnology was carried out under the supervision of Dr. Andrei Kholkin, Research Coordinator of the Department of Physics and CICECO of the University of Aveiro and co-supervision of Dr. Igor Bdikin, Investigator of the Department of Mechanical Engineering of the University of Aveiro.

Bolsa de Doutoramento concedida pela Comissão Europeia no âmbito da Rede de Formação Inicial FP7 Marie Curie "Nanomotion".
(referência № 290158/2012)

Ph.D. scholarship granted by the European Commission within the FP7 Marie Curie Initial Training Network “Nanomotion”.
(reference № 290158/2012)

o júri

presidente

Professor Doutor Manuel João Senos Matias
Professor catedrático da Universidade de Aveiro

Professor Doutor José Ramiro Afonso Fernandes
Professor Auxiliar do Departamento de Física da Universidade de Trás-os-Montes e Alto Douro

Professor Doutor Joaquim Agostinho Gomes Moreira
Professor Auxiliar do Departamento de Física e Astronomia da Universidade do Porto

Professor Doutor Maria do Carmo Henriques Lança
Professora Auxiliar do Departamento de Ciência dos Materiais da Universidade Nova de Lisboa

Professor Doutor Vitor Brás de Sequeira Amaral
Professor catedrático do Departamento de Física da Universidade de Aveiro

Doutor Andrei Kholkin
Investigador Coordenador do Departamento de Física e do CICECO da Universidade de Aveiro

agradecimentos

First and foremost, I would like to express my sincere appreciation to my supervisor, Dr. Andrei Kholkin, for his advice, support and patience during the development of the work. His vast and deep knowledge as well as his consistent encouragement helped me overcome difficulties in my research. He provided innumerable guidance in every step of the way while gave me the freedom to develop my ideas. I consider it as a great opportunity to do my doctoral program under his supervision and to learn from his research expertise.

I am very grateful to my co-supervisor, Dr. Igor Bdikin, for his continuous help and numerous guidance throughout the work. He has generously given his time, knowledge and expertise in the field of PFM and general materials characterization all along these years.

A special thanks to Dr. Vladimir Bystrov for the valuable contributions and his kindness in sharing his knowledge. His expertise in Computational Modelling was of great help to a deeper understanding and better interpretation the experimental results.

I would like to thank Dr. Brian Rodriguez for the support, fruitful discussions and the valuable ideas he gave me during my stay at the University College Dublin.

The contribution of the members of the Prof. Vladimir Shur's group in Ural Federal University (Ekaterinburg) is gratefully acknowledged. My Particular thanks goes to Dr. Pavel Zelenovskiy for all the Raman Spectroscopy measurements and interpretations.

I would also like to thank the members of our research group, especially Dr. Maxim Ivanov, Dr. Svitlana Kopyl and Gonçalo Rodrigues for all their assistances.

Thanks to Dr. Dmitry Isakov and Prof. Nikolay Pertsev for the discussions and comments on the work.

I acknowledge the financial support from the European Commission within the FP7 Marie Curie Initial Training Network "Nanomotion" (grant agreement № 290158).

My deep gratitude goes to my parents, their continued encouragement and unconditional support drove me to move forward in my study.
Last but not least, thanks to my husband, Saeed who absolutely supported me every step of the way. Thank you for your understanding, patience and caring throughout the hard times of my work.

palavras-chave

piezoelectricidade, ferroelectricidade, biomateriais, aminoácidos, glicina, Microscopia de Piezo Força, domínios estruturais, ópticas não-lineares, modelação molecular

resumo

Piezo e ferroeléctricos biorgânicos são materiais que estão a atrair para si uma importância crescente por força da sua compatibilidade intrínseca com ambientes biológicos e uma biofuncionalidade aliada a um forte efeito piezoeléctrico e polarização controlada, a temperature ambiente. Aqui estudamos a piezo e ferroelectricidade no mais pequeno aminoácido, a glicina, representando uma ampla classe de aminoácidos nao-centrosimétricos.

A glicina é um elemento básico e extremamente importante em biologia, uma vez que serve de unidade base de construção para proteínas. Três formas polifórmicas com diferentes propriedades são possíveis na glicina (α, β e γ). De especial interesse para várias aplicações são as estruturas não-centrosimétricas: β-glycina e γ-glycina. A mais interessante β-polimorfa está a ser alvo de uma atenção reduzida, comparativamente às outras, por motivos de uma maior instabilidade a temperatura ambiente. Neste trabalho, Podemos crescer microcristais estáveis de glicina-β pela evaporação da solução aquosa num substrato (111)Pt/Ti/SiO_2/Si que funciona como "template". Os efeitos da concentração da solução e da nucleação Pt-assistida no crescimento do cristal e evolução da fase foram estudados com recurso à difracção Raio-X e espectroscopia Raman.

Adicionalmente, a técnica de "spin-coating" foi utilizada para a fabricação de nano-ilhas de glicina-β altamente alinhadas, com a orientação dos eixos cristalográficos normalizada pelo substrato de Pt.

Estudamos a indução de domínios estruturais por meio da ponta do AFM e a variação da polarização nos sistemas moleculares da β-glicina através da técnica PFM (Microscopia de Piezo Força), comparando os resultados obtidos com modelação molecular e simulações computacionais. Mostramos que a β-glycina é de facto um piezoeléctrico à temperatura ambiente e a polarização pode ser controlada por aplicação de uma tensão a cortes não polares. A dinâmica destes domínios complanares é estudada como função da tensão aplicada e duração do pulso. A forma do domínio é ditada pela polarização interna e externa, cujo rastreio é mediado por defeitos e características topográficas. A teoria termodinâmica é aplicada para explicar a propagação dos domínios induzidos pela ponta do AFM. As nossas descobertas sugerem que a β-glycina é um ferroeléctrico uniaxial com propriedades controladas pelas fronteiras dos domínios (electronicamente carregadas), que em seu turno podem ser manipuladas por tensão externa.

Adicionalmente, propriedades ópticas não-lineares da β-glycina foram investigadas por um método de segunda geração harmonica (SHG). Este método confirmou que a simetria axial é preservada em cristais crescidos sem pós-tratamento, reflectindo a esperada simetria $P2_1$ da fase β. A direcção da polarização espontânea mostrou ser paralela ao eixo monoclínico [010] e direccionada no comprimento do cristal. Estes dados foram confirmados por modelação computacional molecular. Medições ópticas revelaram também um valor relativamente elevado para a susceptabilidade óptica não-linear (50% maior que no quartzo com corte em z).

O pontencial uso de cristais de β-glycina estáveis em diversas aplicações são também discutidos.

keywords

piezoelectricity, ferroelectricity, biomaterials, amino acids, glycine, Piezoresponse Force Microscopy, domain structure, nonlinear optic, molecular modeling

abstract

Bioorganic ferroelectrics and piezoelectrics are becoming increasingly important in view of their intrinsic compatibility with biological environment and biofunctionality combined with strong piezoelectric effect and switchable polarization at room temperature. Here we study piezoelectricity and ferroelectricity in the smallest amino acid glycine, representing a broad class of non-centrosymmetric amino acids.

Glycine is one of the basic and important elements in biology, as it serves as a building block for proteins. Three polymorphic forms with different physical properties are possible in glycine (α, β and γ), Of special interest for various applications are non-centrosymmetric polymorphs: β-glycine and γ-glycine. The most useful β-polymorph being ferroelectric took much less attention than the other due to its instability under ambient conditions. In this work, we could grow stable microcrystals of β-glycine by the evaporation of aqueous solution on a (111)Pt/Ti/SiO_2/Si substrate as a template. The effects of the solution concentration and Pt-assisted nucleation on the crystal growth and phase evolution were characterized by X-ray diffraction analysis and Raman spectroscopy.

In addition, spin-coating technique was used for the fabrication of highly aligned nano-islands of β-glycine with regular orientation of the crystallographic axes relative the underlying substrate (Pt).

Further we study both as-grown and tip-induced domain structures and polarization switching in the β-glycine molecular systems by Piezoresponse Force Microscopy (PFM) and compare the results with molecular modeling and computer simulations. We show that β-glycine is indeed a room-temperature ferroelectric and polarization can be switched by applying a bias to non-polar cuts via a conducting tip of atomic force microscope (AFM). Dynamics of these in-plane domains is studied as a function of applied voltage and pulse duration. The domain shape is dictated by both internal and external polarization screening mediated by defects and topographic features. Thermodynamic theory is applied to explain the domain propagation induced by the AFM tip. Our findings suggest that β-glycine is a uniaxial ferroelectric with the properties controlled by the charged domain walls which in turn can be manipulated by external bias.

Besides, nonlinear optical properties of β-glycine were investigated by a second harmonic generation (SHG) method. SHG method confirmed that the 2-fold symmetry is preserved in as-grown crystals, thus reflecting the expected $P2_1$ symmetry of the β-phase. Spontaneous polarization direction is found to be parallel to the monoclinic [010] axis and directed along the crystal length. These data are confirmed by computational molecular modeling. Optical measurements revealed also relatively high values of the nonlinear optical susceptibility (50% greater than in the z-cut quartz).

The potential of using stable β-glycine crystals in various applications are discussed in this work.

Contents

List of Abbreviations and Symbols

SPM	Scanning probe microscopy
AFM	Atomic force microscopy
PFM	Piezoresponse force microscopy
VPFM	Vertical piezoresponse force microscopy
LPFM	Lateral piezoresponse force microscopy
MEMS	Miniaturized electromechanical systems
EFM	Electrostatic force microscopy
SHG	Second harmonic generation
PXRD	Powder X-ray diffraction
RH	Relative humidity
SAW	Surface acoustic wave
FRAM	Ferroelectric random access memory
BTO	Barium titanate
PZT	Lead zirconate titanate
TGS	Tri-glycine sulfate
$PbTiO_3$	Lead titanate
$LiNbO_3$	Lithium niobate
PVDF	Polyvinylidene fluoride
TrFE	Trifluoroethylene
CT	Charge-transfer
D	Donor
A	Acceptor
TTF	Tetrathiafulvalene
HS	High symmetry
LS	Low symmetry
Phz	Phenazine
PMDI	Pyromellitic diimide
DIPAC	Diisopropylammonium chloride
DIPAB	Diisopropylammonium bromide
KTP	Potassium titanyl phosphate
BPI	Betaine phosphite

GPI	Glycine phosphite
SAMs	Self-assembled monolayers
QPM	Quasi-phase-matching
HB	Hydrogen bonding
NLO	Nonlinear optical
DNA	Deoxyribonucleic acid
PF	Phase fingerprints
H_2ca	Chloranilic acid
H_2ba	Bromanilic acid
KH_2PO_4 (KDP)	Potassium dihydrogen phosphate
TTF-CA	Tetrathiafulvalene-chloranil
dabcoHReO4	1,4-diazabicyclo[2.2.2]octane perrhenate
[H-55dmbp][Hia]	5,5’-dimethyl-2,2’-bipyridine and iodanilic acid
ZnO	Zinc oxide
SBN	Strontium-barium niobate
IP	In-plane
OOP	Out-of-plane
P-E	Polarization-electric field
x-E	Strain-electric field
LDA	Local density approximation
PM3	Parameterized model number 3
UHF	Unrestricted Hartree-Fock
α, β, γ	Glycine phases
P_i	Total polarization
P_R	Remanent polarization
P_s	Spontaneous polarization
σ_{jk}	Stress tensor
d_{ijk}	Piezoelectric coefficients
S_{jk}	Strain tensor
E_i	Electric field
E_c	Coercive field
V^+	Forward coercive voltage
V^-	Reverse coercive voltage
V_c^+	Forward nucleation voltage

V_c^-	Reverse nucleation voltage
R_0^+	Forward remanent piezoresponse
R_0^-	Reverse remanent piezoresponse
R_s^+	Forward saturation piezoresponse
R_s^-	Reverse saturation piezoresponse
T_C	Curie temperature
T_0	Curie-Weiss temperature
ω	Frequency
θ	Diffraction angle
τ	Time
ϕ	Phase
A	Amplitude of piezoresponse
$A_{1\omega}$	Amplitude of the first harmonic piezoresponse
X, Y, Z	Directions
ε_0	Dielectric permittivity of the vacuum (8.85×10^{-12} F/m)
ε_{ij}	Dielectric permittivity
χ_{ijk}	Susceptibility tensor
$I^{2\omega}$	SHG Intensity
V	Volume of the unit cell
hkl	Miller indexes
a, *b*, *c*	Unit cell parameters
V	Voltage
ac	Alternative current
dc	Direct current
3D	Three dimensional
F	Crystal free Energy
$\emptyset_{tip}$	Tip potential
V_{tip}	Tip Voltage
Ω	Domain volume
γ	Domain surface energy density
U_{dw}	Self-energy of domain boundary
U_{dep}	Depolarizing field energy
W_{tip}	Work

r_{tip}	Tip radius
H	Tip height
L	Cantilever length
L	Domain length
W	Domain width
α	Polarizability
Q_y	Electrostriction coefficient
Pt	Platinum
Ti	Titanium
SiO_2	Silicon dioxide
Si	Silicon
P	Primitive
C	Cubic phase
(…)	Plane
[…]	Direction

Introduction

Creating artificial biomimetic materials with multiple functions similar to those of living bodies is an important frontier for advanced society in near future. Electromechanical coupling is one of the important functional properties of several classes of organic and bioorganic materials [1] and is one of the essential features of biological and living systems, in particular, regarding their electrical and mechanical signalization [2,3]. It is based on the complex dipolar properties and dipole-dipole interactions conjugated with hydrogen bonds network in biomolecular systems with different levels of self-assembly and hierarchy.

Recently, electromechanical coupling in various biomolecular structures (both crystalline and natural composites) based on important biological molecules has been observed and several materials have demonstrated functional properties similar to their inorganic counterparts, namely, sufficiently strong piezoelectricity and, furthermore, apparent ferroelectric-like behavior [4]. Understanding the relationship between the generated electric fields and applied mechanical stress is the main motivation for studying piezoelectricity in biological systems and artificial biomaterials. Since the early stage of investigation of biological piezoelectricity, researchers have proposed the undeniable role of electromechanics in the biological tissue development, in the movement of muscles and in the functioning of the nerve system of the body [5,6]. However, initial studies of biological systems have been performed on the macroscopic level, such as conventional electromechanical tests and dielectric measurements. Due to the complex hierarchical structure of these biomaterials, they provide only an averaged signal and quantitative piezoelectric measurements have not been unambiguously conducted.

Of further interest is that new bioorganic ferroelectric/piezoelectric materials have the potential to replace some traditional inorganic ones in practical devices, for example they can be used as natural biocompatible elements in medical implants, biosensors, bioelectronics, harvesting systems, MEMS, etc. [7].

In addition, in the last two decades, there has been an increasing application of ferroelectrics in miniaturized systems, pushing research towards size effects and nanoscale studies. It is therefore important to understand and to investigate ferroelectric properties down to the nanoscale. In this regard, the emergence of Piezoresponse Force Microscopy (PFM) offers a powerful tool to probe local piezoelectricity and ferroelectricity at the nanoscale [8]. PFM is a scanning probe technique based on the converse piezoelectric effect that is present in all ferroelectric materials. This technique allows both the detection and the

manipulation of the polarization state with a resolution down to 10 nm. It has been extensively used to study a variety of biological tissues, biopolymers and molecular crystals [7,9,10]. Using this technique, sophisticated domain structures have been imaged, domain switching characteristics have been determined, and biological ferroelectricity has been discovered [11,12].

In most studied examples of biomaterials, the presence of polar molecules and their inherent chirality are possibly the intrinsic reasons of electromechanical effects in them. Thus, a systematic way to understand the origin of this electromechanical coupling in a biomaterial is to study first the elementary blocks constituting a tissue rather than a complex biological system such as protein fibrils or even more deeply within the element structure of proteins (*i.e.*, amino acids).

It has been reported [13,14] that many amino acids have a non-centrosymmetric crystal structure and can be even ferroelectric when probed at small dimensions. Unfortunately, existing data on local electromechanical properties of amino acids is limited to experimental results obtained before the development of nanotechnological methods such as Atomic Force Microscopy (AFM) and its novel modes like PFM.

In order to understand the electromechanical properties of glycine molecules we need to study their properties using both macroscopic techniques such as X-ray, Raman scattering, non-linear optics, etc but also the local methods including Scanning Probe Microscopy such as AFM/EFM/PFM. These studies require well-defined structure rather than a complicated biological tissue. Furthermore for any application of them as a functional biomaterial in practical devices we need to investigate the relation between the functional properties and their three-dimensional polar structure. For these two reasons, the assembly of ordered molecules as a single crystal is preferable for our study.

Recent studies on the simplest amino acid glycine have demonstrated that it is a suitable material with apparent ferroelectric properties and square piezoresponse hysteresis loops at room temperature [15]. Glycine is one of the basic and important elements in biology as it serves as a building block for many biological macromolecules, such as peptides or proteins [16]. The main structural and physical properties of glycine crystals are reviewed and studied in this work, in particular in the context of their notable piezoelectric and ferroelectric properties.

Glycine can exists in three major polymorphic forms at ambient conditions: α, β and γ phases. From symmetry considerations, piezoelectricity can exist only in non-symmetric polar materials. It has been long time known that α-glycine crystals are centrosymmetric [17] and, therefore, do not exhibit any property described by the 3rd rank tensor such as piezoelectricity or second harmonic generation (SHG). On the contrary, γ- [18] and β-glycine [19] polymorphs are strongly non-centrosymmetric (with two differently formed and oriented by individual dipoles of each glycine molecules) and, therefore, can be used as a biocompatible nonlinear optical and piezoelectric/ferroelectric material [20,21].

The overall objective of this dissertation was first to develop a method of growing useful β- and γ-glycine crystals with well-defined shape and morphology from the solution and to investigate the conditions that affect the growth of crystals and polymorph selectivity. To achieve this goal, several synthesis methods were tried. A full set of the structural parameters of the crystal polymorphs was obtained in order to understand their electromechanical properties. Due to that, all the grown crystals were first characterized by the combination of structural characterization methods such as optical microscopy, X-ray diffraction (XRD), Raman spectroscopy and non-linear optical response.

The second objective was to investigate their electromechanical properties on the nano- and microscale level using PFM and characterize their domain structure and the switching properties so that to understand the microscopic mechanisms of their ferroelectricity.

Following this Introduction the present thesis is organized in six Chapters:

In Chapter 1, the fundamentals of piezoelectricity, ferroelectricity and domain structures are first presented and then followed by a short overview of the history and advances in studying these phenomena in biological materials and synthetic molecular ferroelectrics. The latest developments in molecular ferroelectrics revealed by PFM and the mechanism of ferroelectricity in molecular crystals are discussed. Then a brief overview of nonlinear optical phenomena, particularly in organic crystals is presented. Finally, this Chapter will end up with the description of the potential applications of organic ferroelectrics and possible opportunities for using them in specific devices in the near future.

In Chapter 2, the introduction to amino acids in general and piezoelectricity in crystalline amino acids is presented. Various crystal growth techniques useful for this work

are briefly mentioned. In particular, glycine polymorphism, possible crystal structures and crystallization processes to obtain α- , β- and γ-glycine are discussed.

In Chapter 3, the detailed description of the experimental techniques used for the characterization and phase determination of glycine crystals (including optical microscopy, X-ray diffraction and Raman spectroscopy) is given.

The basic principles and experimental setup of AFM are introduced, followed by a more detailed description of the relevant PFM mode. Then the experimental procedures employed for domain imaging and switching of polarization are described and quantitative analysis of the PFM signal is briefly discussed. Besides, the technique used for the second-order non-linear optical susceptibility measurement is presented.

The obtained experimental results are depicted, analyzed and discussed in the two following experimental Chapters.

In Chapter 4, several synthesis methods were applied to grow single crystals of all three phases of glycine (α-, β- and γ-polymorphs) from solution. The morphology and polymorphic forms of the crystals produced in these experiments have been analyzed by optical microscopy and X-ray diffraction. β-glycine was found to be unstable at normal ambient conditions and phase transition was detected using XRD. Therefore, a simple method of stabilization of the β-phase is introduced based on the evaporation of aqueous solution on crystalline Pt(111) substrates. As a result, we could grow sufficiently stable β-glycine microcrystals with well-defined habit and clear morphology on the commercial (111)Pt/Ti/SiO_2/Si substrates. X-ray diffraction analysis and Raman spectroscopy confirmed the preferential growth and stability of β-phase**.** The ability to grow stable β-phase crystals allowed studying their ferroelectric and nonlinear optical properties in detail in the following Chapter.

In Chapter 5, PFM technique was applied to probe the piezoelectric response and ferroelectric switching in both β- and γ-phases. The γ-glycine is found to be a purely piezoelectric (not ferroelectric) with a unique polar axis along the crystallographic c direction.

Further, PFM tip-induced domain structures and polarization switching in β-glycine were studied. We show that β-glycine is indeed a room-temperature ferroelectric and polarization can be switched by applying a *dc* bias to non-polar cuts via a conducting tip of AFM. Dynamics of these in-plane ferroelectric domains is studied as a function of applied

voltage and pulse duration. Non-linear thermodynamic theory is applied to explain the domain shape upon switching by the voltage applied to the tip of AFM. Our findings suggest that the ferroelectric properties of β-glycine are controlled by the charged domain walls which are in turn can be manipulated by external bias. Additionally, the pronounced decay of the switched domains was observed depending on the domain size.

Computational modelling of both β- and γ-phases was performed using a HyperChem 7/8 package and the importance of the network of the hydrogen bonds for the stability of glycine crystal structure is discussed. The developed molecular model and calculated physical parameters such as polarizability, saturated polarization, piezo- and electrostriction coefficient were found to be close to the obtained experimental data.

In addition, we show that the non-linear optical coefficients of β-glycine are comparable to those of reference z-cut (001) quartz. Highly anisotropic second harmonic generation signal is found to be compatible with the crystallographic symmetry of β-glycine. Biomolecular modelling is applied for understanding of the relationship between the crystal structure and nonlinear properties.

Chapter 6 concludes the thesis with a summary of the entire work carried out towards the objectives and outlines some potential directions for future developments.

Chapter 1

Introduction to Piezoelectricity and Ferroelectricity

This Chapter starts from the standard definitions of piezoelectricity, ferroelectricity, Curie temperature, polarization hysteresis and domain structure in general. Then the general property discussion is followed by the historical overview of the piezoelectric and ferroelectric features observed in biological materials. After that, recent developments in synthetic organic ferroelectrics including microscopic mechanisms governing ferroelectricity in these materials are reviewed. In addition, a brief overview of relevant nonlinear optical phenomena (mainly in organic crystals) is presented. Finally, current and future applications of organic ferroelectrics and their potential for emergent in devices are discussed.

1.1. Fundamentals of Piezoelectric and Ferroelectric Effects

Electromechanical coupling is one of the general characteristics of a wide range of inorganic and organic materials. The linear electromechanical coupling is called piezoelectricity. This property can be observed in non-centrosymmetric materials (in 20 of the 32 point groups) in which the application of mechanical stress results in electrical polarization (direct piezoelectric effect), while the application of an electric field results in a mechanical deformation (converse piezoelectric effect).

In both direct and converse piezoelectric effects there is a linear relation between the mechanical stress (strain) and electric polarization (field). The mathematical relations in the tensorial form can be expressed as:

$$\boldsymbol{P_i = d_{ijk}\,\sigma_{jk}} \quad \text{direct effect,} \tag{1.1}$$

and

$$\boldsymbol{S_{jk} = d_{ijk}\,E_i} \quad \text{inverse effect,} \tag{1.2}$$

where d_{ij} is the piezoelectric coefficient with the unit of m/V (or C/N), σ_{jk} is the stress tensor, P_i is the induced polarization, E_i is the applied electric field, and S_{jk} is the field induced strain tensor. Piezoelectric coefficients d_{ijk} are described by a 3^{rd}-rank tensor having maximum 18 components in triclinic crystals but with higher symmetry the number of independent components is reduced. The magnitude of the piezoelectric coefficient d_{ij} is affected by many factors including degree of crystallinity, degree of orientation (texture), existing domain

structure and intrinsic piezoelectric coefficients of a properly oriented monodomain single crystal [22,23].

Piezoelectric materials are used in a numerous number of devices, such as force and displacement sensors, electrically driven actuators and ultrasonic transducers [24,25]. Sensors make use of the direct piezoelectric effect that transforms mechanical signals into electrical response, *e.g.* to measure acceleration (accelerometers), pressure and acoustic vibrations. Actuators work *vice versa*, transforming electrical signals into mechanical responses and are used in various electrically driven actuators and force generators. Finally, in transducers both effects are used within the same device, *e.g.* in ultrasonic imaging systems.

Among the 20 piezoelectric crystal classes, there are ten pyroelectric groups with a unique polar axis, in which spontaneous polarization exists and varies with temperature. The spontaneous polarization is the average electric dipole moment per unit volume of the crystal. If such spontaneous polarization can be reversed by the application of an external electric field, then the pyroelectric material is called ferroelectric. Thus, all ferroelectrics are also pyroelectric and piezoelectric, although the opposite is not true. The spontaneous polarization of a ferroelectric material usually decreases upon heating and above a critical temperature which is called the Curie temperature T_c, the crystal phase becomes paraelectric with a non-polar structure. This property (temperature-dependent polarization) can be used in infrared detectors and thermal imaging systems [26]. The relative dielectric constant has a distinct maximum in the vicinity of the Curie temperature. Depending on whether the spontaneous polarization changes continuously or discontinuously at the Curie point, the phase transition can also be classified as second or first order [27,28].

As discussed above, main signature of ferroelectrics is the spontaneous polarization (P_s) of a ferroelectric crystal which can be reversed under the influence of a high enough external electric field. This process is called polarization switching. The critical electric field required to reverse polarization in ferroelectrics is called coercive field E_c, which also varies with the temperature, frequency and amplitude of the applied field. The switchability of the spontaneous polarizations causes the hysteretic relationship between the instant polarization P_s and the electric field E (Fig. 1.1a). This hysteretic dependence is called ferroelectric P-E hysteresis loop. The value of polarization at zero field is called the remnant polarization P_R. When the positive and negative coercive fields and remnant polarizations in both remnant states are equal to each other, the hysteresis loop is ideally symmetric relative to the P and E

axes. In reality, the loops are often asymmetric due to several factors including dissimilar electrodes, internal bias field due charged defects, inhomogeneous mechanical stresses, composition gradients across the thickness etc that can all affect the shape of the loop. In addition to the polarization-electric field hysteresis loop, polarization switching under electric field in ferroelectric materials leads to a strain-electric field hysteresis, which has a butterfly shape as shown in Fig. 1.1b [29].

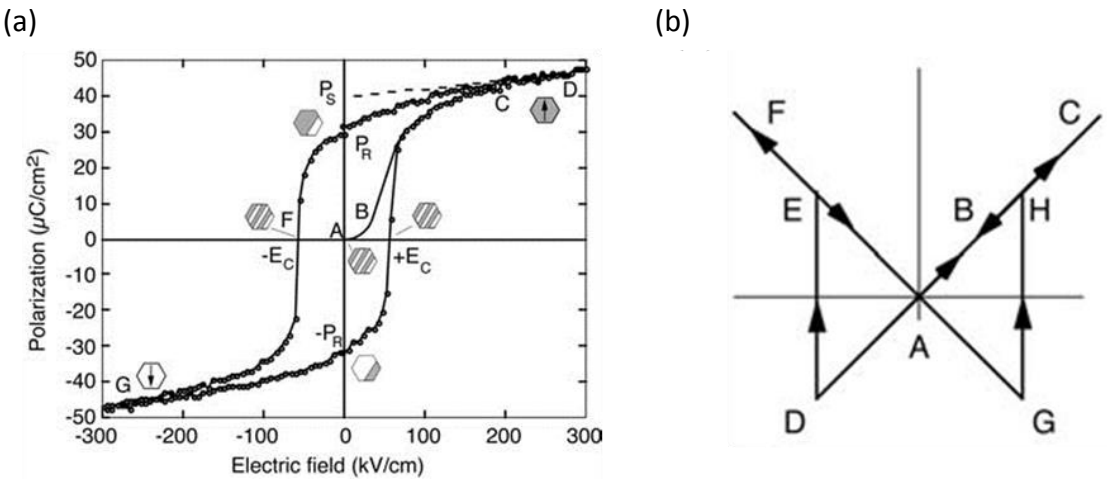

Figure 1.1. (a) Typical polarization-electric field (*P*-*E*) hysteresis loop in ferroelectric material and (b) Ideal strain-electric field (*x*-*E*) hysteresis (butterfly) loop in uniaxial ferroelectrics in which polarization reverses by 180° [29].

Ferroelectrics as multifunctional electroactive materials are suitable for a large number of applications [30] such as capacitors (especially for thin film capacitors due to large dielectric permittivities and small thickness) [31], electro-optic devices [32,33], surface acoustic wave (SAW) transducers [34], and non-volatile ferroelectric random access memories (FRAM) [35,36] in which the direction of the spontaneous polarization can be used to store information and the information bits are retained if the power is turned off.

Ferroelectricity was first observed in Rochelle salt crystal, containing organic tartrate ions [37]. For a while, Rochelle salt was the only known ferroelectric material. However, the rapid progress in ferroelectric field occurred only after the development of perovskite ferroelectrics such as barium titanate (BTO) [38] and lead zirconate titanate (PZT) families [39]. After some time, a few other molecular systems, such as well-known triglycine sulfate were discovered [40]. Today, among ferroelectric materials, the perovskite-type compounds,

particularly PZT, are the most studied and technologically are the most widely used due to their large piezoelectric coefficients and electromechanical coupling constants. However, they contain lead and it is a major environmental concern. Now considerable efforts were focused on searching lead-free alternatives of PZT. In addition, traditional piezoelectric ceramics are rigid, heavy, and require high temperature processing, which limits their application in certain areas.

In this context, in order to expand the range of applications of ferroelectric materials, molecular and bio-molecular ferroelectrics have been recently drawing much attention and a large number of organic ferroelectrics with properties comparable to perovskite oxides have been synthesized. They have several advantages including light weight, mechanical flexibility, non-toxicity, and low processing temperatures (*e.g.* by the solution growth). They are also environmentally friendly as they are do not contain lead and can be easily functionalized, *e.g.* for biosensor applications, which have motivated this perspective [7]. Intrinsic biocompatibility and the possibility of self-assembling are also fascinating properties of some molecular ferroelectrics which are made of biological building blocks.

Despite of many advantages, organic ferroelectric typically suffer from low spontaneous polarization, low transition temperature and weak piezoelectric properties even at low temperatures. Recent results on croconic acid [41] and disopropylammonium chloride (bromide) [42,43] have been indeed a breakthrough due to a combination of high enough transition temperature and polarization combined with low coercive field and switchability. These discoveries paved the way for using organic ferroelectrics in various applications.

In section 1-3 and 1-4, the progress and mechanism of ferroelectricity in biological tissue and synthesized molecular ferroelectrics, are explained in detail. In section 1-6 more details about the current and expected future applications of organic and biomolecular ferroelectric are discussed.

1.2. Ferroelectric Domains and Domain Walls

In general, ferroelectric crystal does not exhibit the same polarization orientation throughout the material. It can be divided into spatial regions with different directions of polarization, called ferroelectric domains. Each domain has uniform polarization and is separated by the domain walls. Domain walls are characterized by the angle between the

polarization directions on both sides of the wall. A number of technological applications of ferroelectrics such as nonlinear-optical and electro-optical devices are critically dependent on the ability to create controlled domain configurations in ferroelectric materials. Hence the understanding of domain formation, dynamics of domain wall motion, stabilization mechanisms, and structure of domain walls are of fundamental interest for the field of domain engineering and opens wide opportunities to optimize device performance.

In general, ferroelectric single crystals have a unique crystallographic orientation, but they may contain areas with uniform polarization directions called ferroelectric domains. They are oriented in a particular way to be compatible with crystallographic orientation and to minimize both electrostatic and mechanical energies. For example in $PbTiO_3$, six equivalent polarizations can be formed in the crystal depending on the stress and electric field conditions upon cooling. Ferroelectric polycrystals (ceramics) are composed of many individual grains with random crystallographic orientations which are in turn split into domains [44].

For platelet crystals domains with out-of-plane polarization are called **c** domains, while the domains with in-plane polarization are called **a** domains. Domain walls which separate two polar domains are called 180º domain walls if the angle between the polarization orientations of the neighboring domains is 180°; if the domains' polarization angle is not 180° – for example, they are 90º or 71º – they are called 90º or 71º domain walls, or generally, non-180º domain walls. 180º ferroelectric domain walls can be classified into three types according to the relative angle between the domain-wall plane and the polarization vector. One widely observed type is electrically neutral domain walls, which have a domain wall parallel to P inside the adjacent domains (Fig. 1.2). The other two types are head-to-head or tail-to-tail charged domain walls, where the domain wall plane is not parallel to P and hence positive or negative uncompensated bound charges are present at the domain wall (Fig 1.2). The mobility of charged and neutral domain walls under an electric field can be different. In conventional ferroelectrics, charged 180° domain walls are thermodynamically unstable because they are energetically unfavorable [45]. Consequently, charged domain walls have been rarely observed in ferroelectric materials such as $PbTiO_3$ crystals [46], PZT thin films [47] and, recently, in uniaxial organic ferroelectrics [48].

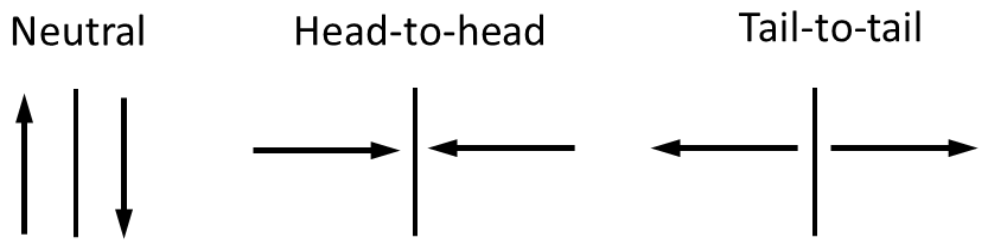

Figure 1.2. Three possible configurations for 180° domains. Orientation of spontaneous polarization with respect to the wall plane is shown by arrows [49].

1.3. Piezoelectricity and Ferroelectricity in Biomaterials

Piezoelectricity in biological materials was first observed and described by Fukada and Yasuda in 1957 [50]. They discovered both direct and converse piezoelectric effects in dry bone samples cut from the femur of man and ox. Piezoelectricity in bone was attributed to the collagen fibrils as an organic crystalline matrix. Collagen is a kind of protein and the polarization or the displacement of hydrogen bonds in the polypeptide chains of collagen crystal was suggested to be an origin of the observed piezoelectric effect [51]. After observation of piezoelectricity in collagen, piezoelectric effect has been also observed in a number of biological materials which contain molecular arrays of proteins or polysaccharides like tendons, muscles, teeth [52], exoskeletons [53], glands [54], nerve fibers [55], membrane protein [56], and cornea [57].

Soon after the discovery of biological piezoelectricity, pyroelectricity was observed in bone and tendon by Sidney Lang in 1966 [58] and, subsequently, in many other biological systems [59,60]. Later on, many authors claimed the existence of ferroelectricity in several biological materials. Fascinating theories were proposed regarding the functional role of ferroelectricity in voltage-dependent ion channels and biological membranes by Leuchtag [61,62]. He considered dielectric constant ε as a nonlinear function of electric field in the classical electrodiffusion model to explain the membrane function. He could fit the existing ion-channel data [63] with the Curie-Weiss law (apparent manifestation of ferroelectric phase transition) in biomembranes. Ermolina *et al.*[56] observed a liquid-crystal-like ferroelectric behavior in bacteriorhodopsin, an integral protein of the purple membrane of *Halobacterium salinarium*, embedded into the lipid biomembrane. Similarly, the Curie-Weiss law was found to be valid suggesting apparent ferroelectric-like behavior, the presence of a long-range order

in the regular positions of molecules and the symmetry loss at some critical temperature called Curie temperature [64]. All these phenomena are essential for various complex bio-objects but cannot be strictly called ferroelectric in a classical sense because of the variety of different mechanisms involved (due to, e.g., flexoelectricity in membranes or presence of water in bone). This makes the assignment of biological phenomena under electric field to ferroelectricity difficult, and sometimes speculative. The hindrance in ferroelectric hypothesis was also due to the fact that biological samples being soft could not endure the mechanical force required for electromechanical measurement and are subject to strong electrostatic effect. Another obstacle was the inability to look at the nanoscale to assign the observed complex electromechanical behavior to the particular structure unit and thus to understand the mechanism of the polar behavior and polarization reversal. Therefore, biological ferroelectricity remains elusive, and no direct experimental evidence has been presented until very recently.

During the last decade, rapid development of Scanning Probe Microscopy including Piezoresponse Force Microscopy (PFM) and Switching Spectroscopy PFM has led to the possibility of probing electromechanical properties of biomaterials along with their topography. The first study on biopiezoelectricity at the nanoscale was reported by Halperin *et al*. in bone [65]. Later both lateral and vertical piezoelectricity in tooth dentin and enamel were reported and it was revealed that dentin shows higher piezoelectricity with respect to enamel [66,67]. This behavior was attributed to the high fraction of piezoelectrically active protein components in dentin. Recently electromechanical properties of collagen fibrils [68,69], human nails [70] and also artificial biomaterials such as peptide nanotubes [71,72] have been studied with the nanoscale resolution via PFM.

The first indication of polarization switching under sufficiently high electric field in biological tissue, generally called bioferroelectricity was reported by Li and Zeng in shells [73,74,75] using PFM. After that bioferroelectricity was observed in the soft biological tissue; elastin protein of the aortic wall in mammals [76,77]. Therefore, the constituents of proteins such as amino acids, lipids and amyloid-like structures could be responsible for ferroelectricity in complex tissues. As such, apparent piezo- and ferroelectricity in these systems should be studied first to understand the global behavior of the complex biological systems. In this context, new materials class based on element structure of mentioned ferroelectric tissue such as crystalline amino acids (glycine), peptides (self-assembled

nanotubes) [71] and lipid/ferroelectric bilayers [78] have been synthesized. In-depth understanding of the electromechanical behavior in these structures under an applied electric field will open a pathway for further insight into the piezoelectric and ferroelectric phenomena in complex biological materials.

In addition to natural and synthetic biomaterials, organic molecular ferroelectrics with properties comparable to inorganic perovskite oxides have been synthesized [79]. The structure and microscopic mechanism of ferroelectricity in these materials are described in detail in the next section.

1.4. Structural Design and Mechanism of Ferroelectricity in Organic Molecular Crystals

The development of the organic ferroelectric had been quite slow since the discovery of ferroelectric effect [37]. However, recently a large number of organic ferroelectrics, mostly two-component and few single component molecular crystals have been synthesized. The microscopic mechanisms governing ferroelectricity in these organic ferroelectrics are usually attributed to order-disorder, displacive and proton-transfer types or mixed characteristics of these which are dependent on the design strategies. Ionic displacements in perovskite oxides have resulted in large spontaneous polarization and excellent piezoelectric and ferroelectric properties (Fig. 1.3). Such a mechanism is apparently less probable in molecular systems due to their large molecular volume and weaker bonds [80].

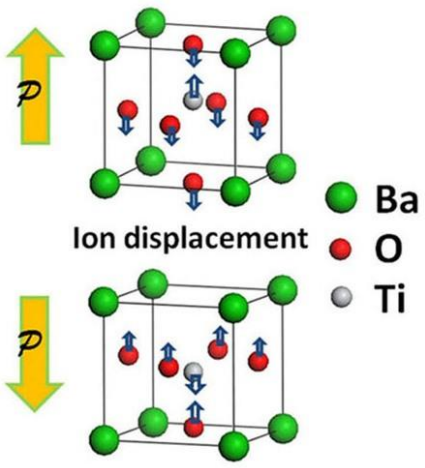

Figure 1.3. Polarization switching mechanism of a typical inorganic perovskite $BaTiO_3$ [81].

Most of the current literature on molecular ferroelectrics is divided into four categories:

The first and most simple possible design is that the permanent dipoles of the polar molecules such as thiourea [82], polyvinylidene fluoride (PVDF) polymer and co-polymers [83] generate spontaneous polarization in the organic solids, and the ferroelectric transition can arise from the reorientation of these polar components (Fig. 1.4).

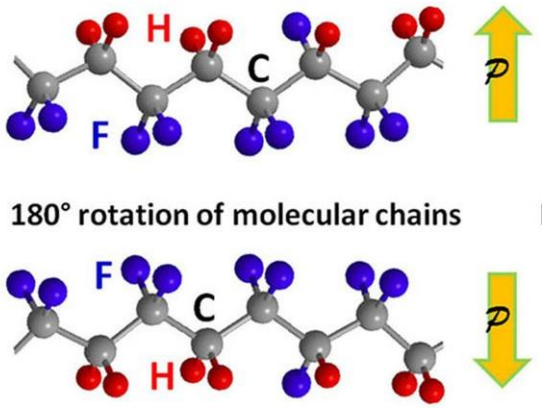

Figure 1.4. Schematic molecular structure and polarization switching of P(VDF-TrFE) polymer [81].

The second group developed from interaction between two nonpolar molecules such as donor and acceptor in a charge-transfer (CT) complex. Electrons can transfer between the donor (D) and acceptor (A) pairs through a neutral-to-ionic transition, which breaks the symmetry in the lattice and leads to forming dipolar DA dimers and polarization. As shown in Fig. 1.5 there can be two possible configurations with opposite polarity (DA DA… and AD AD...). Therefore, ferroelectricity of this polar structure mainly comes from the intermolecular charge transfer rather than from the displacement of point charge. Ferroelectric polarization of CT complexes under external electric field can be switched by the change of stacking style of A-D molecules, resulting in ionic displacement and charge redistribution to finally produce different polarizations (Fig. 1.6) [84].

One successful example of charge-transfer ferroelectric complexes is the tetrathiafulvalene-chloranil (TTF-CA), which demonstrates a distinct hysteresis loop with a large remnant polarization of 6.3 $\mu C/cm^2$ [85]. These co-crystals normally have higher polarization, ferroelectricity at low temperature, first-order ferroelectric phase transition and

large dielectric constant [79]. However, the charge-transfer complexes have some problems, such as current leakage. Because most of these CT complexes are semiconductors, the neutral to ionic transition requires a narrow charge gap which may lead to current leakage and degradation of the spontaneous polarization [86].

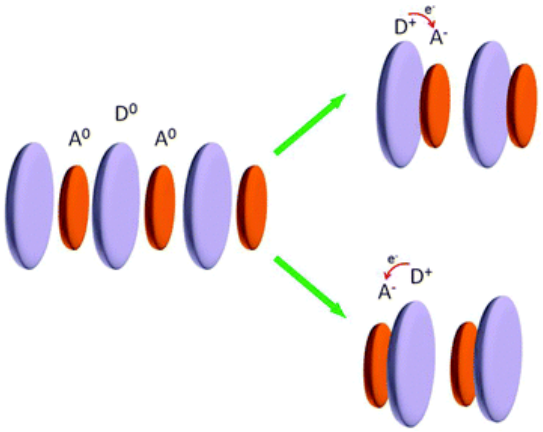

Figure 1.5. Schematics of neutral-to-ionic transition in the charge transfer complex with two possible polarities [86].

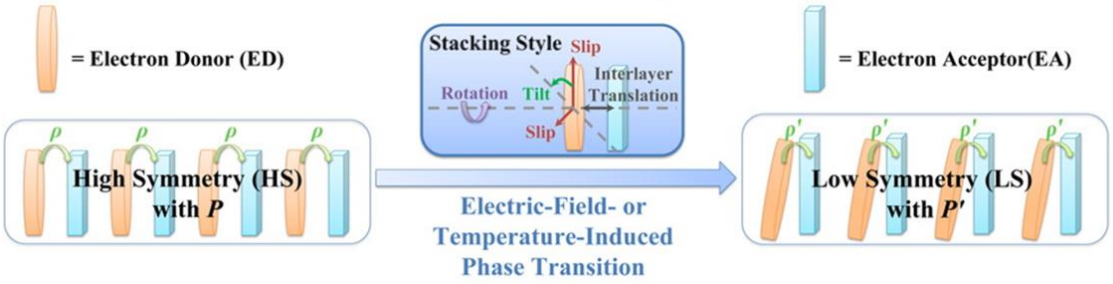

Figure 1.6. Schematic representation of electric field- or temperature- induced ferroelectric switching of charge-transfer complexes between different phases (HS versus LS phases) [84].

The third strategy to obtain organic ferroelectrics is to utilize proton dynamics in hydrogen bonds to contribute to ferroelectric properties. There exist two types of hydrogen bond ferroelectricity: displacive and proton-transfer. In the displacive type, the molecules do not necessarily have permanent dipoles, but the crystal polarization comes from relative displacement of protons in the crystal through intermolecular interaction. Horiuchi *et al.* synthesized two-component molecular ferroelectrics connected by hydrogen bonds to form a

co-crystal with large spontaneous polarizations at room temperature [87], such as nonpolar co-crystals made of phenazine (Phz) with proton accepting nitrogen atoms and chloranilic acid (H_2ca) or bromanilic acid (H_2ba) with proton donation O–H groups (Fig. 1.7a) [88].

Above the Curie temperature, all the hydrogen bonds have equal lengths and the net dipole moment is therefore zero. Below the Curie temperature, the polarization of co-crystal is determined by the displacement of hydrogen atoms on one side of the H_2ca acid molecule toward the nitrogen atom of phenazine while the other side remains almost unchanged (Fig. 1.7b,c). Therefore, ferroelectricity originates from an asymmetric O–H bond elongation of the intermolecular O–H…N bonds and the relative molecular displacement as drawn schematically in Fig. 1.7d. These co-crystals have a first-order ferroelectric phase transition, high dielectric permittivity, and high resistivity [88].

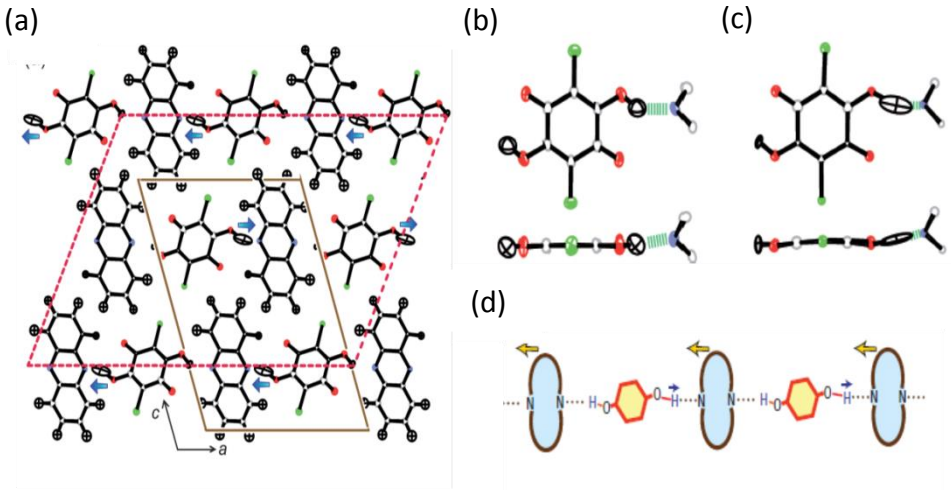

Figure 1.7. a) Crystal structures of a-Phz–H_2ca in the b-axis projections. b,c) Molecular structures of H_2ba in paraelectric and ferroelectric phase. d) Schematic of alternating acid–base molecules with intermolecular hydrogen bonds in every chain. Blue and yellow arrows indicate the displacement directions of proton and the molecules in the ferroelectric phase, respectively [89].

In the second type observed in early ferroelectrics, proton transfer is important as was proved in Rochelle salt [37] and inorganic potassium dihydrogen phosphate KH_2PO_4 (KDP). In the KDP family, the collective site-to-site transfer of protons in the O–H…O bonds, between PO_4^{3-} ions switches the spontaneous polarization (Fig. 1.8) [90].

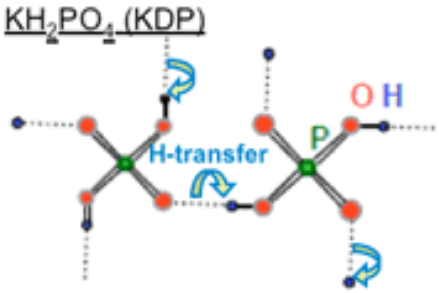

Figure 1.8. Protons transfer in the O–H…O bonds of KH_2PO_4.

Similar proton dynamics have been observed in co-crystals of [H-55dmbp][Hia] [91], and the strong hydrogen bonding suggests possible tautomerism that transforms the O–H…N bonds into the ionic with O^-…H–N^+ form and simultaneously changes the p-electron molecular geometry.

Recently this strategy was also demonstrated in a number of organic single-component low molecular-mass crystals which all have proton donor and acceptor moieties to bind molecules into a dipolar chain. For example a room temperature polarization of 20 $\mu C/cm^2$ and ferroelectric stability up to 130°C was reported in croconic acid which is the highest value among the low-molecular-weight organic ferroelectrics [41]. In the crystal structure, molecules are arranged in two-dimensional sheets, and each one can transfer two protons from hydroxyl groups to the carbonyl groups of adjacent molecule during the polarization switching by an external electric field (Fig. 1.9a,b). Therefore, ferroelectric switching is attributed to the collective proton ordering in intermolecular hydrogen bonds through proton tautomerism on O_H…O bonds. In comparison with bulk molecule rotation, moving protons only within the hydrogen bond would be generally advantageous in minimizing steric hindrance for polarization reversal and decrease the coercive field.

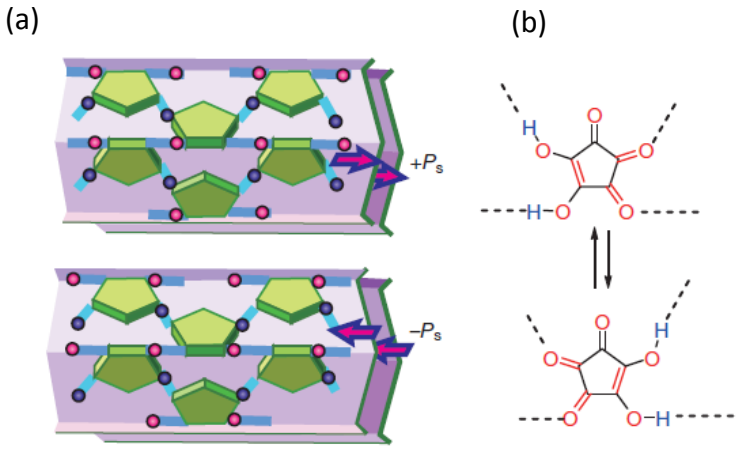

Figure 1.9. a) Schematic illustration of hydrogen-bonded sheets in croconic acid crystal. The arrows show the electric polarity of each sheet. b) Change of chemical-structure polarity through the p-bond switching and intermolecular proton-transfer processes [41].

In this category, room-temperature ferroelectricity and antiferroelectricity was revealed in benzimidazole derivatives, a hydrogen-bonded ferroelectric made of imidazole unit, which are biological building blocks [92] with polarization of 5 to 10 μC/cm^2. Its proton donor and acceptor moieties easily bind molecules into a dipolar chain, which is often bistable in polarity due to the amphoteric nature of the molecules. Ferroelectric polarization can be switched through proton dynamics on N_H…N bond as shown in Fig. 1.10.

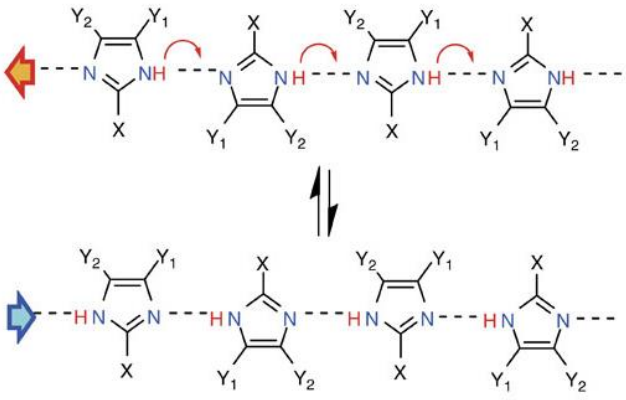

Figure 1.10. Hydrogen bonding (broken lines) and polarization reversal mechanism through the proton tautomerism of the imidazole moiety [92].

In addition, Tayi and coworkers [93] recently synthesized the hydrogen-bonded CT complexes between a pyromellitic diimide (PMDI)-based acceptor and three donors that are derivatives of naphthalene, pyrene and TTF. These polar and switchable systems incorporate both the advantageous features of proton dynamics mechanism and charge-transfer process of organic ferroelectrics. They possess room-temperature ferroelectricity and clear hysteresis loop was observed in all three complexes at 300 K with remnant polarization exceeding 1 μC/cm^2. At low temperature, the polarization for PMDI-TTF was found to be as large as 55 μC/cm^2 which is the highest among known molecular systems. This molecular structure retains its properties up to 153 °C.

The fourth approach is to utilize the disorder-order of atomic position in each single molecule, resulting in an asymmetric structure. This ferroelectric mechanism has been discovered recently in two simple diisopropylammonium (DIPA) salts, DIPA chloride (DIPAC) [42] and DIPA bromide (DIPAB) [43]. DIPAC shows a spontaneous polarization of 8.9 μC/cm^2 and a T_c of 440 K, and DIPAB has a large polarization of 23 μC/cm^2 and a T_c of 426 K, comparable to that of barium titanate. Their ferroelectricity is believed to arise from the order-disorder behavior of N atoms. DIPAB demonstrates a large dielectric constant and a low dielectric loss at room temperature, in addition to its excellent ferroelectric properties. All these features open the pathway for practical applications for them to substitute the traditional perovskite ferroelectrics.

Most of organic ferroelectrics have high optical transparency and large nonlinear response with respect to the electromagnetic radiation in the optical range. Therefore, they have potential application in various nonlinear-optical devices. In the following section a brief discussion of these phenomena and their advantage in organic ferroelectrics is presented.

1.5. Nonlinear Optical Properties of Ferroelectric Materials

Nonlinear optics is a phenomenon arising from the interactions of optical radiation with materials to yield new optical wave in a nonlinear way. In recent years, domain engineering was focused on the fabrication of periodic ferroelectric domain structures with desirable parameters for the manufacturing of devices. Engineerable nonlinear optical materials have permitted the development of a wide range of tunable coherent light sources

based on quasi-phase-matching (QPM), causing a great deal of interest in view of their potential applications in the areas of laser technology, photonic devices, high density data storage technology and optical interconnects [94,95].

The effect of the electric field vector *E* of the incoming light is to polarize the material. This polarization can be calculated using the following relation:

$$\vec{\boldsymbol{P}} = \varepsilon_0 \chi^{(1)}.\vec{\boldsymbol{E}} + \chi^{(2)}.\vec{\boldsymbol{E}}.\vec{\boldsymbol{E}} + \chi^{(3)}.\vec{\boldsymbol{E}}.\vec{\boldsymbol{E}}.\vec{\boldsymbol{E}} + \dots , \qquad (1.3)$$

where ε_0 is the free-space permittivity and $\chi^{(1)}$, $\chi^{(2)}$, $\chi^{(3)}$ are the first order (linear), second order (nonlinear) and third order (nonlinear) susceptibility tensors, respectively. Usually the second order processes are much more important in magnitude than those of higher orders for the moderate electric field commonly present in the materials. Second harmonic generation (SHG), in particular, corresponds to the appearance of a frequency component that is exactly twice that of the input light. SHG was discovered by Franken *et al*. in 1961 just after the development of intense laser sources [96]. Since then this process has become very important for many applications, such as frequency doublers, frequency converters, electro-optic modulators and nonlinear optical microscopy. The majority of the early nonlinear optical materials were based on inorganic crystals, such as potassium dihydrogen phosphate (KDP), lithium niobate ($LiNbO_3$) [97], potassium titanyl phosphate (KTP) etc. [98]. They have large electro-optical and nonlinear optical coefficients and desirable properties for materials applications, including good mechanical properties, high optical damage threshold and the fact that they can be grown as large crystals. However, inorganic materials have important drawbacks such as the "trade-off" problem between response time and magnitude of optical nonlinearity. Moreover, they have problems with optical quality because of the strong absorption in the visible region. This is deleterious for many possible applications.

An important development in nonlinear optical materials occurred in 1970, when Davydov *et al*. reported a strong second-order NLO effects in organic molecules having electron donor and acceptor groups connected with a benzene ring. This discovery led to an entirely new concept of molecular engineering to synthesize new organic materials for the SHG studies. However, very few materials have been studied for this purpose yet potentially there are innumerable organic substances to choose from.

Molecular compounds have received intense interest due to their larger NLO efficiencies and large amount of design flexibility. Furthermore, they show extremely fast response to external electric fields as compared to their inorganic counterparts [99]. The drawback of organic materials is that they often have lower thermal and photochemical stability.

1.6. Current Applications of Organic Ferroelectrics and Future Prospects

Despite the good progress made recently in the organic-ferroelectrics materials, continuous research is needed to better understand molecular mechanism and to improve the performance of molecular ferroelectrics in order to gradually replace them with inorganic materials in devices.

Nowadays, the most widely used organic ferroelectrics are VDF based polymers and their oligomers. PVDF has such unique properties as flexibility, ruggedness, low acoustic impedance and availability as thin films, but a somewhat smaller electromechanical coupling factor. They found numerous applications as non-volatile memory devices [100], opto-electronic memories [101], biomedical sensors [102], capacitors [103] and nanogenerators that convert natural vibrations to electricity by harvesting energy from the movement of the human arm [104] or from respiration [105].

Another example, biologically compatible harvesting elements were created based on 1,4-diazabicyclo[2.2.2]octane perrhenate (dabcoHReO$_4$) ferroelectric microcrystals embedded in the polymer fibers by electrospinning [106].

However, these materials represent a relatively narrow class of synthetic organic crystals with a limited variability of the physical properties and unknown biocompatibility. Apparently, new materials classes based on natural tissue components such as aminoacids, peptides or lipids should be explored in view of their natural biocompatibility and variability [107].

We expect that newly developed molecular ferroelectrics will open novel perspectives for the applications. They offer great opportunities for the development of a new generation of natural piezoelectric materials and nano-devices that could be implanted in the human body (in vivo), as a bio-memory for storing programs to deliver drugs or as a nanocatalyst for controlling chemical reaction because ferroelectric domain orientation affects the chemical

reactivity of the surface in adsorption, catalytic and photochemical processes. In addition, the lower coercive field required for reverse polarization compared to organic polymers could lead to a significant breakthrough in computer memory technology and to reduce its electrical power demands.

Of even greater interest is the direct use of ferroelectric tissues instating implanted molecular ferroelectric devices. For example, it may be possible to monitor the natural polarization state of the biological system for early diagnosis and to manipulate with its polarization states as new ways of fighting disease [7].

Chapter 2

Amino Acids Crystals

This Chapter starts with the explanation of importance of amino acids in living systems and introduction to their piezoelectric properties. The basic principles of crystallization and various crystal growth techniques with emphasis on evaporation from solution are introduced. The process of nucleation (including homogeneous and heterogeneous nucleation) and growth of the crystals is discussed. After the overview of the relevant literature on glycine polymorphs (α, β and γ), their relative stabilities and growth methods for all polymorphs with the focus on the β-glycine will be presented.

2.1. Amino Acids

Amino acids are organic compound with the general formula $HCCO_2^-NH_3^+R$, where R is a lateral chain characteristic of each molecule. Amino acids are extremely important in biochemistry, nutrition, neurology, psychiatry, pharmacology, nephrology, and gastroenterology. One particularly important function is to serve as the building blocks of proteins of all living beings, which are chains of amino acids. Each protein has its own unique amino acid sequence that is specified by the nucleotide sequence of the gene encoding in the deoxyribonucleic acid (DNA) molecule. As such, amino acids play a fundamental role in physiology, origin and evolution of life. Among their properties as life-coordinating molecules, the chemical and catalytic ones were the most studied up to now. There are twenty different amino acids and most of them can also exist with a highly ordered crystal structure in the solid phase, due to their inherent self-assembly and molecular-recognition capabilities. Single crystals of all the primary amino acids can be grown from an aqueous (or other) solution. Crystalline amino acids belong to the family of hydrogen-bonded crystals. Hydrogen bonding (HB) interactions play an essential role in their crystal structure and present complex networks of HB create different crystalline polymorphs [108]. Polymorphism is the ability of crystalline materials to exist in different molecular packing yet with the same chemical compositions. Polymorphs can have different mechanical, thermal, and physical properties [109].

In solution, most amino acids are in the zwitterionic form in which the amino group is represented as $-NH_3^+$, and carboxyl as $-COO^-$. In such a bipolar form there is significant molecular dipole moment, then continuing in the crystalline form. From a crystallographic point of view, molecular crystals formed from amino acids are a class of polar materials and

the majority of them have non-centrosymmetric crystal structures. This means that they are potentially piezoelectric, pyroelectric with nonlinear optical properties and, possibly, ferroelectric [14,110].

In some cases, inorganic derivatives of amino acids such as amino acid sulphate and phosphate salts have shown ferroelectric behavior. For instance, triglycine sulphate (TGS) is a salt of glycine with inorganic counterion ($(CH_2NH_2COOH)_3\ H_2SO_4$) and is known for room temperature ferroelectricity (P_s = 3.8 μC/cm^2, $T_c \approx 50$ °C) [40]. Semiorganic TGS family has excellent pyroelectric properties and second order phase transition of order-disorder type. Other examples are betaine phosphite (BPI) and glycine phosphite (GPI). Typically amino acids with inorganic compounds have better mechanical and thermal properties relative to the purely organic amino acids.

Lemanov *et al*. investigated piezoelectricity in pure amino acids crystals in respect to the temperature dependence of ultrasonic properties. He found that γ-glycine and DL-alanine are the strongest amino acid piezoelectrics (comparable to, or even stronger than quartz crystals). L-alanine, L-valine, L-glutamic and DL-tyrosine possess much weaker piezoelectric activity [14,110,111].

2.2. Crystal Growth Techniques and Principles of Crystallization

Crystal growth techniques are classified into three main categories: growth from solutions, from melts and from vapor phases. The choice of a particular crystal growth method depends on the material to be crystallized, its quality, size, growth rate, its physical and chemical properties in particular and the nature of the method.

In general, solution growth is simple and inexpensive. Amino acid crystals are typically grown from the solution. Crystallization from the solution has two stages: nucleation and growth. Nucleation is the formation of a new solid phase from a supersaturated mother phase. In the nucleation step, three important concepts are critical nucleus, homogeneous and heterogeneous nucleation. In supersaturated homogeneous systems, nuclei can appear once sufficient supersaturation has been generated to overcome the energy barrier for nucleation and when sufficient time has passed for critical sized clusters to form, crystallization begins. Heterogeneous nucleation involves the nucleation on the substrate, in the presence of impurity particles in the medium, on the wall of a

crystallizer, etc. All of them serve as the catalytic agents for the process of nucleation of the new phase. Therefore, activation energy for heterogeneous nucleation is lower than that for homogeneous nucleation and, under the same temperature and pressure conditions, heterogeneous nucleation occurs at lower supersaturation than homogeneous nucleation [112].

Nucleation is followed by the crystal growth, which is the process of further addition and integration of growth units to the existing nuclei/crystals. Both crystal nucleation and growth occur in supersaturated solution but the supersaturation level requirements for nucleation and crystal growth are different. There are many methods to achieve this supersaturation on which the crystallization technique depends [113]. Amino acid crystals can be produced by different methods from the solution. The slow evaporation of a solution is the simplest method to grow crystals [114]. Other commonly used techniques include slow cooling of the solution, solvent diffusion, vapor diffusion, sublimation and many variations of these. The choice of the technique is dictated by the necessary size of the sample. From the above mentioned methods, slow evaporation from solution and droplet evaporation on the crystalline substrate was used for the crystallization of glycine in this work.

Droplet evaporation offers some advantages such as a reduction in production steps when compared to traditional crystallizations; however, it is sometimes difficult to control and to model the product properties because of flow patterns of the droplets and following irreproducibility [115]. Droplet evaporation has been used in various self-assemblies. In this method, evaporation increases the level of concentration gradually to produce supersaturation and induce crystallization. The volume of the initial droplet, concentration of the solution, interaction between molecules and substrate and environmental conditions such as temperature, relative humidity, hydrophilicity-hydrophobicity of the substrate and external pressure all influence the size and quality of the resulting crystals. As mentioned above, crystallization on the substrate is an inhomogeneous nucleation and growth since the evaporation rate at the droplet edge is higher than that inside. Fast evaporation at the edges of a droplet results in a flow directed from within the droplet towards the edges. This flow carries molecules with it, and these molecules are deposited at the boundary of the droplet. After that, the molecules inside the droplet contribute to the crystal growth [116].

2.3. Glycine Polymorphs

In our work, among the 20 natural amino acids, glycine has been selected because it has significant piezoelectricity at room temperature and it has recently shown ferroelectric properties [15] and thus presents significant interest for biomedical and electronic applications. Glycine is the simplest amino acid and is widely used as an excipient for proteins and pharmaceutical reagents production [117]. It has been also recognized as the symbolic origin of life based on its presence in extraterrestrial objects [118]. In the gaseous state glycine exists in non-ionic form, whereas in solution and in crystalline state it is in the form of the zwitter ion [119]. Figure 2.1 shows the structure of glycine molecule in the zwitterionic form.

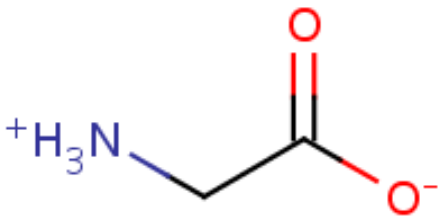

Figure 2.1. Glycine structure

Glycine as a classical polymorphic material exists in three major polymorphic forms at ambient conditions: α, β and γ phases [120] and under some extreme conditions other metastable phases were also obtained [121]. The polymorphs of glycine differ in the packing arrangement of the $+NH_3$-CH_2-COO- zwitterions via a hydrogen-bond network between them. It has been found that the bulk glycine polymorphs display different thermodynamic stability (in the order of γ > α > β) and different crystal symmetries based on different zwitterion packing during growth. γ-polymorph is thermodynamically the most stable form of glycine, α-glycine is the metastable form and β is the least stable phase under ambient conditions. However, metastable α and β polymorphs can be preserved in a dry atmosphere for a long time because they have large enough kinetic barriers for transformation. Under humid NH_3 vapor, α-phase typically converts into the γ-polymorph [122]. The β-polymorph irreversibly transforms into α or γ forms in the presence of a humid air, under increasing temperature, in the presence of NH_3, or under grinding. This transformation appears by the loss of transparency of the crystals [123,124].

Structural peculiarities and physical properties of these glycine polymorphs have been considered in a lot of publications, especially as pharmaceutical reagents since different molecular self-assemblies in the solid state can affect drug performance, bioavailability and safety. Thus a complete characterization of all possible polymorphs is considered as an essential step in pharmaceutical industry to choose the best drug formulation with desirable properties [125]. However, there have been only a few attempts carried out to study the piezoelectric properties of these materials. The physical arrangement and hydrogen bonds of the molecules within the unit cell are responsible for the ferroelectric and dielectric properties of the materials. In the following, the molecular structure of glycine polymorphs (α, β and γ), their relative stabilities and growth methods for each polymorph will be discussed.

α-glycine Structure and Crystal Growth Methods

The structure of α-glycine was first investigated by Albrecht and Corey and later by Marsh [17,126]. The centrosymmetric α-glycine easily crystallizes from saturated pure aqueous solution with evaporation [114]. In the α-polymorph, glycine dimers are linked by hydrogen bonds in double antiparallel layers and the layers are connected together by Van der Waals interaction. Formed crystals usually have bipyramid morphology with monoclinic crystal structure and centrosymmetric space group ($P2_1/n$, Z = 4). From a thermodynamic point of view α- phase is less stable than the γ-phase, but there are no phase transitions at room temperature. Therefore, its transition to the γ-phase should be prohibited kinetically [119,127].

β-glycine Structure and Crystal Growth Methods

β-glycine was first reported by Fisher in 1905, and the structure was investigated later by Bernal and Iitaka [19,128]. To induce crystallization of the β- or γ-polymorphs, zwitterionic glycine monomers are necessary as building units rather than cyclic dimers. In the β-polymorph, single polar layers create a monoclinic structure similar to the α-phase but with a non-centrosymmetric space group ($P2_1$, Z = 2) [129].

The β-polymorph of glycine was mostly crystallized by adding antisolvent (either an alcohol or acetone) to a concentrated solution of glycine [19,130,131]. Other used techniques were spray-drying [132] and freeze-drying [133,134]. However, the obtained crystals were frequently unstable under ambient conditions, and rapid conversion into a more stable α-

phase was observed in this material [19,132]. Moreover, some of these methods did not lead to the pronounced habit with the well-defined shape, and the grown β-glycine was only present as a mixture with α-crystals. Due to these limitations there are only a few reports on the physical properties of β-glycine.

There were a few attempts to stabilize the useful β-phase under ambient conditions. For instance, Hamilton *et al*. [135] obtained stable nanocrystals of β-glycine embedded in nanometer-scale channels. They found that the nanocrystals grown within the channels of pore diameters less than 24 nm persist for at least one year against transformation to other forms and transform slowly to α-glycine over several days if grown within bigger pore diameters. In another paper, Lee *et al*. [136,137] studied the effect of the substrate on the polymorph selectivity of glycine. They obtained all three polymorphs of glycine on a patterned substrate with self-assembled monolayers (SAMs) consisting of hydrophilic gold islands surrounded by hydrophobic domains. According to their result, the main crystals phase (in a natural aqueous solution) was the α-phase and the frequency of β-glycine appearance increased for smaller metallic islands and under reducing concentrations. This result was important to understand that the preferential growth of β-glycine can be mediated by using an appropriate substrate that can accelerate the nucleation and further growth of the desired phase.

γ-glycine Structure and Crystal Growth Methods

γ-glycine was first obtained by Iitaka [18]. The crystal structure of γ-glycine is essentially different. The zwitterions are organized in triple helices around the 3_1 screw-axis which are linked together by lateral hydrogen bonds and form a three dimensional network. The crystal structure of γ-glycine belongs to the hexagonal non-centrosymmetric space group $P3_1$ or $P3_2$ with three molecules in the unit cell.

If the formation of the dimers in solution, and the growth of the α-polymorph, is inhibited, then the stable γ-polymorph grows under crystallization conditions closer to equilibrium (slow crystallization), whereas very quick precipitation gives the β-polymorph [120].

In prior studies it was reported that γ-glycine crystals can be obtained by changing the solutions pH [137], by adding special salts (such as sodium chloride, potassium chloride, ammonium chloride, lithium bromide) to glycine solution [138,139,140] or addition of a

tailor-made additive [141]. The additive does not interfere with the crystal structure; it influences nucleation and growth kinetics. γ-phase crystals also can be created by exposing the supersaturated aqueous glycine to an electric field [142], or using irradiation with polarized laser light [143,144]. These may promote crystallization of the γ form through the arrangement of monomers in a head-to-tail orientation along the polar c-axis of crystal.

Recently, Guangwen He *et al*. grew γ-glycine crystals from neutral aqueous solutions through slow evaporation of water using an evaporation-based crystallization platform [145], because a slow evaporation process allows the molecules to be arranged in the lowest energy state during the formation of nuclei. However, the resulting crystals did not have any preferred orientation and shape and agglomerated together.

Chapter 3

Experimental Techniques

A variety of techniques are available to characterize the polymorphic phases of glycine. In this Chapter, the description of the experimental techniques used for the characterization and phase determination of glycine crystals are introduced.

Also, after presenting a short introduction of AFM technique and experimental setup, PFM operating principle will be explained along with the experimental procedures employed for domain imaging and quantitative PFM characterization. Besides, the measurement technique used for the second-order non-linear optical susceptibilities is described.

3.1. Characterization Techniques

3.1.1. Optical Microscopy

Optical microscopy is a simple technique, which magnifies the object by using visible light and a system of lenses. We expected to produce different phases of glycine structures during crystallization. Optical microscopy is used for polymorph determination via observation of crystal morphology and for *in situ* monitoring the growth process during crystallization. Different polymorphic forms of crystals have distinct shapes which can be used with image analysis techniques for determining the polymorphic form. However, the shape is not always conclusive in characterizing the polymorphic form. A polarized microscope could be used to assess the level of misorientation in the crystals.

An optical microscope (Nikon Eclipse LV 150) with parallel and crossed polarizer and analyzer wave plate modes was used to visualize all the grown samples in this experiment.

3.1.2. X-Ray Diffraction

X-ray diffraction (XRD) is a powerful technique which can be used as the primary step to identify the crystalline phases and to determine the structure of the obtained glycine crystals. In X-ray diffraction a collimated beam of X rays is incident on a specimen and is diffracted by the crystalline phases in the specimen according to Bragg's law ($n\lambda = 2d \sin\theta$, where d is the spacing between crystallographic planes). A randomly orientated powder sample of a polymorph has a unique powder X-ray diffraction (PXRD) pattern, which is now the most common tool for polymorph identification.

Each crystal form of a given molecule has a unique powder X-ray diffraction pattern, made of diffraction peaks in certain positions and with differing intensities. When more than one polymorph is present, PXRD can give information on the relative amounts of different polymorphs in the mixture through the area under the peaks. PXRD can also give information on the preferred orientation of crystals.

Single crystal X-ray diffraction can be used to confirm the grown crystal as a single crystal and give detailed information of crystal structures, such as cell parameters values, crystal symmetry, and space group.

In this experiment, XRD patterns of glycine samples were collected with a powder diffractometer (Siemens D500) using Cu Kα radiation (λ = 1.54059 Å). The diffraction patterns were recorded in a reflection geometry at room temperature in the range 5°−70° with steps of 0.02°. The single crystal X-ray diffraction data were collected on a Bruker SMART Apex (II) CCD-based diffractometer at 150 K using graphite-monochromatized Mo Kα radiation (λ = 0.710 73 Å). The results are discussed in the Chapter 4.

3.1.3. Raman Spectroscopy

Raman spectroscopy is another structural characterization tool that detects the vibrational motion of chemical bonds. The Raman spectrum arises from the inelastic scattering of optical radiation (photons) by the electron clouds that make up the chemical bonds in the crystals. The scattered photon is related to the incident photon by frequency, ω, which is also called the Raman shift [146]. Thus the spectrum is sensitive to the lengths, strengths, and arrangement of bonds in the crystal structure. Different crystal structures tend to have distinct peak positions and intensities as a result of vibrational changes of molecules in the crystal lattice.

In the linear approximation, polarization, P, induced in the molecule under the influence of electric field of the incoming light, $E = E_0 \cos(\omega_0 t)$, can be written as :

$$P = \alpha E, \qquad (3.1)$$

where α is the polarizability tensor of the molecules, which characterizes the mobility of the electron cloud that makes up the chemical bonds, *i.e.* how easily it can be displaced or deformed under the influence of an external electric field.

Atomic vibrations near the equilibrium position periodically change the state of the electron shells and, therefore, the polarizability tensor. Thus, the components of the polarizability tensor α_{ij} equilibrium position can be expanded in a series in the normal coordinates Q:

$$\alpha_{ij} = (\alpha_{ij})_0 + \sum_k (\frac{\partial \alpha_{ij}}{\partial Q_k})_0 \, Q_k + \cdots \quad (3.2)$$

Therefore the polarization can be written as:

$$P = \alpha_0 E_0 \cos(\omega_0 t) + \frac{1}{2}\left(\frac{\partial \alpha}{\partial Q_k}\right)_0 Q_{k_0} E_0 \cos(\omega_0 - \omega_i)t + \frac{1}{2}\left(\frac{\partial \alpha}{\partial Q_k}\right)_0 Q_{k_0} E_0 \cos(\omega_0 + \omega_i)t \quad (3.3)$$

And the light is scattered at three frequencies: ω_0, $\omega_0 - \omega_i$ and $\omega_0 + \omega_i$. The first term in this expression represents the elastic (Rayleigh) scattering of light without changing the frequency. The second and third terms represent inelastic Raman scattering, with $\omega_0 - \omega_i$ and $\omega_0 + \omega_i$ corresponding to Stokes and anti-Stokes Raman scattering, respectively.

Raman spectroscopy is a fast analysis method without any post-processing and widely used, when the crystals are small and microfocus capabilities are important. Raman imaging is also possible, which adds important information about the crystal orientation and domain width.

In this work, Micro-Raman measurements were performed in a backscattering geometry using a WiTec alpha 300 AR confocal Raman microscope which combines the analytical capabilities of Raman spectroscopy (RS) and the high spatial resolution of a confocal microscope. An objective (10×, NA = 0.55) focused the exciting light (solid state laser, λ = 488 nm) onto the sample (spot diameter about 260 nm). A diffraction grating of 600 dashes/mm with a spectral resolution of 3.19 cm^{-1} at λ = 488 nm was used for light decomposition. All measurements were done at room temperature.

In this work, Raman scattering has been used for the detection of the polymorphic forms and to study polymorphic transformation [147].

3.2. Piezoresponse Force Microscopy (PFM) Technique

3.2.1. Introduction to Atomic Force Microscopy (AFM)

Scanning probe microscopy (SPM) is a unique tool for studying topography and physical parameters of materials. It offers several different possibilities to obtain information on the domain configurations of ferroelectric thin films, single crystals and ceramics. AFM is currently the most broadly employed tool in the SPM family, since it can measure a wide range of surface properties on any kind of materials, ranging from topography to surface potential, from electrical to magnetic properties. Moreover, AFM measurements can be performed under normal (ambient) temperature and pressure, thus not requiring special environmental conditions. In the standard experimental AFM systems, there are three main components for imaging the surface of the sample: a cantilever with probing tip sharpened down to several tens of nanometers, a piezo-electric scanner which controls the position of the sensing probe relative to the surface, and the optical system to measure the deflection or torsional twist of the cantilever. The two main imaging modes for all kinds of AFM systems are non-contact mode and contact mode. When the tip is brought to the sample in contact with or tapping the surface, it will be affected by a combination of the surface forces. Those forces cause cantilever bending and torsion and these deformations of the cantilever are detected by measuring the displacement of the laser spot, which is reflected from the back of the cantilever, on the position sensitive photo detector. Its resolution in the Z direction is of the order of subnanometer, while the lateral one is limited by the tip radius of curvature, *i.e.*, in the order of a few tens of nanometers.

A difference in mechanical, structural, electrochemical, dielectric and piezoelectric properties of opposite ferroelectric domains may provide distinct contrast in the AFM contact mode. In the non-contact regime, domains can be visualized by detecting surface polarization charge and surface potential. Currently, the most widely used AFM method for studying domain polarization and nanoscale switching behavior in ferroelectric materials is the so-called Piezoresponse Force Microscopy (PFM). PFM works in a contact regime based on the detection of local bias-induced surface deformation [148]. In this research, focused on the piezoelectric and ferroelectric properties of glycine crystals, we used PFM technique as the main experimental method.

3.2.2. Principle of Piezoresponse Force Microscopy (PFM)

PFM utilizes a basic experimental setup of Atomic Force Microscopy in which a conductive tip is brought into contact with the sample surface under a constant force (Fig. 3.1). The sample is positioned on the macroscopic bottom electrode and the PFM tip acts as a movable top nanoelectrode. The tip scans the sample and the bias voltage $V_{tip} = V_{dc} + V_{ac} . \cos(\omega t)$ is applied via the tip to the sample. The applied voltage creates an alternating electric field that causes the local deformation of the sample (expansion or contraction) due to reverse piezoelectric effect. Surface displacement is translated into the deflection of a cantilever $A = A_0 + A_{1\omega} \cos(\omega t + \phi)$ and this response is mechanically passed on to the cantilever and can be optically detected by the movement of the reflected laser on the four-quadrant photodiode as shown in Fig. 3.1 [149].

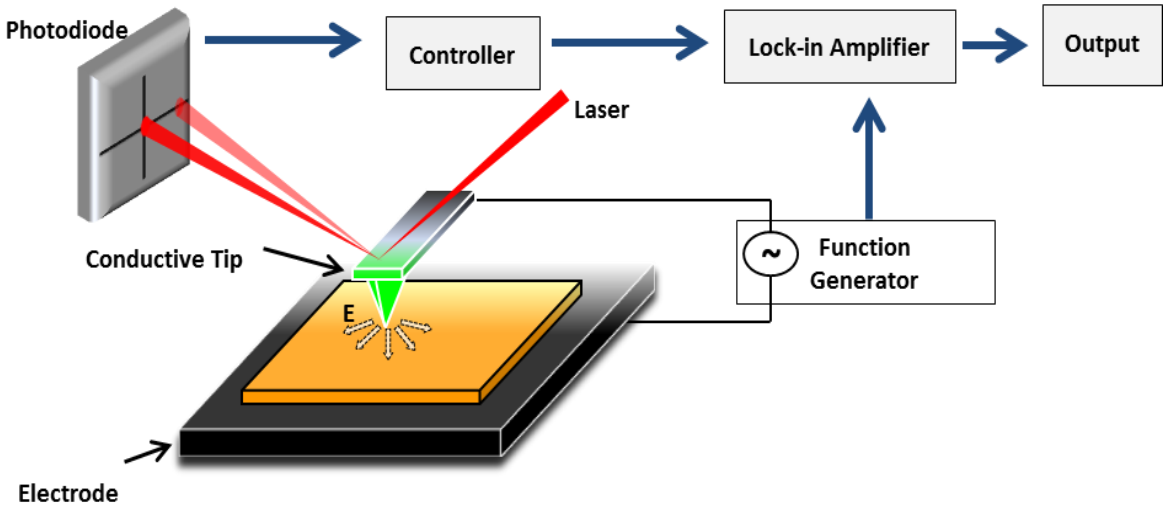

Figure 3.1. Experimental setup of Piezoresponse Force Microscope.

The signal collected by the photodetector is analyzed by the lock-in amplifier and the phase and amplitude of the response can be obtained in addition to the regular topography. The phase of the electromechanical response, ϕ, gives information on the polarization direction of the sample below the tip. The amplitude, $A = A_{1\omega}/V_{ac}$, defines the strength of the piezoelectric activity of the surface. The sign of the piezoelectric effect depends on the relative orientation of polarization of the sample and applied electric field [150,151].

Vertical vs. Lateral PFM

Deformation caused by the applied AC voltage can occur in any direction, and therefore, it leads to deflection, bending (buckling) and torsion of the cantilever. PFM can be operated in two modes, namely, vertical (VPFM) and lateral (LPFM) as schematically presented in Fig. 3.3. VPFM enables distinguishing the domains with a different out-of-plane component of the polarization. For domains whose polarization vector is oriented perpendicular to the surface, applying an electric field parallel to it results in the expansion of the sample. In this case, surface oscillations are in phase with the tip voltage, and $\phi = 0$. For domains with antiparallel orientation of the field and polarization the sign is reversed and the phase difference will be in 180°(*i.e.* $\phi = 180°$). (Fig. 3.3a,b).

In addition to the vertical displacement of the cantilever, there exists another type of PFM measurement. When the polarization is parallel to the sample surface, the voltage applied to the tip results in an in-plane surface displacement which is then translated into cantilever torsion (Fig. 3.3c,d). The torsion of the cantilever is measured by the lock-in technique in the same way as the modulated deflection signal in the photo-detector is measured in VPFM. These types of measurements are called lateral PFM (LPFM) [152]. The piezoelectric coefficient (relationship between the strain and the applied electric field) measured in the direction of the applied field is usually called the longitudinal coefficient (d_{33}), and that measured in the direction perpendicular to the field is known as the shear coefficient (d_{15}). Combining vertical and lateral PFM signals can be used to create a 2D vector PFM map of molecular orientation in piezoelectric biomaterials [153].

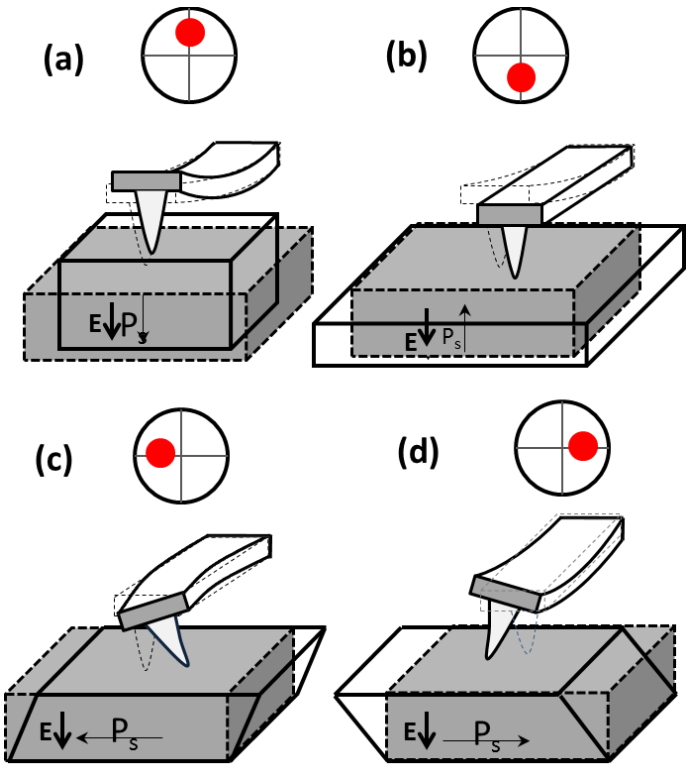

Figure 3.3. Schematic illustration of (a,b) vertical PFM, and (c,d) lateral PFM.

Switching PFM

In addition to domain structure imaging and quantitative local electromechanical measurement, PFM can be used for the investigation of nanoscale domain switching under an external electric field. In switching measurements a probing tip is fixed at a certain location on a sample surface. If voltage pulses higher than the characteristic coercive voltage are applied to the tip, the spontaneous polarization under the tip can be switched. This allows the creation of any desired pattern of ferroelectric domains. With PFM imaging after each pulse, nascent domains can be visualized and it provides direct information about the local coercive field strength for nucleation of new domains and velocity of domain wall motion. The second approach of polarization switching behavior is to measure the hysteresis loops in the pulse mode. In this case, a sequence of *dc* voltage pulses with the same duration and with the amplitude cycled from $-V_{min}$ to V_{max} is applied and the piezoresponse is measured between the pulses at each step (Fig. 3.4). Because no bias voltage is applied during the measurements, the contribution related to electrostatic interaction is minimized and actual remanent piezoresponse is detected.

The shape and/or shift of the hysteresis loop contain important information about the switching mechanism, spontaneous polarization, saturated polarization, coercive field and imprint I_m in case of asymmetry hysteresis ($I_m = (V^+ + V^-)/2$).

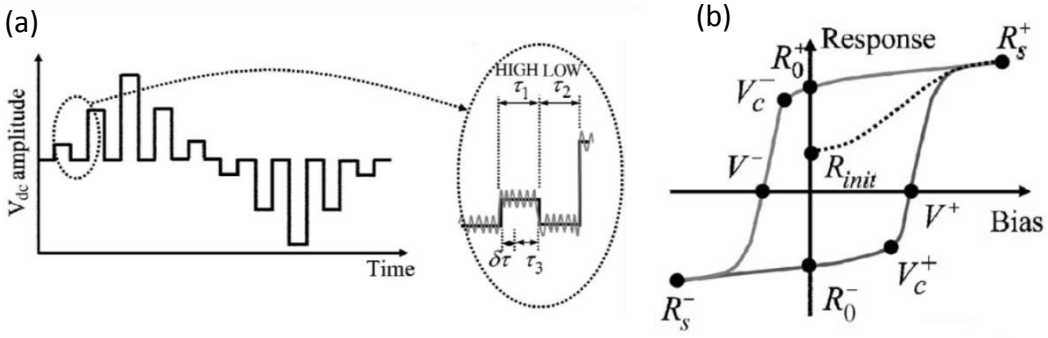

Figure 3.4. a) Probing *dc* bias wave form in switching PFM. τ_1 is the writing period, τ_3 is the reading period and τ_2 is the waiting interval. b) Illustration of piezoelectric hysteresis loop, forward and reverse coercive voltages, V^+ and V^-, nucleation biases, V_c^+ and V_c^-, and forward and reverse remanent and saturation piezoresponses, R_0^+, R_0^-, R_s^+ and R_s^-, are shown [154].

The high spatial resolution (down to several nanometers), investigation of local piezoelectric properties, analysis of ferroelectric domain wall structures and its correlation with microstructural features and local spectroscopy capabilities make PFM a well-suited tool for nanoscale ferroelectric studies [155,156].

3.2.3. Experimental Setup for PFM Measurements

For this study the piezoresponse measurements were performed mainly with a commercial AFM (Ntegra Prima, NT-MDT, Russia) equipped with an external function generator (FG120, Yokogawa, Japan) and a lock-in amplifier (SR830, Stanford Research System, USA). A conductive Si cantilevers (from Nanosensors) with resonance frequency and spring constants of 75 kHz and 3 N/m, respectively were used throughout the experiment.

Domain Visualization and Switching Measurement of Glycine Crystals by PFM

PFM was used to investigate the local piezoelectricity and to image the apparent ferroelectric domain structure in piezoelectric phases of glycine (both β and γ). During imaging, a harmonic *ac* voltage (typically 10 V), was applied locally to the sample via the PFM tip, leading to sample deformation due to converse piezoelectric effect. The specific measurement frequency (~ 15 kHz) was chosen to be well below the resonance frequency of the contact, identified in a frequency sweep in order to minimize any interference from topography or elasticity variations in the sample surface to the PFM signal.

Only β-glycine microcrystals which were isolated and in full contact with the Pt substrate were chosen for analysis. In order to find the polarization direction orientation of the structural units inside the crystals, we use orientational PFM-imaging. In this method comparing PFM contrast in the vertical and lateral images and considering the geometry between tip and crystal axes reveals important information about the polarization direction of crystals. For the lateral response mode PFM measurement, the orientation of glycine microcrystals with respect to the cantilever axis can affect the magnitude of the piezoelectric signal. Thus the substrate was rotated prior to the experiment to align the long axis (polarization direction) of the studied crystal perpendicularly to the cantilever axis in order to detect maximum shear piezoelectric deformation. This geometry also minimizes any contribution of cantilever buckling with the measured lateral signal [157].

Switching spectroscopy PFM was performed to confirm polarization switchability of domains [158]. In these measurements, the tip is fixed in a predefined position on the sample surface and voltage bias pulses of variable strength and duration are applied. Domain configurations are imaged immediately after each pulse. In some cases, we could observe an instability of the switched domains (polarization backswitching). In these cases, several scans were done until the stable domain configuration was reached. In order to obtain piezoresponse hysteresis loop, a sequence of *dc* voltage pulses was applied to the PFM tip in a cyclic manner and piezoresponse (typically $A\cos\theta$) was measured between the pulses [154].

PFM Calibration

In order to convert the voltage output signal to length units for quantitative PFM measurement, the deflection and torsional sensitivity coefficient (nm/V) of the cantilever was required. The out-of-plane deflection sensitivity was measured based on the standard analysis of the force curve acquired from pressing the AFM probe on a glass substrate. The in-plane sensitivity was calculated based on the geometry of the cantilever and the measured out-of-plane deflection sensitivity as described by Peter *et al*. [159,160]. It was shown that $R = 2L/3h$, where R is the in-plane/out-of-plane sensitivity ratio, L is the length of the cantilever, and h is the tip height plus cantilever thickness. For cantilevers used in this study, L = 225 μm and h = 12 μm, with the out-of-plane deflection sensitivity of 97.4 nm/V, and therefore the in-plane sensitivity was calculated as 1217.5 nm/V.

In order to obtain the absolute value of piezocoefficient, the slope of piezoresponse curve of a glycine microcrystal was measured at a point while varying the amplitude of the electric bias from 0 to 15V.

3.3. Nonlinear Optical Measurements

As mentioned in the Chapter 1, second harmonic generation (SHG) is due to the emitted light at frequency which is two times that of incident light. The relation between the SHG intensity and the electric field of incident light E^{ω} in non-centrosymmetric crystals is proportional to nonlinear polarization squared $I^{2\omega} \propto \left(P_i^{2\omega}\right)^2$ and can be written in a tensor form as:

$$P_i^{2\omega} = \chi_{ijk}^{(2)} E_j^{\omega} E_k^{\omega}, \qquad (3.4)$$

where i, j, k represent the coordinates x, y, z and $\chi_{ijk}^{(2)}$ (the nonlinear susceptibility tensor) is defined by the crystallographic structure of the crystal. Analogously to the refractive index (which characterizes the optical properties but also reflects crystallographic structure as well), the nonlinear susceptibility tensor depends on the optical transitions and reflects even more strongly the crystallographic structure. In order to get this information, a set of measurements

should be performed, namely, SHG intensity vs. azimuthal rotation of the sample and polarization rotation of the incident light.

In nonlinear optical measurements (SHG method), the light from a solid-state laser based on a titanium-doped sapphire crystal was used. The output of a Ti:sapphire laser (800 nm) had a pulse width of 100 fs, a repetition rate of 80 MHz, and an average power of 30 mW focused onto a spot of about 50 μm in diameter. A reflecting geometry was used with the incidence and reflection SHG light fixed at 45° relative to the sample plane. The reflected SHG signal was discriminated by color filters and measured by a photon counting system (see Fig. 3.5 for details).

For the polarization studies, a polarizer placed in front of the sample and an analyzer placed beyond the sample were used (Fig. 3.5). Thus, the variation in the mutual orientation of the electric field vector for the incident and reflecting beams allowed determination of all components of the nonlinear susceptibility tensors χ which are responsible for the polarization and symmetry dependences. In the following results, the electric field vector parallel (perpendicular) to the incidence plane will be termed as P (S) output, respectively.

As a reference sample for the azimuthal and polarization rotation measurements we have used a z-cut (001) quartz plate with a well-known nonlinear susceptibility tensor.

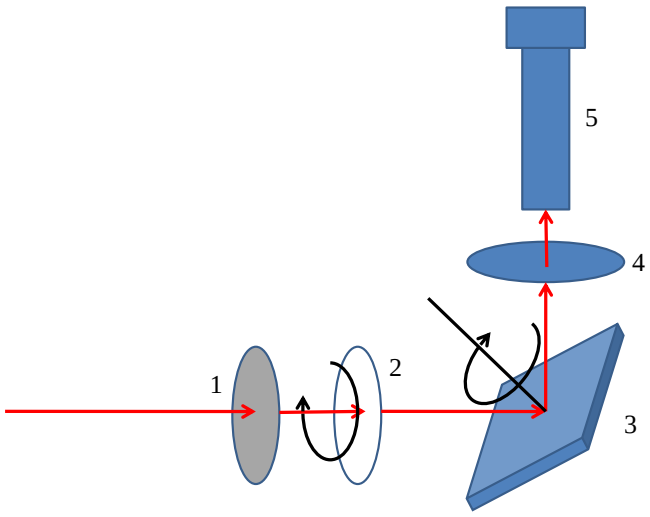

Figure 3.5. Schematic of the measurement setup for the acquisition of azimuthal and polarization dependences of SHG signal: 1 – polarizer, 2 – λ/2 wave plate, 3 – sample, 4 – analyzer; 5 – photomultiplier tube.

Chapter 4

Crystal Growth and Characterization

In this Chapter, the preparation of single crystals of all three phases of glycine: α-, β-, and γ-forms from solution and the conditions that affect the growth of crystals and polymorph selectivity are discussed. All the obtained crystals were first characterized by the combination of optical microscopy and X-ray diffraction.

In the following of this Chapter, some template-assisted methods are shown to be well suited for the synthesis of stable β-glycine microcrystals. The crystallization process of glycine driven by the evaporation of aqueous solution on crystalline (111)Pt/Ti/SiO_2/Si substrates is discussed in detail. The effects of the solution concentration and Pt-assisted nucleation on the crystal growth and phase evolution are evaluated using X-ray diffraction analysis and Raman spectroscopy.

Finally, we describe the growth of highly aligned micro- and nanoislands of β-glycine on Pt substrates by spin-coating technique.

4.1. Crystallization from Solution

α-glycine

Glycine powder (99% pure) was purchased from Sigma Aldrich. Powder X-ray diffraction (PXRD) analysis confirmed that as-received glycine was in the α-form. α-glycine crystals were simply prepared by evaporation from pure, 3M aqueous solution of glycine at neutral pH without the presence of any additive as described in section 2.3 of Chapter 2. The α-phase usually crystallizes in bi-pyramids morphology as shown in Fig. 4.1. The type of crystals polymorph was confirmed using PXRD and the positions of the peaks in the X-ray spectrum were found to be in a good agreement with the data available in JCPDS database (00-032-1702) for α-glycine (Fig. 4.2).

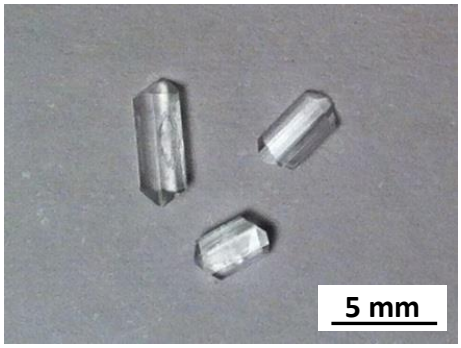

Figure 4.1. Optical microscopy image of single crystals of α-glycine.

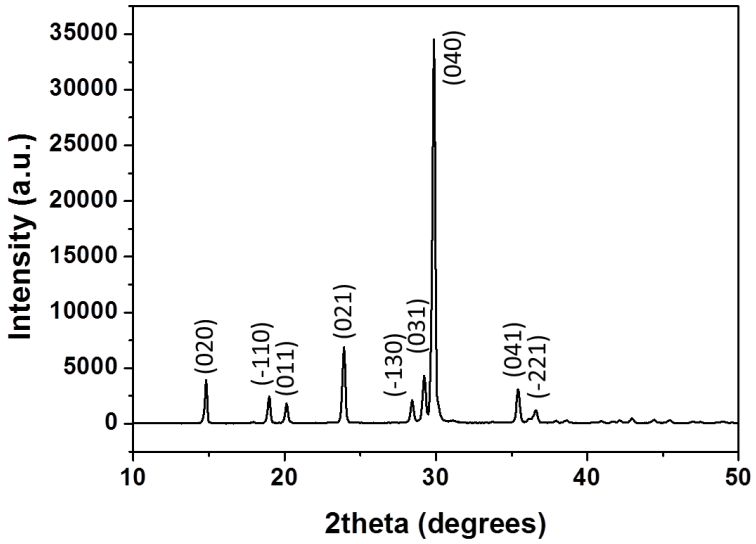

Figure 4.2. The indexed powder XRD pattern of α-glycine crystal.

In the α-polymorph, glycine dimers are linked to each other by hydrogen bonds in double antiparallel layers and the layers are connected together by van der Waals interaction. The individual molecular dipole of each glycine molecule is compensated by that in opposite direction and formed crystals have centrosymmetric space group ($P2_1/n$, Z = 4) and, consequently, cannot have piezoelectric properties [161].

γ-glycine

Although the γ polymorph is thermodynamically the most stable form of glycine known at ambient conditions, crystallization of γ-glycine in neutral aqueous solutions is typically hindered by the formation of the kinetically favored α form. In this work, single crystals of γ-glycine were grown from aqueous solution by slow evaporation method in the presence of lithium nitrate that suppressed the formation of α-glycine. As the formation of pure γ-glycine crystals starts below a certain rate of evaporation, the crystallizing solution stays close to equilibrium throughout the evaporating process allowing the system to sample the lowest free energy state during the formation of nuclei. Aqueous solution of glycine (Sigma-Aldrich, 99%) and lithium nitrate (Sigma–Aldrich, 99.5%) in 2:1 mole ratio was prepared in deionized water (resistivity 18.2 MΩ.cm) at room temperature. The prepared solution was stirred for four hours in order to dissolve fully and then filtered with a Whatman filter paper. The solution was taken in a beaker, closed with a perforated cover and allowed to

evaporate slowly at ambient temperature. A few days after solvent evaporation, the solution becomes supersaturated and tiny crystals were seen. They were allowed to grow for bigger dimension and 5 weeks later, crystals with hexagonal prismatic morphology were obtained (Fig. 4.3). Lithium cations do not enter the crystal structure, but remain in the solution as free ions; they just influence nucleation and growth kinetics. Glycine crystals grew along the c direction, possessing (010) and (100) lateral faces (Fig. 4.3).

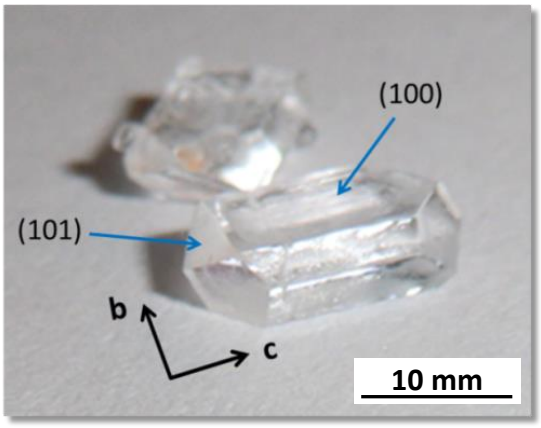

Figure 4.3. Optical microscopy image of single crystals of γ-glycine.

The powder XRD confirmed the formation of a pure single γ-phase structure. The positions of the peaks in the x-ray spectrum were found to be in a good agreement with the data available in JCPDS database (00-006-0230) for γ-glycine. The various planes of reflections were indexed in PXRD as shown in Figure 4.4. The calculated cell parameters of the γ-glycine crystal from single crystal XRD data are a = b = 7.038 Å, c = 5.48 Å, α = 90^o, β = 90^o, γ = 120^o and V = 233.9 Å^3, which agree well with the literature data [162].

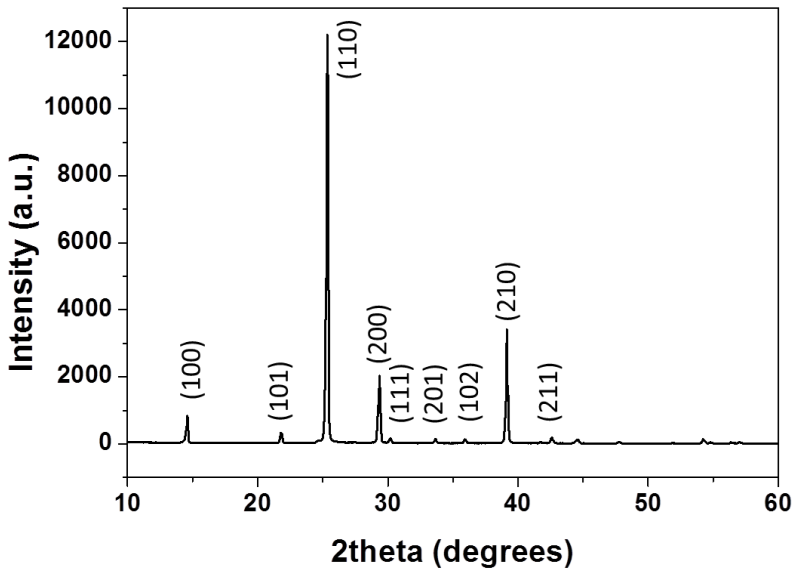

Figure 4.4. An example of the indexed powder XRD pattern of γ-glycine crystal.

β-glycine

As mentioned in Chapter 2, the unstable β-glycine was typically crystallized at high supersaturation, such as that which occurs during anti-solvent crystallization. In this work, a slightly undersaturated aqueous solution of glycine was prepared (5ml), and then ethanol was added quickly to this solution (10ml). A lot of thin needles of β-glycine appeared within minutes as presented in Fig. 4.5 a,b. If crystals stayed in the solution for a longer time, β-glycine was found to recrystallize to an α-form within 20 min of contact with solution. Transformation from the β to α glycine was monitored using optical microscopy, as seen in Fig. 4.5 c-f. Needle-like β-glycine crystals first begin to break into many small crystals and then dissolve. With the dissolution of needle-like crystals, the supersaturation of the solution increases and stable bipyramidal crystals corresponding to α-form start to appear. This transformation can occur because of the interplay of thermodynamics and nucleation kinetics of the two polymorphic forms. In the similar experiment we have found that the speed of the transformation is even faster if the initial portion of water to ethanol increases.

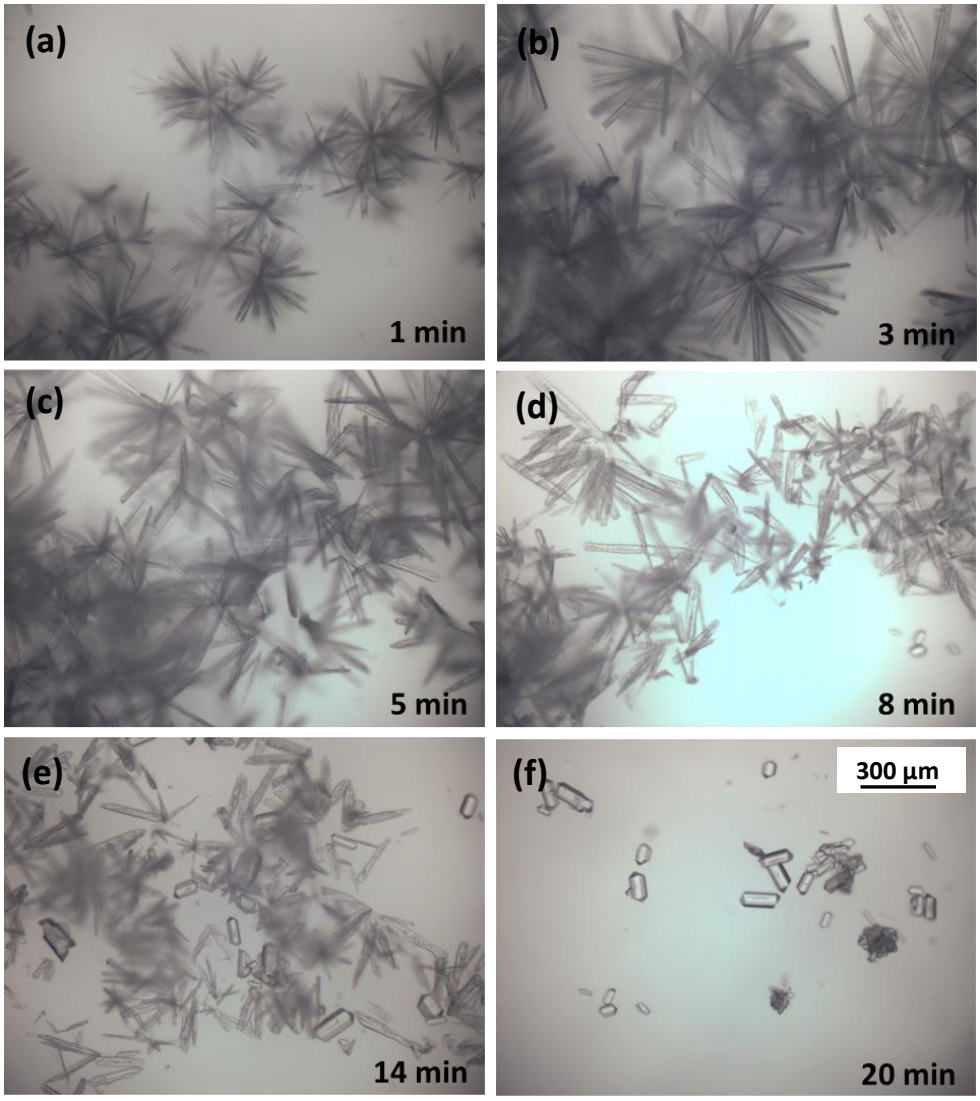

Figure 4.5. Microscopic images taken during solution-mediated transformation from the β- to the α-form of glycine in the aqueous ethanol solution.

However, if the crystals were isolated rapidly after growth by filtration, washed with ethanol, and dried in an oven at 60 °C, we could have almost pure β-glycine. The crystal structure of β-glycine is shown in Fig. 4.6. The X-ray diffraction pattern of β-glycine has characteristic peaks at 18^o, 24^o, and 28^o as shown in Fig. 4.7 (black spectrum). The positions of the peaks in the powder X-ray data were found to be in a good agreement with the data available in JCPDS database (00-002-0171) for β-glycine. However, the problem was the instability of the crystal under ambient conditions. Crystals were kept at room temperature and humidity for three weeks and then x-ray diffraction was performed from the same batch

of the sample (red line in Fig. 4.7). A spontaneous transformation of β to α-phase was observed by the comparison of two diffraction patterns (Fig. 4.7).

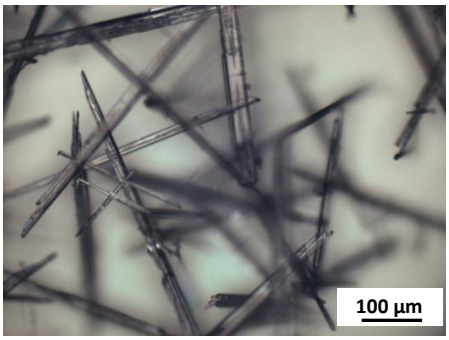

Figure 4.6. Optical microscopy image of single crystals of β-glycine grown from water/ethanol solution.

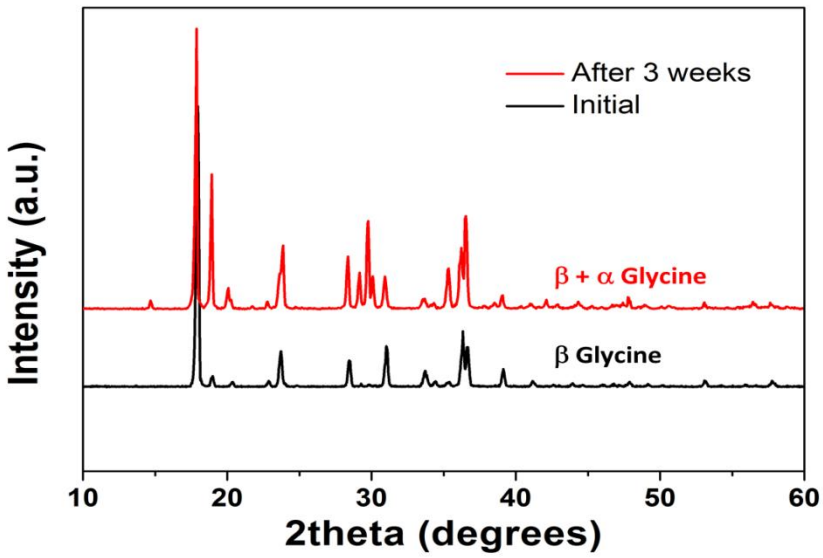

Figure 4.7. Comparison of XRD pattern of the initial β-glycine crystals and its transformation after 3 weeks of shelf time.

In order to synthesize stable single crystals of the glycine β-polymorph, we chose the crystal growth on Pt substrates as detailed in the following section.

4.2. Crystal Growth on the Substrate

Besides inherent capability of amino acids to molecular recognition and self-assembly through their functional group (-COO^- and -$NH3^+$), the adsorption of amino acids (specifically, glycine) on the metal and oxide surfaces has made them attractive for the synthesis of functional nanostructures. The nature of these interfacial bindings on a solid surface has been reported for glycine in many papers. For example, glycine was found to adsorb in the zwitterionic form on Pt(111) [163] and Au [164] substrates and in ionic form on Cu surface (110) [165]. Therefore, we conclude that the crystal growth of glycine on the solid surface can be controlled by the intermolecular and molecule-substrate interactions.

In this section, a simple method of the stabilization of β-phase is been demonstrated based on the evaporation of glycine solution on commercial (111)Pt/Ti/SiO_2/Si substrates.

4.2.1. Sample Preparation

The droplet evaporation technique was used for the molecular self-assembly and crystal growth on (111)Pt/Ti/SiO_2/Si substrates. In this process, the supersaturation and crystallization conditions are controlled by the evaporation rate. Different concentrations of glycine solutions (1.77, 0.66, 0.133, and 0.0133 M) were prepared by dissolving various amounts of glycine powder in an ultrapure water. All solutions were rigorously stirred and filtered before crystallization. Commercial (111)Pt/Ti/SiO_2/Si substrates (Inostek, 30–200 nm Pt deposited on the 10nm Ti adhesion layer and the substrate were thermally oxidized Si (100) wafer) were cleaned with alcohol and pure water in an ultrasonic bath. Glycine solutions were dropped (50 μL) onto clean surfaces using a micropipette. The surface was left for crystallization under ambient conditions (21 °C, humidity 30%) until the droplet dried out completely (Fig. 4.8).

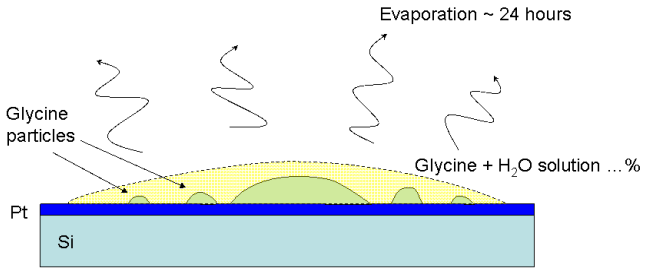

Figure 4.8. Schematic of the crystal growth on the surface.

4.2.2. Structural Characterization of Glycine Microcrystals

Glycine crystals were obtained by the evaporation of microdrops of the water-based solutions on (111)Pt/Ti/SiO_2/Si substrates. PXRD analysis confirmed the existence of all three α-, β-, and γ-polymorphs, but the distribution and the size of grown crystals were found to be strongly dependent on the initial solution concentration. Table 1.4 summarizes the presence of different glycine polymorphs crystallized on the substrate as a function of the solution concentration. Apparently, all three phases were present in the crystals grown from the concentrated solutions, while only β- and α-phases were observed for lower concentrations. The β-phase was found to be a dominant one as discussed in detail below.

Table 1.4 Polymorph distribution of glycine crystals grown on a Pt surface at 21 °C

Concentration of glycine	Polymorph distribution
133 mg/mL = 1.77 M	α, β, γ
50 mg/mL = 0.66 M	α, β, γ
10 mg/mL = 0.133 M	α, β
1 mg/mL = 0.0133 M	α, β

In order to quantify the phase content, X-ray diffraction patterns were obtained from the crystals attached to the substrate. The spectra were compared with the data available in JCPDS database (00-032-1702 for α-glycine, 00-002-0171 for β-glycine, and 00-006-0230 for γ-glycine). The presence of each phase was revealed by the presence of the corresponding peaks in PXRD data. The positions of peaks substantiate the existence of all glycine phases at higher concentration (1.77 and 0.66 M), while at lower concentrations (0.133 and 0.0133 M) only α- and β-phase were seen (Fig. 4.9). Raman spectroscopy was then used for the detailed identification of crystalline forms.

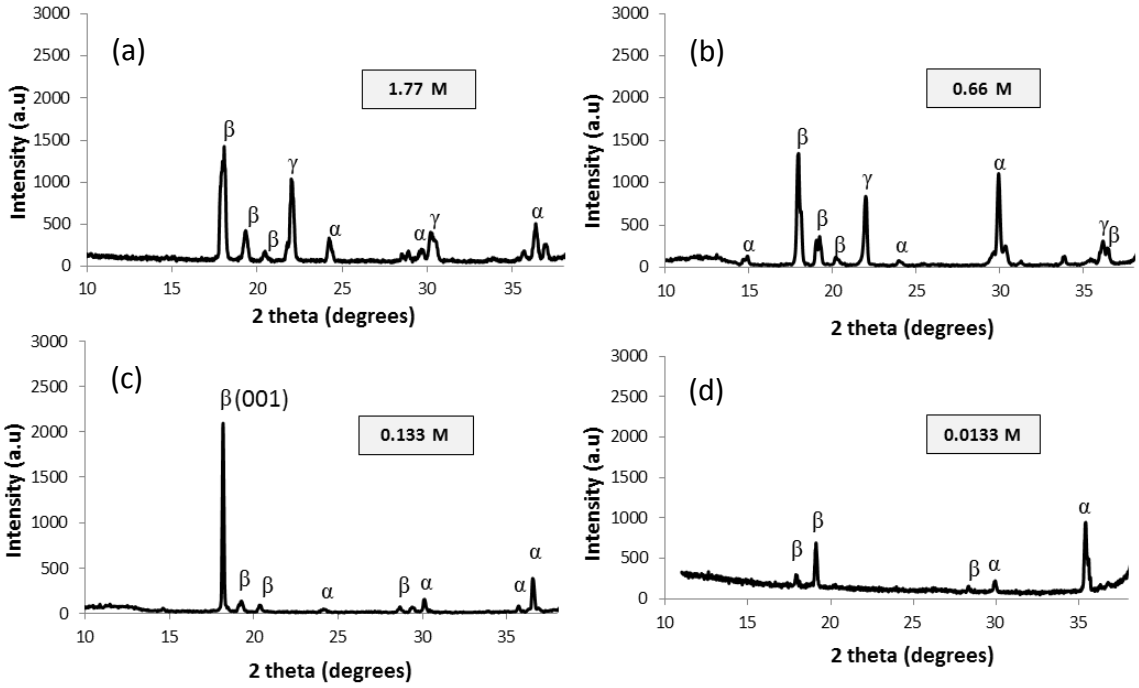

Figure 4.9. X-ray diffraction patterns of different glycine samples grown on the $Pt/Ti/SiO_2/Si$ substrates from the solutions of (a) 1.77, (b) 0.66, (c) 0.133 and (d) 0.0133 M concentrations.

Since we were interested only in β-phase, we focused on the study of batches grown from the diluted solutions. As an example, Fig. 4.10 demonstrates optical micrographs of all three types of crystal morphologies found on a Pt substrate for the 0.133 and 0.0133 M concentrations: the bipyramidal, the transparent needle-shaped, and the dendrite-type crystals, respectively.

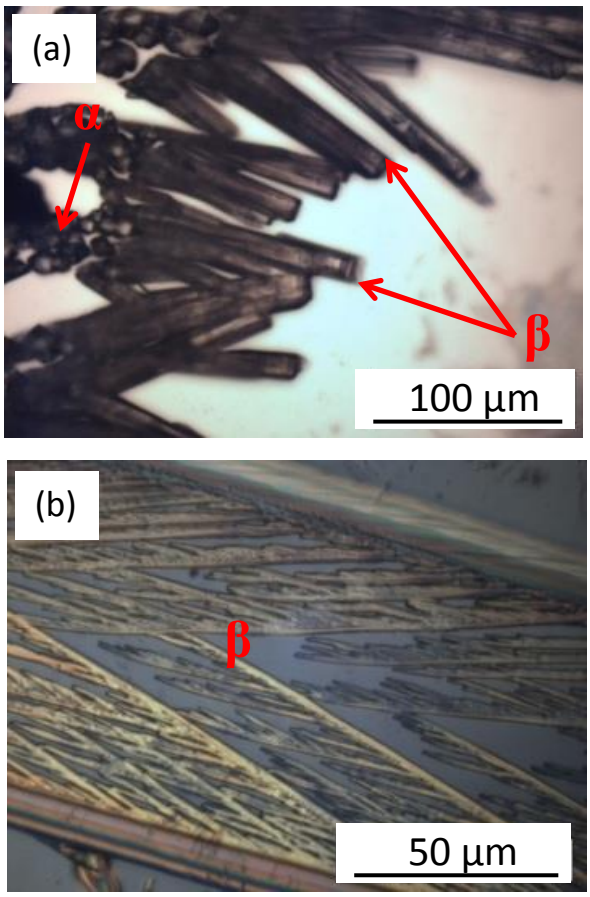

Figure 4.10. Optical images of (a) bipyramidal α-glycine and needle-shaped β-glycine and (b) dendrite β-glycine.

Following deposition, we used the micro-Raman spectroscopy to identify the polymorphic form of each crystal type in the 0.0133, 0.133, and 0.66 M concentration samples. In this technique, a phase analysis is typically performed by the determination of each phase fingerprints (PF) in Raman spectra and by the comparison of the peak positions with literature data [166,167]. Raman spectra for three studied crystal morphologies are considerably different (Fig. 4.11). In particular, three separate spectral regions, 100−260, 1200−1600, and 2800−3200 cm^{-1}, were compared to distinguish all three polymorphic forms. The first region includes mainly glycine lattice vibrations. Since glycine phases differ in the individual molecule's packing, this region represents the most important PFs. The second spectral region contains bands corresponding to torsional vibrations of the CH_2 group (spectral line at about 1327 cm^{-1}) and symmetrical stretching of the CO_2 group (spectral line at about 1414 cm^{-1}). As such, these lines can be used as PFs for phase identification.

Probably, the most convenient PF can be found in the third spectral region, where the bands of symmetric and antisymmetric stretching vibrations of the CH_2 group are present. The line position in the vicinity of 2960 cm^{-1} strongly depends on the glycine phase and varies from 2953 cm^{-1} for β-phase up to 2972 cm^{-1} for α-phase. Thus, Raman spectroscopic analysis fully confirmed that the needle-shaped and dendrite crystals belong to β-phase, while bipyramidal crystals were all of an α-phase (Fig. 4.10). (Raman spectroscopy measurements have been carried out by Dr. Pavel Zelenovsky in Ural Federal University, Ekaterinburg, Russia.)

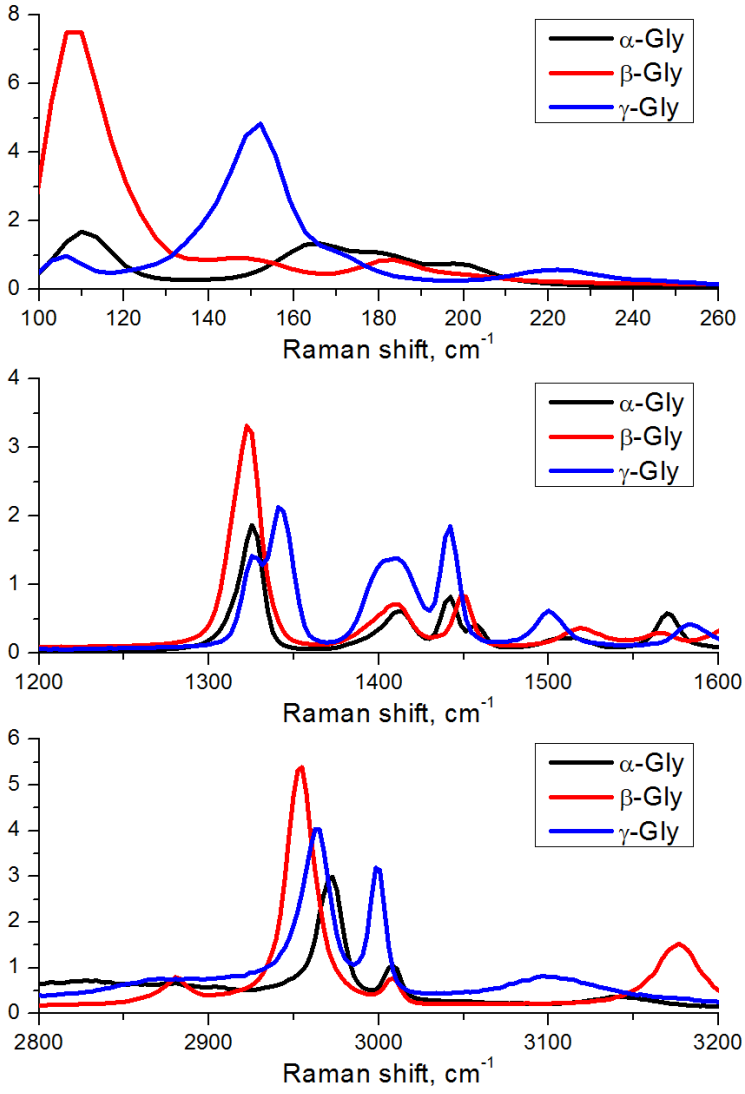

Figure 4.11. Three spectral regions of the Raman spectra used for the identification of the glycine crystal phases. Measurements were made on samples with 0.133 and 0.66 M concentrations.

At high solution concentrations, the γ- and β-phases were observed in addition to bipyramidal crystals of α-phase. However, at low solution concentrations, γ-phase is absent, as confirmed by Raman measurements. This observation establishes that the rate of supersaturating generation and drying conditions can control the polymorph selectivity through changing the crystal growth kinetics and thermodynamics as discussed below.

Crystallization of the needle-shaped β-glycine for all concentrations is in agreement with the basics of Ostwald law [168], which states that the crystallization from a solution should start from the nucleation of the least stable polymorph and then it should transform to a more stable phase. It is true also for the glycine-based solutions: we have shown that the less stable β-phase is formed first (Figs. 4.12 and 4.13). At high concentration (0.66 M) (Fig. 4.12), since the time between the appearance of first β-crystals (Fig. 4.12b) and complete drying (Fig. 4.12f) was sufficiently long (almost 20 min), the β-crystals nucleated at the periphery of the drop could eventually grow to a large size, but part of them was readily transformed to α- or γ-phases through the contact with the solution. In the central part of the drop, α-crystals of a bipyramidal shape had also enough time to nucleate and grow.

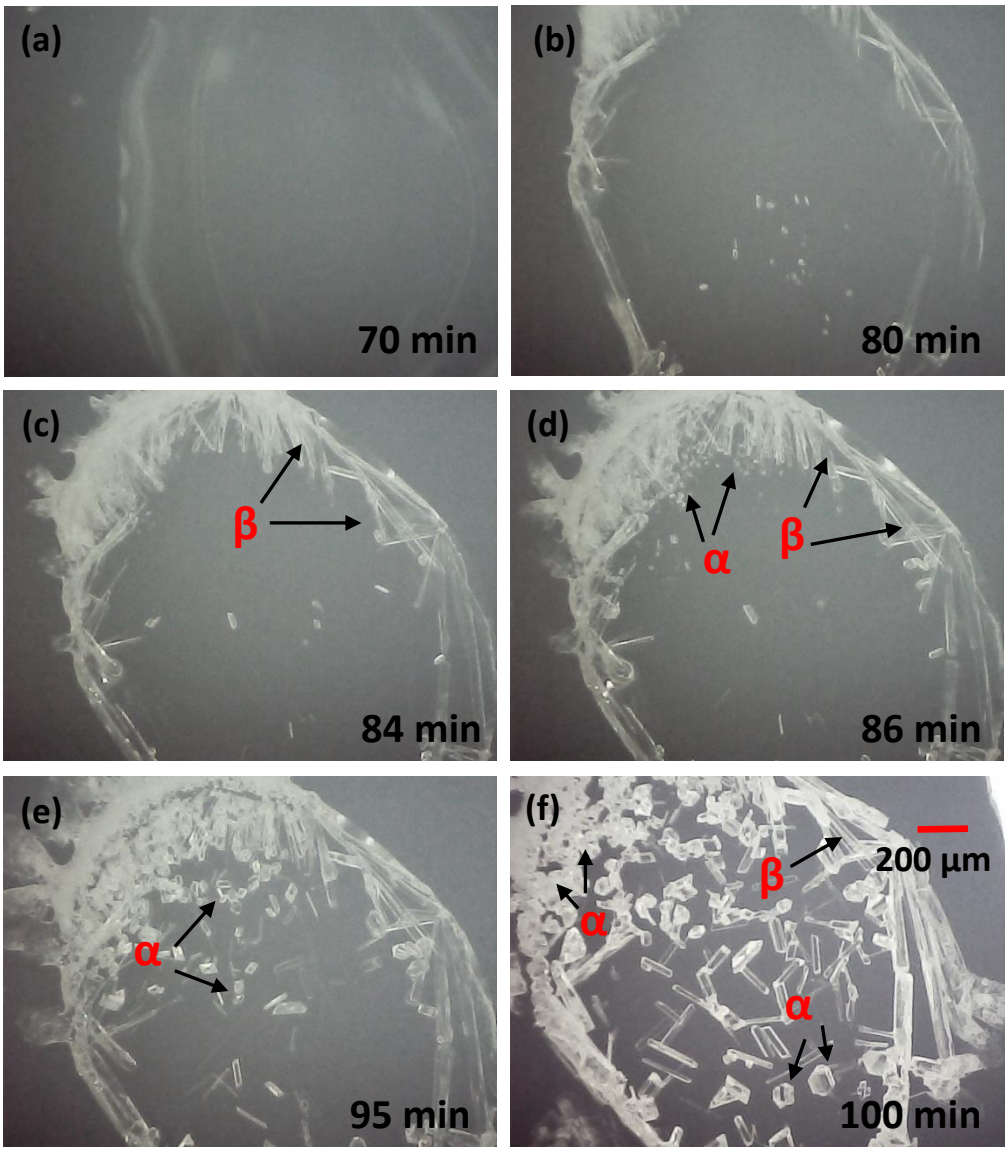

Figure 4.12. Optical images of the glycine crystals growth during evaporation of a 0.66 M solution drop on a Pt/Ti/SiO_2/Si substrate. All images are the same scale.

In contrast, at lower concentrations (0.133 M, Fig. 4.13) β-crystals were the predominant species on the surface, because the solution reached the saturation before completely drying, thus nucleation and growth occurred in a few seconds (Fig. 4.13c−e). In other words, β-crystals appear some minutes before drying and do not have time to transform to the undesirable α-phase. As such, nonequilibrium precipitation and fast drying yield the kinetically limited polymorph, β-phase, at the expense of the undesirable γ- and α-phases. All these studies suggest that kinetic restrictions on crystal nucleation and growth have a

dominant effect on polymorph selectivity, despite the thermodynamic driving force caused by the relative stability of different polymorphs.

In addition, the dendrite β-glycine structure grows very fast on the Pt substrate between microcrystals for low solution concentration (Fig. 4.13e). Thin liquid between the crystals raptures by dewetting, and dendrite crystals are created due to 2D nucleation on the surface. This phenomenon, usually referred as spinodal dewetting [169], and the specific formed dendrite patterns are highly dependent to the type of chosen substrate [170]. Little difference in the grown structures was observed upon repeating the growth experiments with slightly different relative humidity and temperatures. After complete drying, β-crystals were stabilized through their contact with the Pt substrate and we did not see any further transformation to other phases within 1 month of the shelf time under ambient conditions. The grown β-crystals possessed the identical Raman spectra and looked uniform and transparent under a polarized light (Fig. 4.14). The average sizes of β-glycine needle-shaped crystals grown from the diluted solution (about $30 \times 200\ \mu m^2$) were comparable to those reported in the literature [171]. At 0.133 M concentration, the (001) peak of β-glycine (2θ = 18°) was considerably increased (Fig. 4.9). This confirms that the (001) crystal planes are parallel to the substrate and that the growth direction of the needle crystals is along the (100) plane (*b* direction).

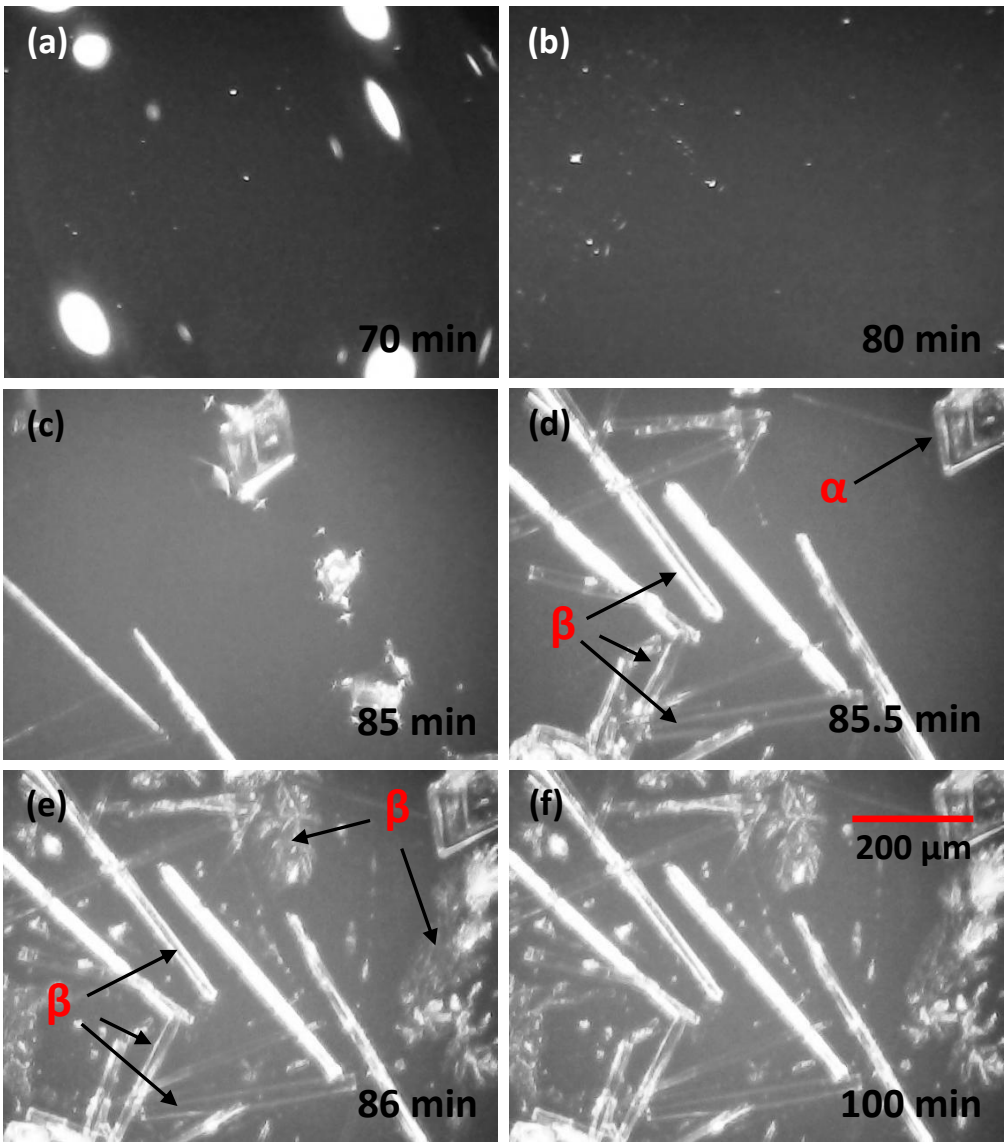

Figure 4.13. Optical images of the glycine crystals grown by the evaporation of 0.133 M solution drop on Pt/Ti/SiO_2/Si substrate. All images are the same scale.

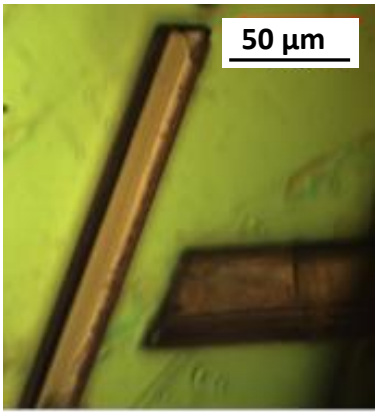

Figure 4.14. Optical image of two β-glycine crystals obtained after 1 month of shelf storage.

The observed stability and preferred growth of β-glycine can be attributed to the interaction between the glycine molecules and highly crystalline Pt/Ti/SiO_2/Si substrate. In general, the nucleation and growth of organic molecular crystals on the crystalline substrates are controlled by chemical interactions rather than by the epitaxial relationship [172]. The adsorption and surface interaction mechanism of glycine molecule on Pt surface have been studied a long time ago [163,173]. It was reported that the glycine zwitterions could adsorb on the Pt surface through the interactions of both deprotonated carboxyl ($-COO^-$) and protonated amino ($-NH_3^+$) groups. In this bonding, the lone-pair orbital of the oxygen atom overlap with orbitals of the three adjacent Pt atoms forming the hollow site, and the lone-pair orbitals of the nitrogen atom could well couple to the Pt d_{z^2} orbital in the on-top position [174]. We believe that, due to this interaction, Pt surface acts as a nucleation site for glycine crystals through bonding and stabilization of the initial β-phase nuclei. Therefore, it facilitates the growth and prevents further rearrangement of molecules and phase transformation into other phases. Since the observed solid–solid phase transformation starts from the crystal–substrate interface, chemical interaction of glycine with Pt may prevent this transformation in an adlayer and thus consequently slow down the transformation of the entire crystal. These observations reveal the potential of Pt-coated substrates to control the polymorphic selectivity, stability, and preferred orientation of β-glycine.

Dendrite β-glycine structures were even more stable as compared to needle-shaped ones under ambient conditions over a period of several months due to their nanoscale thickness and better interaction between the glycine functional groups with Pt substrate.

In addition to micro-Raman data, single crystal X-ray diffraction measurements have been done for the crystals of needle-like and bipyramidal shapes. The results revealed that the needle-shaped crystals (assigned to β-phase by Raman spectroscopy) belong to the monoclinic system (group $P2_1$) with the following unit cell parameters: a = 5.08 Å, b = 6.25 Å, c = 5.36 Å, β = 113.43°, and α = γ = 90°. These values are very close to those reported previously in the literature [175]. As expected, bipyramidal crystals (α-phase) exhibited reflections characteristic for the monoclinic structure (symmetry $P2_1/n$), and the following cell parameters were extracted: a = 5.08 Å, b = 11.90 Å, c = 5.46 Å, β = 111.29°, and α = γ = 90°. These values are also in a good agreement with the literature data [176]. Therefore, we can conclude that the preferential growth of high-quality glycine β-polymorph was achieved by the careful control of the growth conditions and choice of the suitable substrate (Pt).

4.3. Glycine Thin Films

The difficulties in the growth of large bulk single crystals of β-glycine have motivated us to try to prepare thin films of glycine for easier miniaturization and integration. Several methods exist for the formation of ordered layers of organic materials on surfaces. Among them spin coating offers a simple inexpensive method which was extensively applied for the deposition of thin layers of polymers thin films [177] and nanostructures of functional molecules [178]. For the spin-coating process the arrangement and adsorption of molecules with special functional groups on the surface can be achieved almost instantaneously depending on the rotation speed. Here, we show that this simple and widely used method can be used for the fabrication of regular arrays of β-glycine micro- and nanoislands with regular in-plane orientation of crystallographic axes of β-glycine on Pt substrates.

4.3.1. Thin Film Preparation

Glycine films were prepared by the spin-coating of glycine solutions. A drop of the glycine solution (50 ml and 0.13 M) was placed on the Pt-coated $Ti/SiO_2/Si$ substrate by a micropipette and then the substrate was rotated at a speed of 2000 rpm for 3 min to spread out and to simultaneously dry the solution. The centrifugal force pushes the solution to flow radially outward the center of rotation while decreasing its thickness, as the solvent

evaporates. As a result of this process, glycine micro- and nanoislands were grown by the evaporation and the spin-coated assisted process.

4.3.2. Structural Characterization of Thin Films

Figure 4.15 shows the representative optical morphology of the films, comprising the regions with ordered islands and distinguishable "grain boundaries" separated areas with different orientations of nanoislands. By the evaporation of the solvent during spinning, the fluid thickness is reduced to the point at which strong immersion capillary attraction arises between the particles that assists the self-organization of the particles into long-range ordered array of nanoislands [179]. Therefore, the ordering of the glycine particles at Pt surface by spin coating is controlled by the inter-particles and molecule-substrate interactions.

Large open voids appear randomly throughout the film due to dewetting phenomenon. Dewetting normally arises from fluctuations in the film thickness, and non-wettable nature of the substrate causes the film to rupture at random positions [180]. At the edge of holes liquid draws itself onto the crystal in order to minimize the amount of liquid in contact with the substrate and the rim thickness of these holes increases.

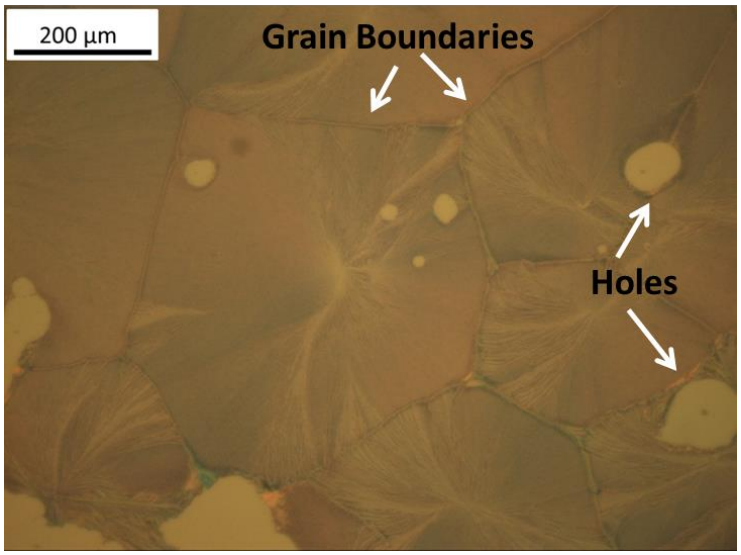

Figure 4.15. Optical image of β-glycine film.

Generally speaking, deposition of glycine on plane substrates as nano-/microscale islands via spin coating is a non-equilibrium process in which the delicate balance exists

between the centrifugal force, rate of evaporation and crystal growth rate. Such has the following advantages: fast fabrication time, preferential growth of useful β-phase, and easy control of nanoislands size and orientation relative to the center of the drop.

Raman spectroscopy was used to identify the structure of individual islands and direction of the crystallographic axes relative to the center of each grain. Analysis of the position of spectral peaks confirmed that all islands belong to ferroelectric beta phase. Inside each grain there is a spherulite-like structure [181]; these spherulites, growing from central parts, outward along the radial directions governed by four-fold symmetry arrangements of islands (Fig. 4.16a). By using the polarized Raman spectra we could prove that b- (polar) and c-axes of the film laid in plane of the substrate, and the c-axis laid preferably along the longest axis of each island (i.e. in the radial direction), while the b-axis was perpendicular. (Fig. 4.16b,c).

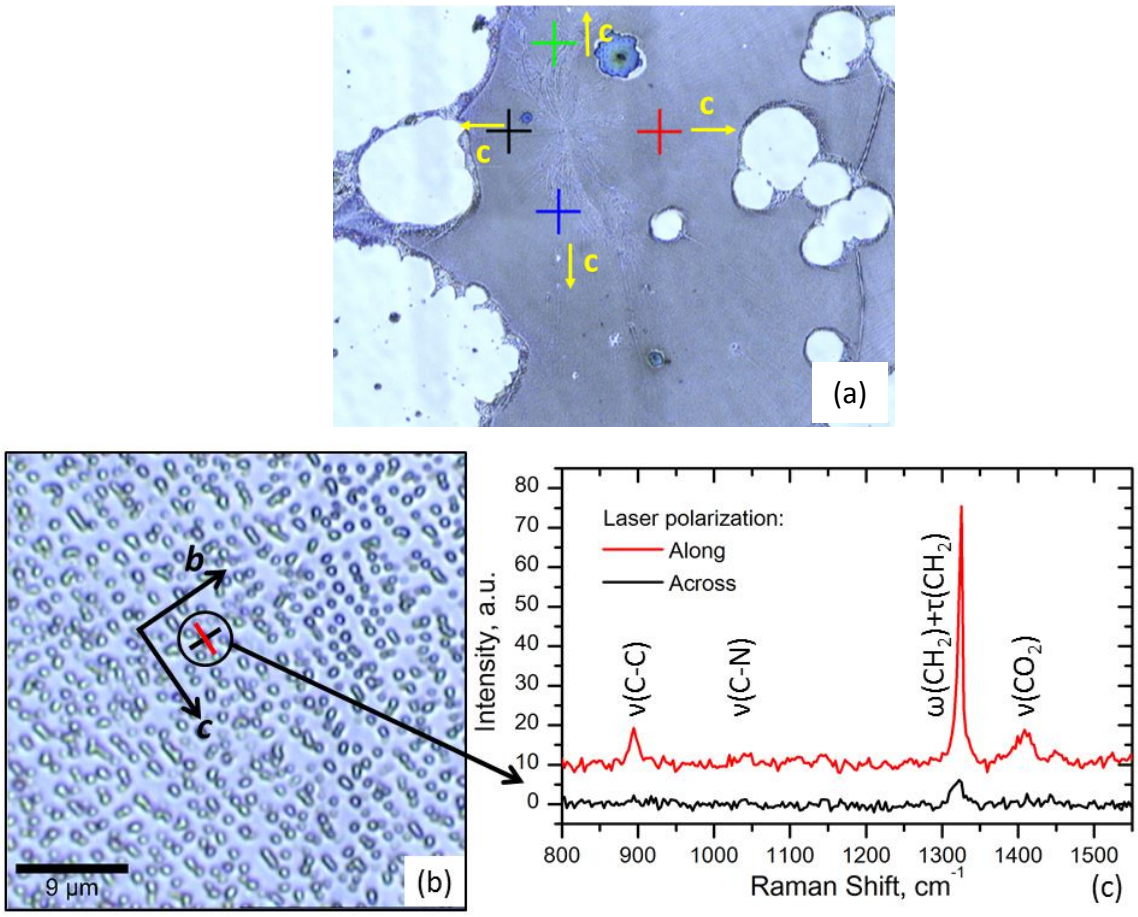

Figure 4.16. (a) Radial arrangement of the glycine islands and development of spherulitic structure. (b) and (c) Identification of the axes orientation of each glycine island by polarized Raman spectroscopy.

Important parameters that affect the structural formation of spin-coated crystals are the concentration of solution and spinning speed. With increasing concentration and decreasing rotational speed, the films become thicker and denser but less homogeneous [182]. However, we did not do any quantitative measurements the film thickness as function of the spinning speed and solution concentration.

Thus obtained glycine particles were stable under ambient conditions over a period of one year, perhaps due to its nanoscale dimension and good contact with the Pt substrate.

4.4. Summary

Single crystals of all three phases of glycine were grown from the solution at room temperature. Their polymorphic phase, crystalline structure, and stability were examined by combined methods of optical microscopy, X-ray diffraction, and Raman spectroscopy.

Due to inherent instability of β-glycine at ambient conditions, a simple method of stabilization of the β-phase is demonstrated based on the evaporation of aqueous solution on crystalline Pt(111) substrates. We have found that the interplay between the concentration of the glycine solution and crystallization effect of the surface results in the preferential growth of glycine β-phase with well-defined shape and morphology. These two parameters are suggested to be the major factors controlling the evaporation rate and growth kinetics. As a result, β-glycine needle-shaped crystals with the average size of $30 \times 200\ \mu m^2$ were grown on $Pt/Ti/SiO_2/Si$ under ambient conditions. No encapsulation in polymers or nanopores was indeed needed to maintain the stability of β-phase.

Glycine thin films were grown on Pt-coated Si substrates by spin coating method. The self-organization process during spin-coating creates the ordered particle arrays due to capillary and other forces. Film morphology is dominated by the “grains”, each composed of one spherulite-like structure. The orientation of crystal axes inside each grain area was determined by the precise analysis of the position of the Raman spectrum lines.

Chapter 5

Electromechanical and Non-linear Optical Properties of Glycine Crystals

Non-centrosymmetric crystals such as β-glycine (space group $P2_1$) and γ-glycine (space group $P3_2$) are of special interest for bioelectronics, biomechanics and bioMEMS applications. In this Chapter we attempt to analyze the electromechanical properties of both γ- and β-glycine forms to establish their piezoelectric activity and possible switching behavior.

The switching process and creation of elongated ferroelectric domains as well as dynamics of domains propagation under different voltage pulses with variable height and durations are studied in the ferroelectric phase of β-glycine. Thermodynamic theory is applied to explain the variation of domain length and aspect ratio under the voltage applied to the PFM tip. The process of domain backswitching is also investigated. In addition, piezoelectric activity and switching behavior are being theoretically approached by molecular modeling.

In the following of this Chapter, the non-linear optical properties of β-glycine are studied. Second harmonic generation (SHG) signal was compared with the crystallographic symmetry of β-glycine and with biomolecular modelling. Finally, possible applications of glycine crystals with controlled domain structure in various applications are discussed.

5.1. PFM in γ-glycine

The non-centrosymmetric structure of γ-glycine crystal was characterized for local piezoelectricity and possible ferroelectric properties. A detailed study of the piezoelectricity was carried out by in-plane (lateral) and out-of-plane (vertical) PFM. The out-of-plane PFM is measured by the piezoelectric response directed along the normal to the crystal surface, while the in-plane mode as shear response of the cantilever.

The crystals were cut parallel to the (100) and (001) planes (Fig. 5.1a). Piezoelectricity was studied on both polished planes of glycine by means of vectorial PFM. In general, PFM contrast confirms the polarization homogeneity on each surface and high enough crystallinity of the samples. The values piezoresponse amplitude and phase allows determining the orientation of the polarization *P* in each plane. In Fig. 5.1b,c the (100) surfaces show a significant in-plane (IP) signal with uniform contrast of phase which is reversed upon rotation of the crystal by 180 degrees. The plane cut normally to c axis (001) displays significant out-of-plane (OOP) contrast providing information about vertical

polarization component (Fig. 5.1d). Here again with rotation of the crystal at 180 degrees (along c direction), the vertical signal is reversed (Fig. 5.1e) (bright and dark contrasts: polarization pointing out and down of the plane, respectively).

Combination of all of these facts confirms the unipolar alignment of glycine molecules arranged to form a crystal down to a nm resolution and proves that the contrast is due to piezoelectric nature of the crystal. However, both planes of a sample were not switchable even up to 200 V. Thus, γ-glycine is a piezoelectric crystal with a unique polar direction axis along the c direction and without ferroelectricity, making it a potential candidate for piezoelectric and nonlinear optical (NLO) applications.

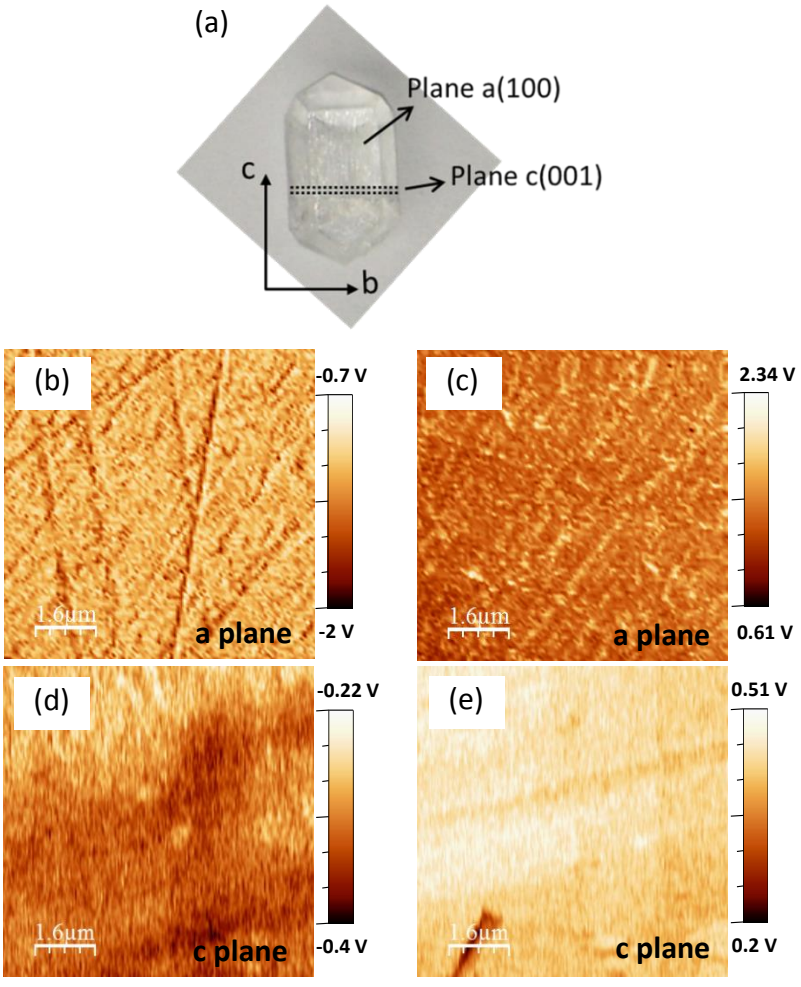

Figure 5.1. (a) The γ-crystal axes orientation and cutting directions (b) IP-PFM of (100) plane, (c) after 180° rotation, (d) OOP-PFM images for (001) plane, and (e) after 180° rotation. The positive and negative signals demonstrate opposite orientations of corresponding polar vectors.

5.2. PFM in Needle-shaped β-glycine

5.2.1. Domain Imaging

Piezoelectricity and domain structure of a needle-shaped β-glycine microcrystal were studied by using PFM. Figure 5.2a shows the position of the cantilever relative to the crystal during scanning. Fig. 5.2(b-h) presents typical topography and piezoresponse images (amplitude and phase) acquired on the surface of β-glycine microcrystals comprising several domain boundaries. According to the topography image (Fig. 5.2b), β-glycine grows in a layer manner and a number of defects are generated on the surface of the crystal. These topographic defects apparently correlate with the distribution of ferroelectric domains. Only an in-plane polarization (shear piezocontrast) was observed (Fig. 5.2c,d) with almost zero out-of-plane one (Fig. 5.2f,g). The bright and dark contrasts of the in-plane phase image (Fig. 5.2d) indicate an apparent 180^{o} phase difference and suggest an antiparallel polarization direction in adjacent domains (as shown in Fig. 5.2d by arrows). The in-plane (shear) signal is significantly reduced at domain walls as expected (Fig. 5.2e) [183]. This could be a result of domain wall clamping and averaging effect of the piezoresponse by the finite size of the tip [183]. A comparison of the in-plane piezoresponse with a single crystal x-ray diffraction data indicates that the spontaneous polarization of as-grown domains is parallel to the crystal axis *b* of the monoclinic phase of a β-polymorph.

There is only slight variation in the out-of-plane phase, so there is not enough evidence of out-of-plane domains (Fig. 5.2g). However, there is an increase in the out-of-plane signal for charged domain walls only in the situation when the cantilever lever is parallel to the charged domain walls (Fig. 5.2f,h). In order to find the origin of this response, the sample was rotated physically as explained below.

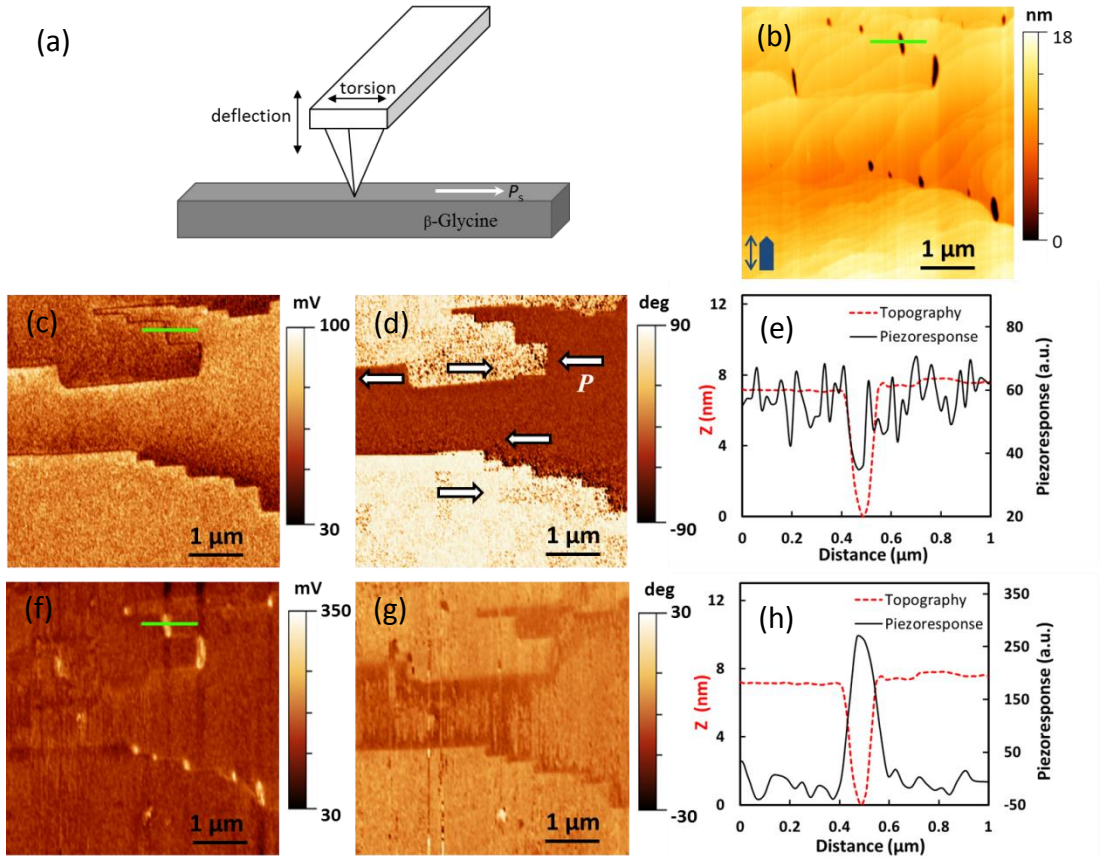

Figure 5.2. (a) Schematic of cantilever position on a needle-shaped β-crystal, (b) Topography, (c) LPFM amplitude, (d) LPFM phase, (e) Cross-sections across the domain wall on the topography and LPFM amplitude images (marked by green line), (f) VPFM amplitude, (g) VPFM phase, and (h) Cross section across the domain wall on the topography and VPM amplitude.

Comparing piezocontrast in the vertical and lateral images and considering the geometry of the PFM tip and crystal axes allowed revealing information about the spontaneous polarization direction of the crystal and boundaries [184]. When the cantilever is perpendicular to the long axis of the crystal, the in-plane contrast is maximal (Fig. 5.2a). After rotating the crystal (180°), the signal will be reversed. Upon rotation the sample at 90 degrees (Fig. 5.3a), in-plane contrast disappears inside domains and the charged domain walls, which are now perpendicular to the lever, give enhanced in-plane response (out-of-plane signal is absent), which is coincident with topography (Fig. 5.3b-d). It confirms that inside the domains spontaneous polarization lies in the b direction of the β-phase crystal (Fig. 5.2a). The arrows show the orientation of the polarization with respect to the domain wall

(Fig. 5.3c). This means that the response from the boundaries in Fig. 5.2f is not due to the true out-of-plane polarization vector or topography effect, but rather to some buckling of the cantilever. For the case of IP polarization vectors parallel to the cantilever axis, the shear strain from the sample induces buckling oscillations, which are detected as OP signal [185]. This explanation was confirmed by domain switching experiments as described below.

These observations suggest the presence of a complex structure of charged domain walls, which includes a thin layer with polarization directed parallel to defect (Fig. 5.3.e). This is the reason why domain wall becomes seemingly wider. In the in-plane phase image (Fig. 5.3.d), one can notice the areas with the opposite contrast, which is obviously connected with opposite signs of the related "head-to-head" and "tail-to-tail" charged walls.

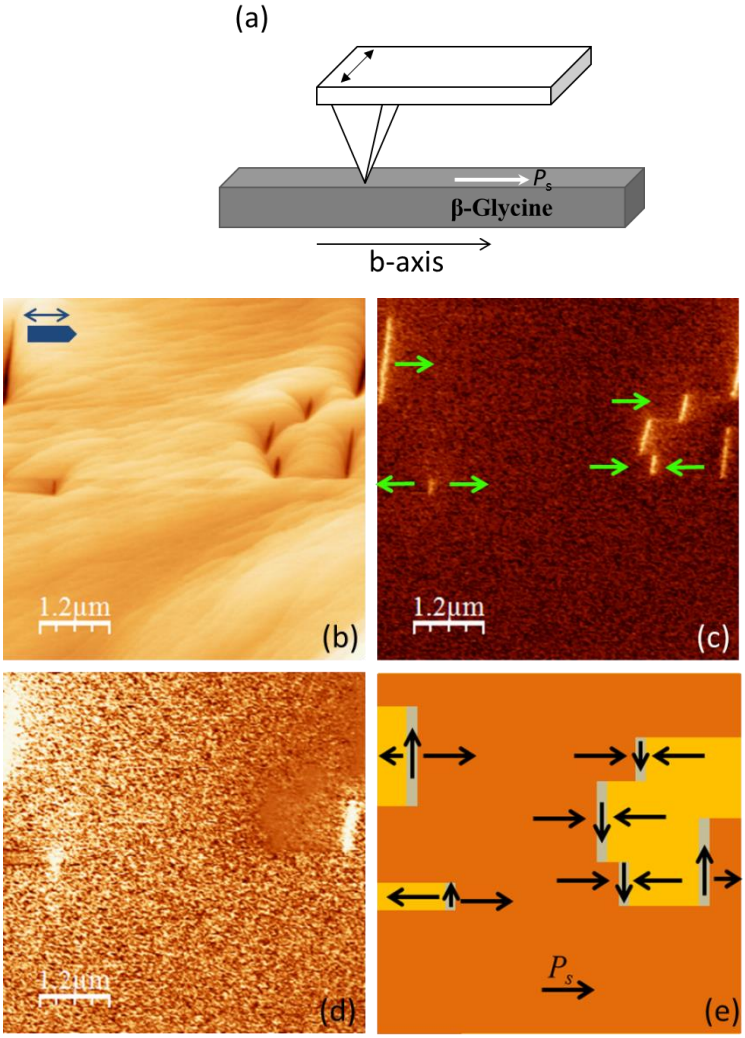

Figure 5.3. (a) Schematic of the cantilever position on a needle-shaped β-crystal, (b) Topography, (c) LPFM amplitude, (c) LPFM phase and (d) A cartoon sketch of ferroelectric domain walls according to PFM (overlaid) and its derivative images.

Thus, the domain walls in β-glycine are apparently true 180^o domains separating domains with the polarizations parallel to the domain wall plane and charged domain walls in which polarization discontinuity leads to an additional energy associated with such domain configurations. The combination of both domain types represents a typical step-like domain structure similar to that recently observed in α-6,6'-dimethyl-2,2'-bipiridinium chloranilate [186].

Figure 5.4 shows a part of the step-like domain structure overlaid on the 3D topography image. It clearly indicates that the 180^o domains are mostly coincident with the cleavage planes of the crystal. The steps in topography correspond to the atomic planes of β-glycine. Since the crystal surface was not polished, it may be suggested that stabilization of 180^o domain walls occurs at these growth defects and their density is controlled by the density of atomic steps at the surface. It is natural to propose that β-glycine (grown at room temperature below Curie point) could decrease the domain wall energy by pinning 180^o domain walls at the vertical steps on the surface (Fig. 5.4). These thermodynamically stable domains may not be easily switched under an applied electric field and thus the macroscopic remanent polarization can be reduced as compared to the single domain state [186].

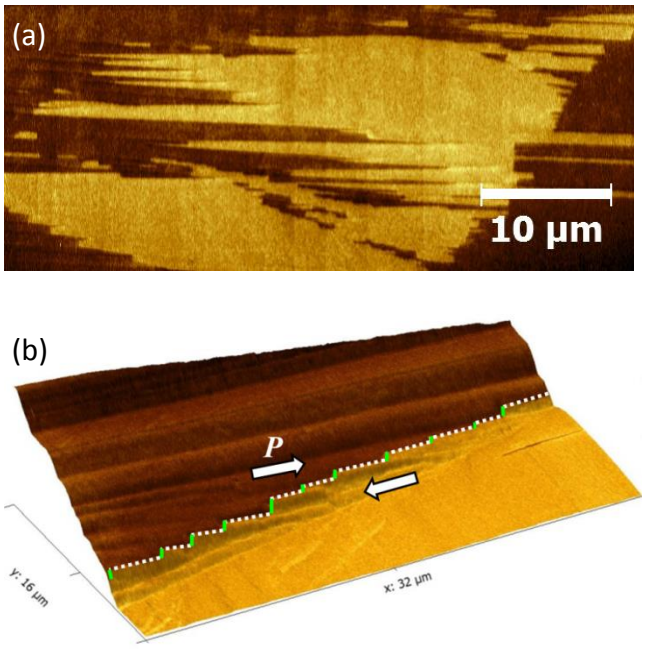

Figure 5.4. (a) LPFM contrast for the as-grown state, (b) Topography overlaid on the PFM contrast. Green and white lines represent charged and neutral domain walls, respectively.

The distinct feature of our β-glycine microcrystals is the presence of a large number of charged domain walls (either head-to-head or tail-to-tail). In uniaxial ferroelectrics, 180° domain walls typically separate antiparallel domains with polarization vector *parallel* to domain plane, so as to avoid high electrostatic energy associated with polarization discontinuity at the domain wall [44]. Consequently, charged domain walls have been rarely observed in ferroelectric materials, *e.g.* in $PbTiO_3$ crystals [187], in PZT thin films [188] and, recently, in uniaxial organic ferroelectrics [44]. As-grown glycine crystal has both antiparallel (neutral) and charged ferroelectric domain walls appearing as a series of steps as shown schematically in Fig. 5.5. As seen from the comparison of PFM amplitude and topography cross-sections (Fig. 5.2e), the initial charged domain boundaries in the crystal are always associated with the topography trenches of about 6-7 nm in depth. This is an indication of the existence of topological defects which can be associated with the high electrostatic field compensated by electronic or ionic charges trapped at defect sites [189]. On the other hand, the associated strain at the charge domain wall is about 0.1% and corresponds to the change of crystal dimension due to d_{31} piezoelectric effect under an electric field of about 5 MV/cm. This naturally explains the existence of trenches (not protrusions) on the surface due to the negative sign of d_{31}. Unfortunately, our microcrystals were too small to conduct conventional Sawyer-Tower polarization hysteresis measurements.

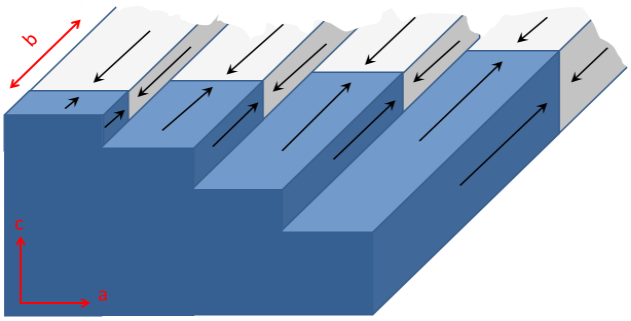

Figure 5.5. Schematic of the domain configurations and polarization distribution on the growth steps of glycine crystals.

By calibrating lateral displacement using an AFM scanner it was possible to determine the absolute value of the effective shear piezoelectric coefficient ($d_{15\text{eff}}$) inside the domain. The in-plane sensitivity was calculated based on the geometry of the cantilever and out-of-plane deflection sensitivity was measured as described by Peter *et al*. [190]. The

piezoresponse signal of β-glycine was measured at a point inside the domain while varying the amplitude of the *ac* bias from 0 to 15 V. The effective shear piezoelectric coefficient was calculated directly from the slope of the acquired curve and in-plane torsional sensitivity of the cantilever [190]. The value varied from point to point with an average effective coefficient of about 6 pm/V. It should be noted that this value cannot represent the true bulk coefficient and should be used with caution to evaluate piezoelectric activity of the amino acid crystals. Still this value is significantly greater than that of the corresponding coefficient of quartz (d_{14} = 0.76 pm/V) [191] and similar to that of ZnO [192].

5.2.2. Switchability of β-glycine

In order to confirm polarization switchability in β-glycine, an external electric field was applied locally via a PFM tip to the crystal with in-plane polarization and domain switching was controlled by varying the amplitude and duration of *dc* bias pulses [193]. It is well known that the electric field created via PFM tip is inhomogeneous and has a maximum intensity in a direction perpendicular to the sample surface. Due to this effect, it is possible to create artificial domains with the polarization perpendicular to the ferroelectric surface and monitor their switching kinetics by measuring the domain diameter versus applied voltage [194,195]. Since switching in uniaxial ferroelectrics is limited to 180° reversal of the polarization, the field can create only a 180° domain with polarization parallel to the surface in in-plane domains. Recently, Pertsev and Kholkin [196] have theoretically shown that the 180° in-plane polarization switching can be observed in uniaxial ferroelectrics when the initial polarization is *parallel* to the sample surface. In this approach, the PFM tip is represented as a line of charges [195] extending from $\mathrm{Z} = h$ to $\mathrm{Z} = \mathrm{H}$ (h is the distance between the tip apex charge and the crystal surface and H is the total tip height) and potential distribution created by the tip inside the ferroelectric crystal can be written in the form:

$$\emptyset_{tip} = \frac{V}{\ln\left[\frac{2H\sqrt{\varepsilon_x\varepsilon_z}}{\left(r_{tip}\,\varepsilon_{ext}\right)}\right]} \ln\left[\frac{H-\sqrt{\varepsilon_x/\varepsilon_z}z+\sqrt{x^2+\left(\varepsilon_x/\varepsilon_y\right)y^2+\left(H-\sqrt{\varepsilon_x/\varepsilon_z}z\right)^2}}{h-\sqrt{\varepsilon_x/\varepsilon_z}z+\sqrt{x^2+\left(\varepsilon_x/\varepsilon_y\right)y^2+\left(h-\sqrt{\varepsilon_x/\varepsilon_z}z\right)^2}}\right] \qquad (5.1)$$

where x is a coordinate parallel to the polar axis (in our case b direction), z is the coordinate perpendicular to the surface, r_{tip} is the effective radius of the tip, $\varepsilon_{\mathrm{ext}}$ is the dielectric

permittivity of external media, and V is the bias applied to the tip. The dielectric response in the surface plane is supposed to be anisotropic ($\varepsilon_x \neq \varepsilon_y$), where ε_x is the dielectric permittivity along the polar x direction and ε_y is along the nonpolar one. The distribution of lateral field of the tip should be calculated as the derivative of potential $\emptyset_{tip}$ with respect to *x*:

$$E_x^{tip} = -\partial\emptyset_{tip}/\partial x. \qquad (5.2)$$

We calculated the lateral component of electric field intensity at the sample surface and at two different depths (10 and 20 nm) by using Eq. 5.2 and applied voltage 90 V. As expected, the inhomogeneous electric field induced by the tip in x-direction (E_x^{tip}) has opposite signs at right and left sides from the tip, reaching a maximum at a distance close to the tip and then decreasing slowly with distance (Fig. 5.6a). Therefore, the surface domain would grow only at one side of the PFM tip depending on the initial polarization of the crystal and the sign of applied electric field (Fig. 5.6b). Changing the bias sign reverses the direction of electric field produced by the tip and, therefore, creates domain in opposite direction (Fig. 5.6c). Interestingly, recent observation of the in-plane switching in congruent $LiNbO_3$ single crystals demonstrates much richer phenomena, where in-plane domains grew in the same direction after the application of voltages of opposite signs [197].

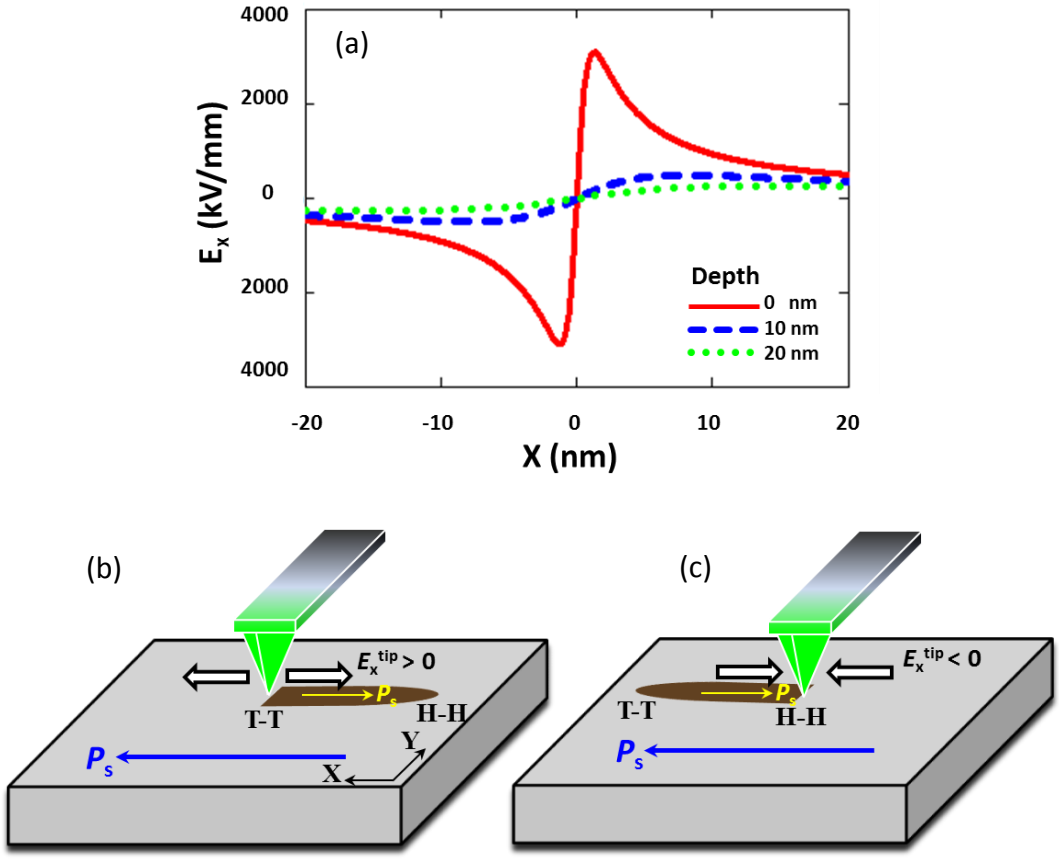

Figure 5.6. (a) The electric field intensity E_x^{tip} produced by the tip on the surface and with different depths in the bulk along the polar x axis. (b) and (c) Schematics of the expected in-plane domain configuration recorded by PFM tip with positive and negative bias, respectively. T-T is tail to tail and H-H is head to head configurations.

Indeed, after the application of a high enough *dc* bias to the tip in contact with the surface, a new 180° domain is observed being sufficiently stable after switching. Nascent domains have a typical rectangular shape with high aspect ratio and wedge-shaped end (in order to decrease electrostatic energy associated with charged domain wall [44]). Place of application field is marked with blue arrows in Fig. 5.7 d. We note that the charged domain walls are not associated anymore with surface defects (*i.e.* with the topography change) and, therefore, electrically switched domains were not that stable as compared to the natural ones appearing during crystal growth. It is speculated that high electrostatic field associated with them could be partly compensated by the external rather than by internal charges from

defects. It has been found that as-grown charged domain walls cannot be moved even under very high electric bias applied to the tip.

Although there are no features on the topography, while there is enhanced OOP signal in charged wall as shown in VPFM amplitude and cross section across the domain wall (Fig. 5.7e,g). Therefore, it confirms again that OOP signal in a charged wall is not due to a surface but rather to a bulk effect.

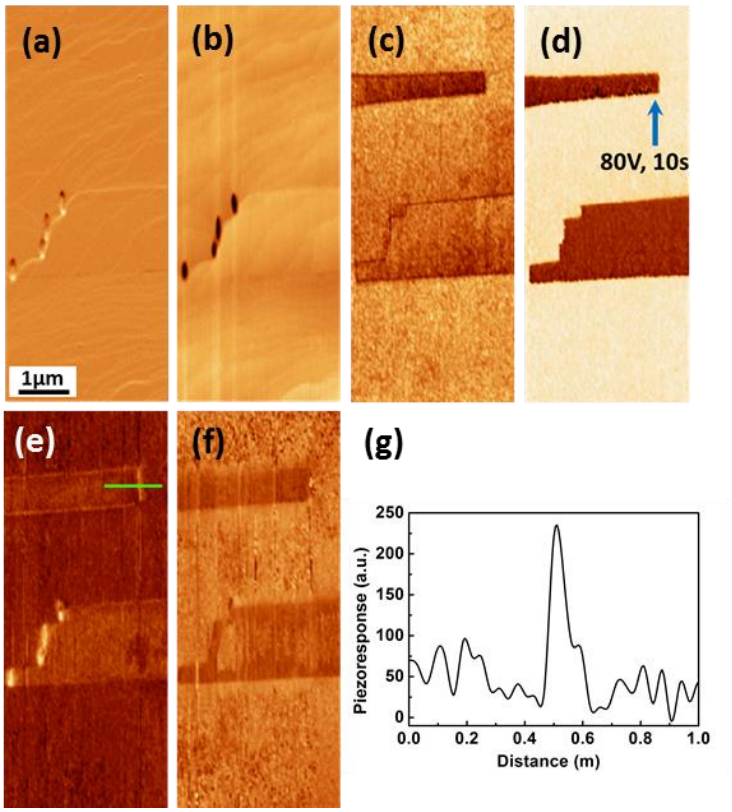

Figure 5.7. PFM image of the domain structure of the crystal after the application of an external field, (a) Surface deflection, (b) topography, (c) LPFM amplitude, (d) LPFM phase, (e) VPFM amplitude and (f) VPFM phase, (g) Cross-section along the domain wall (green line) on the amplitude profile. The arrow indicates the probe contact regions in the process of writing.

Figures 5.8a and b represent domains appearing after the application of -90 V to the tip for two opposite polarization states and different pulse durations. The direction of the nascent domain is sensitive to the initial polarization direction and changes to the opposite one upon crystal rotation at 180^{o}.

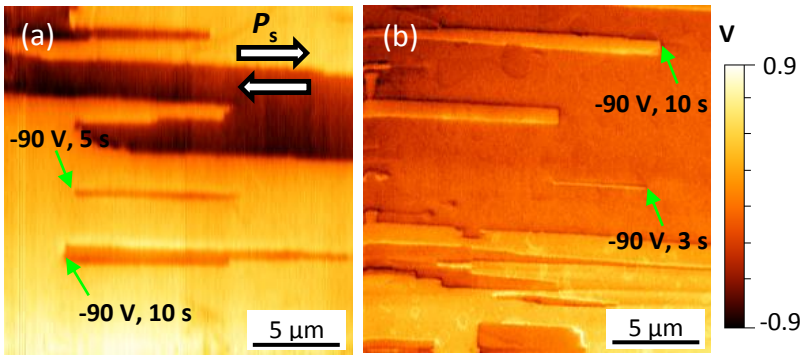

Figure 5.8. LPFM image of domains after writing in bright (a) and dark areas (b) by tip voltages of -90 V with different pulse durations (the arrows show the contact points of the AFM tip).

Domains lengths were found to be dependent on the amplitude and duration of the applied voltage pulse. Figure 5.9 illustrates the voltage dependence of the domain length for fixed bias pulse duration (10 s). Independently of the voltage pulse duration, the critical voltage was about 65 V for both orientations of the initial polarization. Small variation of critical voltages (±5 V) probably originates from different defect structure (density, defect type) under the tip.

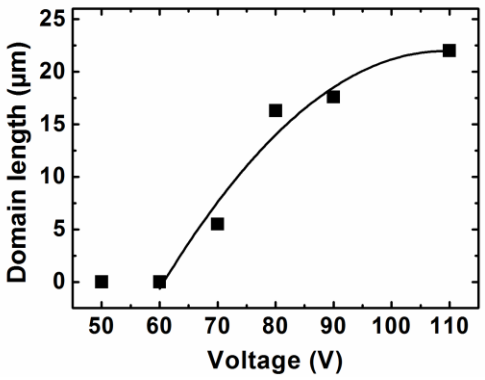

Figure 5.9. Domain length as a function of applied voltage for fixed pulse duration (10 s).

The value of threshold voltage needed for the appearance of domains on non-polar surface is more than three times greater than that necessary for the switching on the polar surface in glycine ($V_{cr} \approx 20\,V$ according to Ref. [15]). There are two reasons for that. First, due to dielectric anisotropy of the surface ($\varepsilon_z/\varepsilon_x > 2$) , the maximum value of E_z is about two times higher than that of E_x, similar to the case of the non-polar surface of uniaxial $LiNbO_3$. Second, back switching effect could be more pronounced for in-plane domains

which are not sufficiently stable due to incomplete polarization screening [197]. Apparently, domains switched under lower voltages are unstable and the initial polarization state is recovered after the external field is switched off. This happens due to fundamental instability of the charged domain which cannot be completely screened with absence of the slow bulk screening processes [198].

The domain lengths were also found to depend on the duration of the applied voltage as seen in Fig. 5.10a. The threshold time was about 2 s. At shorter times the domains were not in the equilibrium and switched back after the field was removed. Domain wall velocity was calculated based on the dependence of the domain length on switching time ($v = dL/dt$) and is plotted as a function of the domain length in Fig. 5.10b. Domain wall velocity significantly decreases with increasing domain length since the lateral electric field decreases with asymptotic behaviour ($E_x^{tip} \sim 1/x$) with distance from the tip [196].

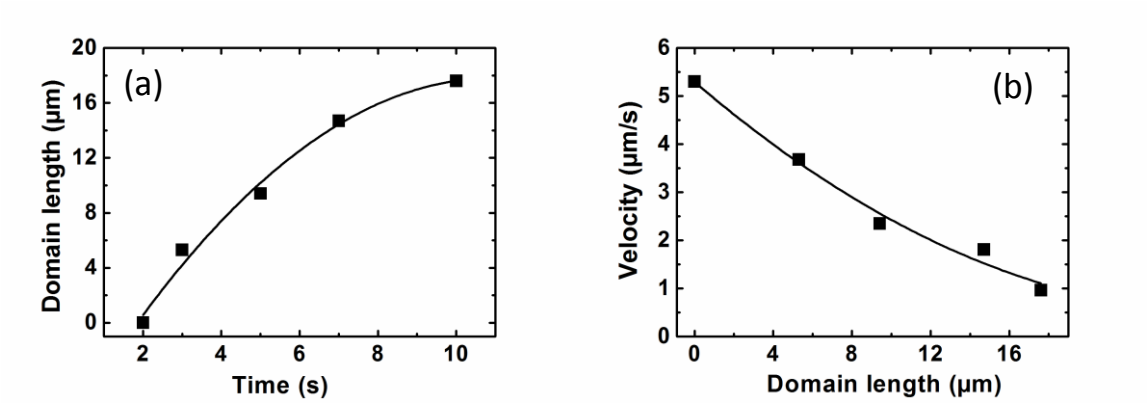

Figure 5.10. (a) Domain length as a function of writing time for the applied voltage -90 *V*. (b) Domain wall velocity of as a function of domain length for the applied voltage -90 *V*.

Ferroelectricity in organic crystals arises from the collective transfer of electrons in charge-transfer (CT) complexes [199] or protons transfer in hydrogen bonded crystals [200], which are different from ionic displacements in perovskite structure. The spontaneous polarization of glycine crystal comes from the interaction of permanent dipole moments of glycine molecules in the volume, but polarization of each chain can be inverted by dynamics of the intermolecular N-H…O bonds, similar to proton tautomerism of O-H…O bonds in croconic acid [1] or N-H…N bonds in benzimidazole derivatives [201]. This property is attributed to the amphoteric nature of glycine molecule which can donate or accept proton to each other.

With increasing voltage, the domain length reached high values, e.g., ~17 μm for 90 *V*, or even more as shown in Fig. 5.9. At such distances the associated driving field from the tip is very weak or practically zero (according to E_x^{tip} equation, electric field under the tip of the probe is about 3000 kV/mm at the voltage of 90 V, the field at a distance of $r \approx 2$ μm from the probe decreases to 5.2 kV/mm). Thus, the domain wall is not driven anymore by the electric field from the tip. This observation can be explained by the domain breakdown phenomenon, a domain growth process which was proposed by Molotskii *et al*. [202]. It states that the main driving force for domain propagation is a decrease in the depolarizing field energy of the system, rather than direct effect of the electric field induced by the tip. Probably in the case of glycine, the domain length increases with consecutive rearrangement of H atoms position in the intermolecular N-H…O bonds to satisfy the minimum free energy condition.

The stability of the written domain structures is important for the application of ferroelectrics for memories. In glycine, the domains are stable for a short time only and then their length slowly decreases to reach stable configuration or sometimes they fully disappear similar to the case of single-domain strontium-barium niobate SBN crystals [203]. However, the time taken for the nucleated domain to switch back after removal of the field is a few hundred times shorter than the intrinsic switching time.

5.3. Theoretical Calculations

The equilibrium domain size under the voltages above the critical one was determined using a theoretical approach developed in Ref. 196 and the results were compared with the experimental results in Fig 5.9. To calculate the dimension of such in-plane domains, a coordinate system with the z axis perpendicular to the surface and the x axis parallel to the polar crystallographic direction is considered. The model is based on the minimization of the total free energy after the polarization switching inside the domain in the form

$$\Delta F = U_{dw} + U_{dep} - 2P_s \int_{\Omega} E_x^{tip}(x, y, z)\, d\Omega, \qquad (5.3)$$

where U_{dw} is the self-energy of the domain boundary separating the new domain from the surrounding crystal, U_{dep} is the energy of a depolarizing field created by the polarization

charges on the domain surface and the last term represents the work W_{tip} done by E_{tip} during the polarization reversal inside the domain volume Ω.

By minimizing the free energy numerically, critical bias voltage (V_{cr}) was evaluated and the domain lengths were calculated at and above critical voltage using the glycine crystal parameters calculated in Ref. 204: $P_s \approx 0.11\ C/m^2$, $\varepsilon_x \approx 5$, $\varepsilon_z = \varepsilon_y \approx 18$, and domain surface energy density $\gamma = 0.001\ J/m^2$. In our calculations we considered the tip radius $r_{tip} = 30$ nm, H = 10 μm, and h = 1 nm. The critical voltage was about 25 V for glycine while PFM scanning indicates domain appearance after the application of much higher voltage (~ 65 V). This discrepancy is might be due to instability of domains appearing under the lower voltages and their backswitching after the field removal [44]. Figure 5.11 compares the experimental and calculated domain lengths as a function of the voltage applied to the tip. At high voltages the experimental domain lengths are very close to those predicted by the thermodynamic theory. However, the experimental values at low voltages deviate from the expected theoretical behavior and domain sizes are smaller than predicted ones.

This thermodynamics model provides equilibrium domain dimensions which are difficult to reach in real experimental conditions because of insufficient screening and consequent backswitching after the field removal. Additionally, the thermodynamic threshold voltage may be smaller than the observed one because of the voltage drop across a low-permittivity layer at the sample surface, which is not taken into account in the theory.

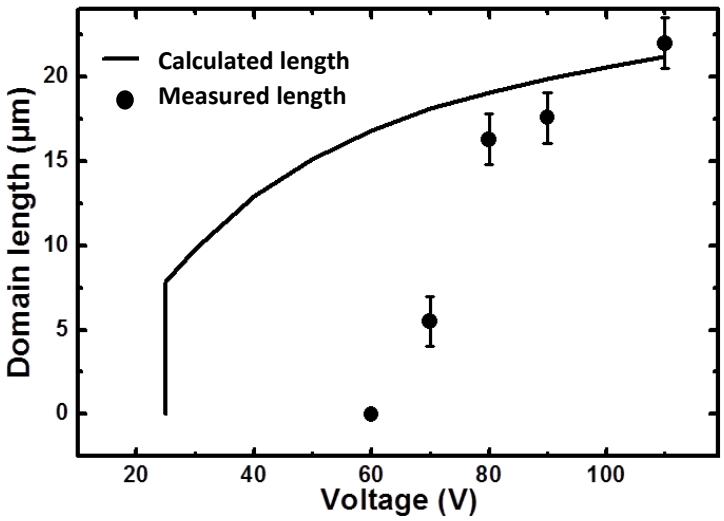

Figure 5.11. Measured (filled circles) and calculated (curve) domains length in the β-glycine as a function of applied voltage.

As mentioned in Fig. 5.7 the artificial domains are not associated with topography pits and therefore they are not very stable and decay under the driving force originated from the surface energy of the domain wall and the depolarization field energy after removing the switching voltage [205]. The decay of domains is a nonequilibrium thermodynamical process proceeding so as to lower the free energy of the system. It is affected by initial domain size, temperature, crystal defects, which can pin the domain walls, etc [206].

The decay process of domains with different length was measured after poling. Decay processes depended on the domain size. For longer domain as shown in Fig. 5.12a, firstly, the domain width becomes uniform through the entire domain, while the length remains almost unchanged. Then it shrinks relatively slowly in both directions. 80 minutes later, when it reaches to a critical size, rapidly drops to the as original state. For domain with smaller size (Fig. 5.12b), it is very unstable and totally switches back to the original state in less than 20 minutes which reveals a fast decay process. Therefore, the larger domains survive more due to decrease in the domain decay driving forces. The discrepancies between theoretical and experimental values in the lower voltage (Fig. 5.11) might be due to higher speed of domain size decay in the first few minutes after switching off the field in smaller domains relative to larger size. It should be mentioned that the domain stability can also be influenced by the distance of neighboring domains which is important in the fabrication of periodically poled crystals by SPM poling method for applicability in electro-optical devices.

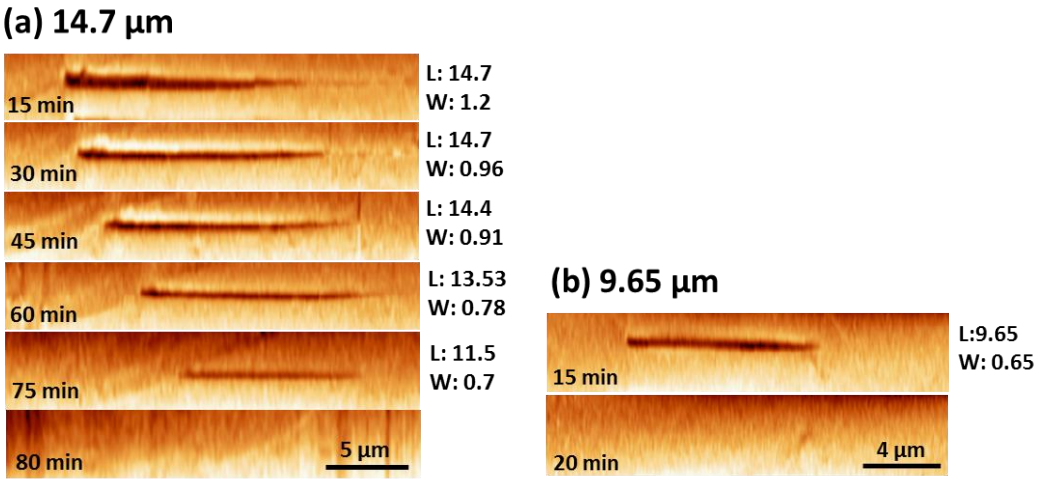

Figure 5.12. The decay process of domain with length of (a) 14.7 µm and (b) 9.6 µm as a function of time. L and W are the length (µm) and width (µm) of domain in each time.

In our experiment, the domain width is not constant (wedge-like). Thus, we used the average domain width by dividing the measured reversed domain area by the domain length.

5.4. Molecular Modelling

Computational modelling of both glycine polymorphic phases (β and γ) were performed using a combined method with local density approximation (LDA) first principle calculations of crystal structures on Linux cluster and with molecular semi-empirical PM3 calculations by HyperChem 8.0 [207]. The structural models obtained and the physical data (dipole moment, polarizations, dielectric permittivity, electrostriction and piezoelectric coefficients, etc.) were computed and compared with experimental data obtained by PFM.

Figure 5.13 shows schematics of the individual glycine molecules dipole moment. Each glycine zwitterion contains a dipole moment directed from oxygen to nitrogen atom.

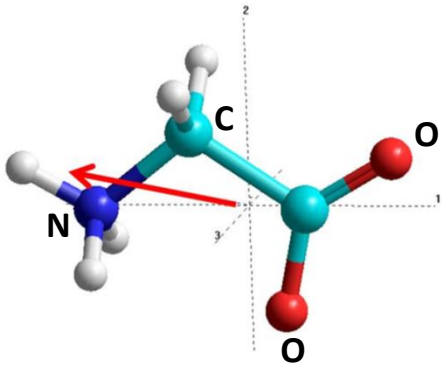

Figure 5.13. The dipole moment orientation of an individual glycine molecule.

The network of hydrogen bonds plays an essential role in organization of the crystal structure of glycine. Figure 5.14 displays both molecular crystallographic structures for β- and γ-glycine in two projections with marked hydrogen bonds network and resulting dipole moment. According to the modeling results, γ-glycine crystals consist of molecules in the form of zwitterions linked through NH…O hydrogen bonds. Molecules form triple helices around the 3_1 screw-axis passing through the c axis; these helices are linked together by the lateral hydrogen bonds, forming a three-dimensional noncentrosymmetric network of hydrogen bonds. Therefore, for γ-glycine, crystal structure does not consist of layers, but is a three-dimensional hydrogen-bonded network with total dipole moment and polarization strongly oriented along c (OZ) axis. Each nitrogen atom is surrounded by oxygen atoms, and

each oxygen atom by nitrogen atoms, so the effect of such bonding will be enhanced by electrostatic forces between oppositely charged groups. The calculated value of polarization by unrestricted Hartree-Fock (UHF) PM3 method for modelled molecular cluster from 27 individual glycine molecules shows that polarization $P \approx P_z = 0.17$ C/m^2 for this γ-glycine polymorphic crystal structure. The calculated volume of γ-glycine lattice unit cell is V = 219.8 A^3.

The molecular arrangement in the crystal lattice of β-glycine is quite different with γ-form. In the β-polymorph, we have layered structure. Zwitterionic glycine monomers are linked in single polar layers in XOZ plane and hydrogen bonds link the single polar layers along the monoclinic b-axis with alternating chain orientations and create a non-centrosymmetric structure ($P2_1$ space group, Z = 2) [208]. A schematic diagram of the β-glycine crystal structure is shown in Fig. 5.14. In this case, the dipole moment has several components, which are oriented at various angles to the main axis at each layer with oppositely directed and compensated components in ac (XOZ) plane. But the components along OY axis are summed up and the total polarization is directed along OY axis. The calculated values of the polarization components are smaller than for γ-glycine and have on average $P \approx P_y \approx$ 0.1...0.12 C/m^2.

The specific features of all glycine phases are related to their hydrogen-bonded network system. There are two main types of H-bonds in β-glycine: within layer: H-bond with length L ≈ 1.179 Å and inter-layer: H-bond with length L ≈ 2.75 Å. As derived from IR-experiments [209], hydrogen bonds within the layer are stronger than the inter-layer ones in β-glycine. In addition, the strongest hydrogen bond in the β-form being weaker than the weakest hydrogen bond in the γ-form. Such structural features lead to an easier mobility of the glycine molecule in β-glycine crystal under external electric field as compared to γ-glycine where each individual molecule is fixed in a more stable position. The calculated volume of the β-glycine lattice unit cell is V = 158.9 A^3 which is smaller as compared to γ-glycine.

The estimation of the coercive electric field for γ-glycine yields a higher value $E_c \approx$ 30...80 MV/cm along c (OZ) axis, and it is hard (almost impossible) to switch polarization in this case. For β-glycine, we obtain smaller value of the coercive electric field $E_c \approx$ 10…15 MV/cm for the P_y polarization component (Fig. 5.15), which is much smaller and switching

phenomena are possible. This fact means that the individual glycine molecule in β-glycine structure moves easier and finds new stable positions under a relatively small *dc* field.

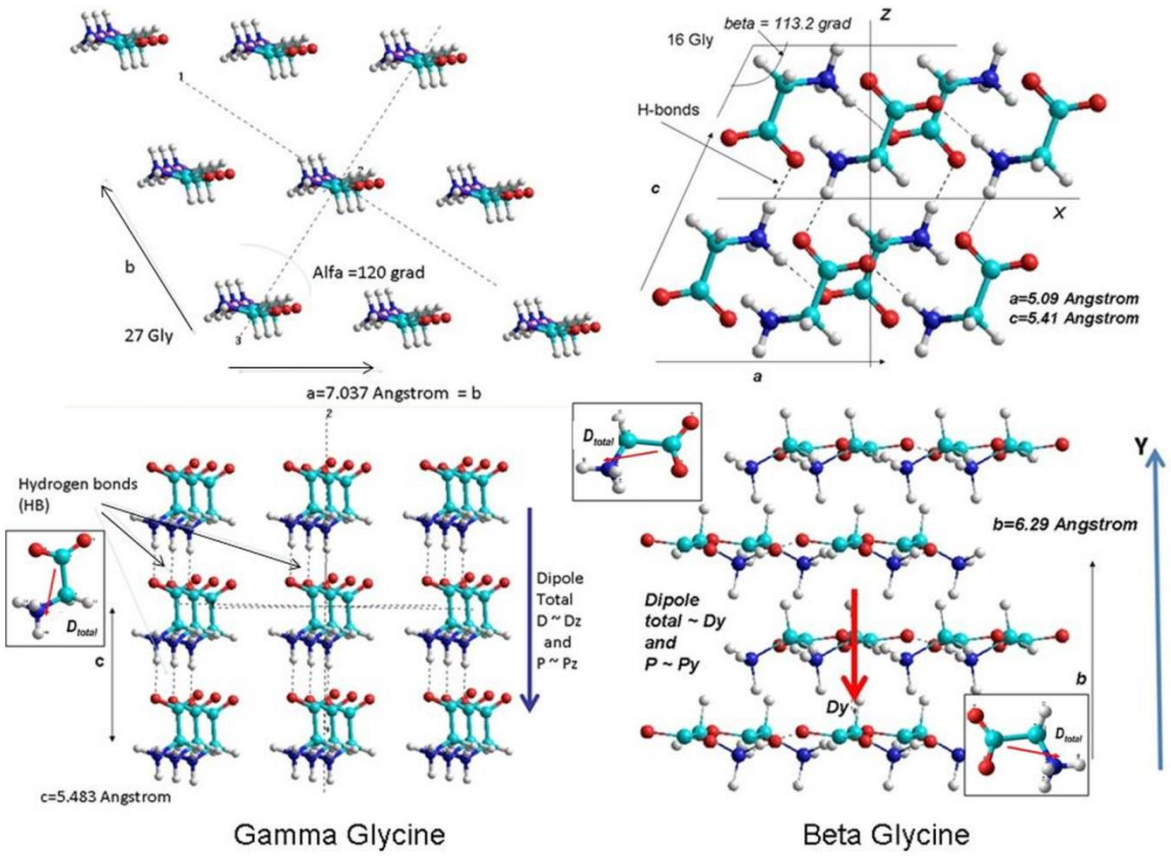

Figure 5.14. Molecular models of two polymorphic glycine (β and γ) crystal structures for two projections (along a and c axes) with marked hydrogen bonds network and total dipole moment.

Figure 5.15 represents the calculated polarization hysteresis loop for β-glycine. For the proposed molecular model of β-glycine the calculation procedure is not so easy and stable, because this cluster consists of only 16 individual glycine molecules and under applied electric field along OY axis some molecules, which are close to the surfaces of the cluster, are subject to non-uniform total electric field and, as a result, the convergence of calculations is far from regular and very good in this case. But, nevertheless, this model allowed us to estimate several important quantities and to obtain very good agreement with the experimental data.

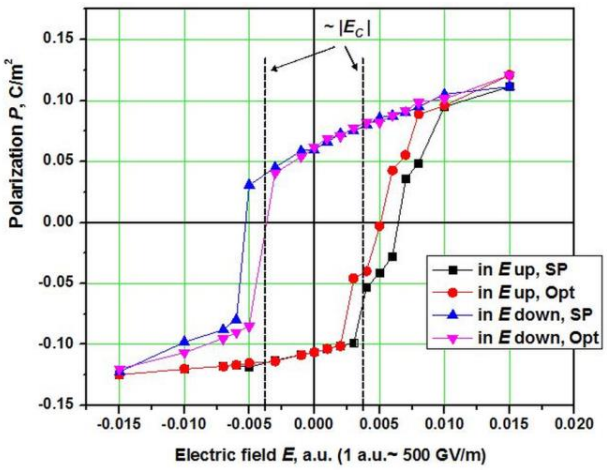

Figure 5.15. Calculated hysteresis loop for molecular model of β-glycine crystal structure with average coercive field E_c ~ 0.003 a.u. ~ 1.5 GV/m. SP and Opt are single point calculations (at the fixed position of each atom of the modelled molecules) and optimization of molecular geometry under a varying electric field, respectively.

First, the polarizability ($\alpha = \Delta D/\Delta E$) was found to be in the range α ~ 44…56 Å^3 ~ (4.8…6.1)*10-39 Cm^{2}V^{-1} for our molecular cluster from 16 individual glycine molecules. These data are close to the reported ones [210]. Second, we determined the electrostriction coefficient in the OY direction Qy ($Q = s/(\Delta P)^2$, where $s = \Delta V/V$), which equals (in absolute value) to Qy ~ 3.87 m^{4}C^{-2} and in perpendicular direction Qyx ~ 1.0 m^{4}C^{-2}. These values are close to those of other organic crystals with similar structure [211]. Using Clausius-Mosotti relation ($\varepsilon = (1 + 2k)/(1 - k)$, where $k = \alpha/V$) [212] we estimated the permittivity ε = 5, which is also close to experimental data (ε = 6 [213]).

Then, using a well-known linearized electrostriction relation d = 2εε$_0$QP [211] we roughly estimated apparent piezoelectric coefficient in OY direction, which could correspond to the longitudinal piezocoefficient d_{33} in this case. The obtained values of piezoelectric coefficients are: d_{33} ~ -8.2 pmV^{-1} and d_{31} ~ -8.5 pmV^{-1} for β-glycine. The measured shear piezocoefficient for β-glycine is d_{15} ~ 10 pmV^{-1} which is close to our calculations in absolute magnitude.

Using these data we also estimated the same quantities for γ-glycine. Assuming for simplicity that along Z axis Qz = ~ (0.5 – 1.0) m^{4}C^{-2} we obtain d_{33} ~ (5.8 – 11.6) pmV^{-1} (pCN^{-1}). This result is in line with the experimental value d ~ 7.4 pCN^{-1} from Ref. [213]. As a

result, we can conclude the β-glycine crystals should be easier switchable and, consequently, demonstrate apparent ferroelectric properties. On the contrary, γ-glycine is not easily switchable, but has better piezoelectric properties.

All in all, these computed data and obtained switching properties for both models of β- and γ-glycine polymorphic structures are fully in line with the experimental observations in PFM experiments.

5.5. PFM in Dendrite-type β-crystals

As mentioned in Chapter 4, the other morphology of β-phase that was found on the Pt substrates is dendrite-type. Figure 5.16 shows optical picture of part of dendrite crystals under polarizers light, different areas have distinguishing colors.

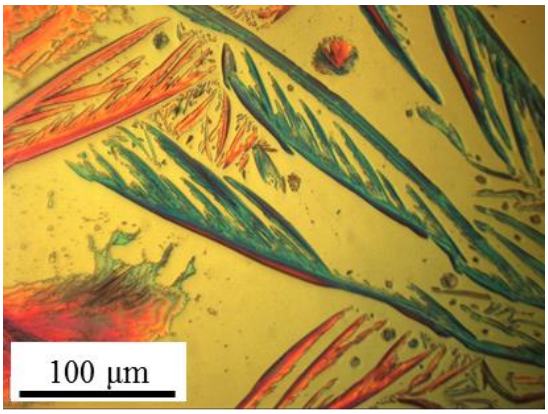

Figure 5.16. Optical microscopy image of dendrite crystals of β-glycine.

Dendrite crystals exhibit mainly twinned morphologies and their trunks are split in the centre. Most of the dendrites grow and expand further by not symmetrically branching mechanism, while side branches and secondary branches also show sequential twining.

Piezoresponse Force Microscopy confirmed that the dendrite-type β-glycine crystals exhibit piezoelectricity with both out-of-plane and in-plane components of polarization. Main twin boundary, side branches twin boundaries, and secondary side branches twin boundaries are identified by black, green, and blue lines, respectively (Fig. 5.17).

Micron-sized ferroelectric domains were easily switchable under external electric field and the average coercive voltage was found to be around 30 V. Figure 5.18a displays the

in-plane piezoresponse image after poling in bright and dark areas. Piezoresponse hysteresis loops also were obtained for the maximum *dc* voltage of 50V (Fig. 5.18). Hysteresis loop is a clear signature of polarization switching on the local scale.

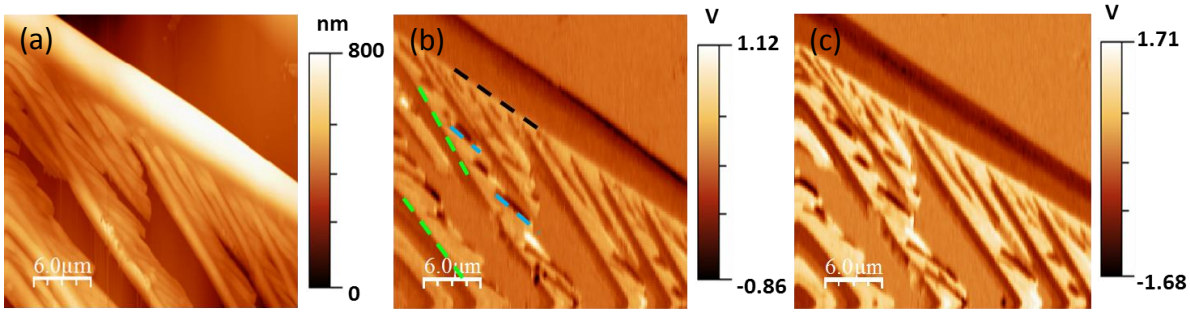

Figure 5.17. (a)-(c) show topography, the vertical and lateral PFM images of as grown dendritic shape β-glycine.

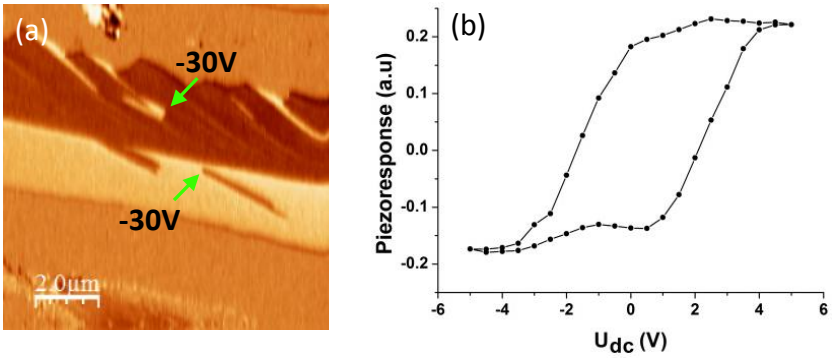

Figure 5.18. (a) Switching of ferroelectric domains with the application of *dc* voltage. (b) Hysteresis loop of the amplitude piezoresponse.

5.6. PFM in Thin Films of β-crystals

The significant ferroelectricity of the β-glycine crystal motivated us to process a thin film of glycine for easier miniaturization and integration, which we succeeded using the simple and inexpensive spin-coating approach. It is known that ferroelectric thin films may exhibit different properties from those of their bulk crystals [214] because surface/interface effect and dimensional effect commonly play an important role in polarization in thin ferroelectric films.

Figure 5.19 represents topography (a), PFM-lateral and vertical (b,c) measurements of the self-assembled glycine structures in the area between partially connected grains. According to the topography, glycine nanocrystals array in some parts of the film were uniform and closely packed and some parts were dispersed monolayer (Fig. 5.19a). Capillary forces between the particles of the similar size are more attractive relative to non-identical particles. Therefore, the areas of particles with uniform size are more closely packed arrangement relative to area with non-homogeneous particles.

PFM lateral image (Fig. 5.19b) shows a contrast only for a grain which polarization direction is perpendicular to the longest axis of the cantilever. In two other grains the contrast is weak because their polarization direction is parallel the cantilever axis and the contrast may arise only through the buckling effect. White arrows indicate the polarization orientation of each crystalline area (Fig. 5.19b). Vertical image (Fig. 5.19c) shows negligible contrast, in agreement with Raman measurements (ferroelectric axis *b* is oriented parallel to the substrate). The shear piezoelectric coefficient of the glycine film was derived between 12 and 17 pm/V which is twice as that for a β-glycine single crystal.

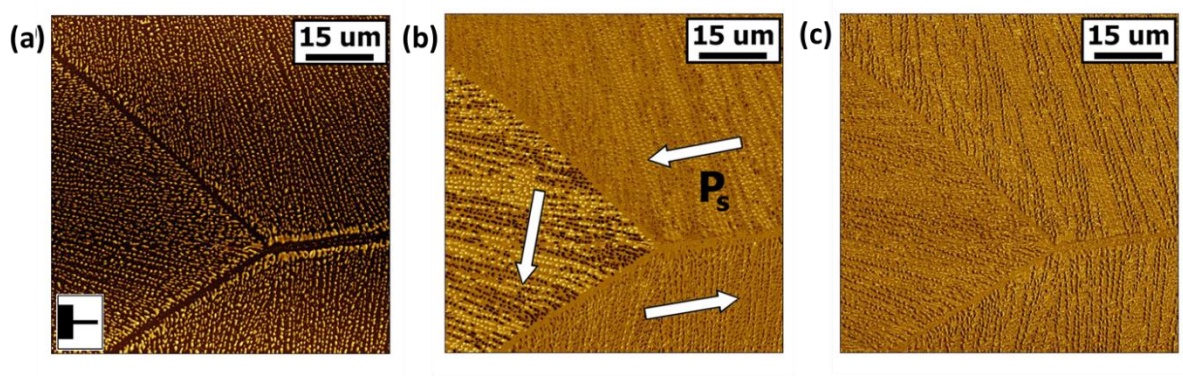

Figure 5.19. Representative images of topography (a), lateral (b) and vertical-PFM (c) measurements of the nanocrystalline glycine arrays on Pt substrate.

Higher magnification PFM of the particles in a non-closed packed area shows that these nanoislands have near spherical shape. While analyzing the domain structure of each microcrystal, it appears that they can be in the monodomain state or can be divided into two domains (Fig. 5.20a). The nanocrystals were easily switchable and the average coercive voltage was found to be around 20 V (Fig. 5.20b).

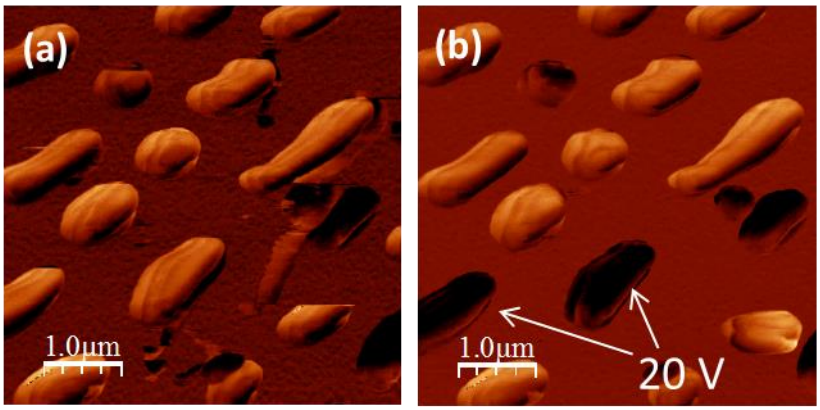

Figure 5.20. Switching of glycine islands: (a) PFM In-plane image of virgin film, (b) PFM image after switching of some islands under application of +20 V.

5.7. Optical Characterization of β-glycine Single Crystal

Ferroelectrics are also ideal materials for electro-optics and nonlinear optics applications (for polarization rotation and frequency conversion of light) [215], because the local direction of the polarization; hence, the properties of the material can be easily controlled through domain structure engineering.

Due to strongly polar nature and the presence of hydrogen bonds, glycine has been for a long time recognized as a potential nonlinear optical (NLO) material in which the useful optical properties (large nonlinear optical coefficient, large birefringence, wide transparency range, high damage threshold, broad spectral and temperature bandwidth, etc.) are combined with the ability of chemical modification using molecular engineering and intrinsic biocompatibility [216,217].

During the optical characterization, both linear and nonlinear methods were used. In the linear part, optical images of the grown crystals were acquired with parallel and crossed polarizer and analyzer positions. This procedure allowed finding the crystals where the high frequency dielectric permittivity looked anisotropic and the highest nonlinear susceptibility of β-glycine polymorph was therefore expected.

The nonlinear optical properties were obtained through the SHG measurements. Figure 5.21a,b represents the measured and fitted dependences of the SHG signal oriented parallel (P-out) and perpendicular (S-out) to the polarization of the incident light while rotating this polarization by 360°. In case of [010] crystallographic axes of β-glycine crystal

parallel to the incident light polarization direction, two different behaviors for P- and S-output polarization dependences were observed.

For P-output polarization, we observed two strong 180° peaks (Fig. 5.21a). We assume that these peaks are consistent with the strong dipole contribution of the $-COO^-$, $-NH_3^+$ molecule groups aligned along the [010] crystallographic axes (Fig. 5.12c). Therefore, we deduce that the inherent polarization of β-glycine lies along [010] crystallographic axes.

For the S-output polarization, we found four strong 180° peaks (Fig. 5.21b). We assume that these peaks contribute to the SHG signal owing to the zwitterions dipole precessions along the [100] crystallographic axes (Fig. 5.21d).

These results are in agreement with the Hyperchem 8 [207] simulations of the β-glycine molecules in the monoclinic crystal structure. The dipole moment of each molecule as well as the dipole moment of total crystal clusters was calculated using the unrestricted Hartree-Fock (UHF) PM3 method similarly to refs [218,219]. The polarization direction is determined from the $-COO^-$ group to the $-NH_3^+$ group in the zwitterionic form of each individual glycine molecule in polar layers which is nearly normal to the Pt substrate surface (Fig. 5.21c). The layers are linked together via hydrogen bonds in the [010] direction while forming a monoclinic structure. The total dipole moment is found to be parallel to the native fast-growth crystallographic direction (*b*-axis).

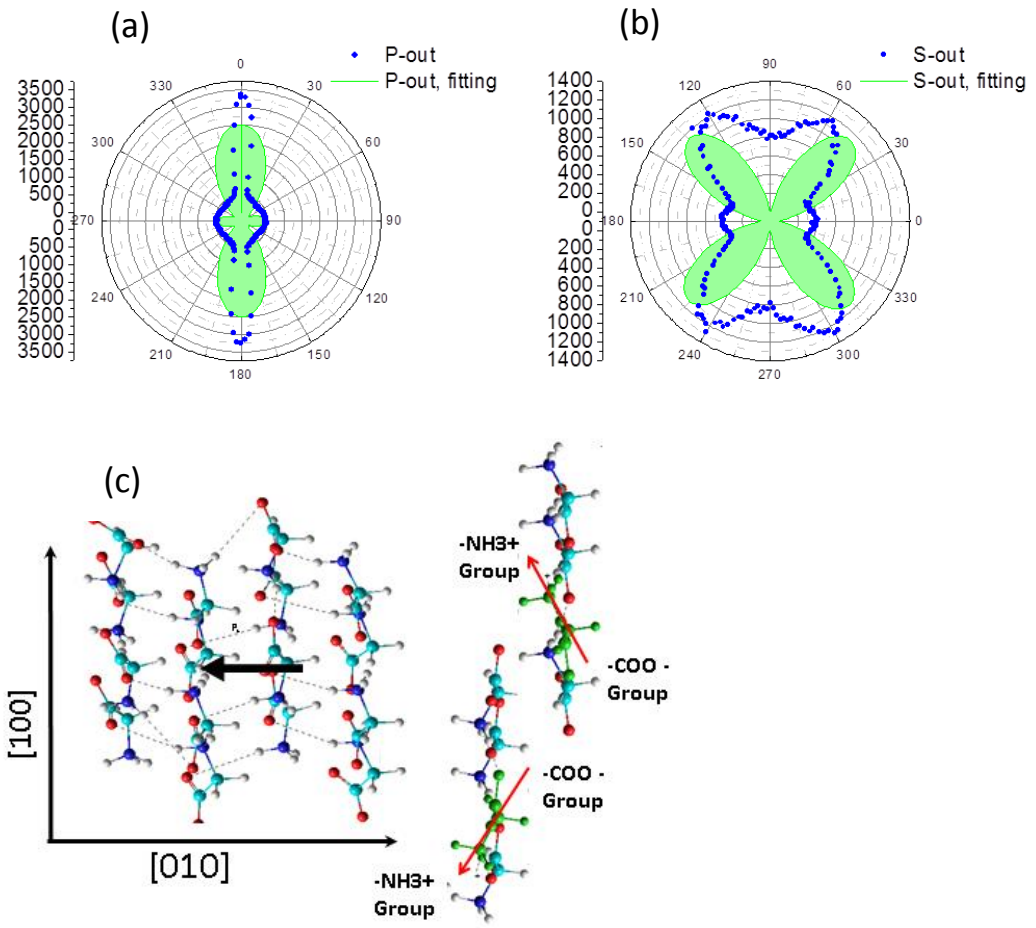

Figure 5.21. Measured and fitted light polarization dependences of the SHG signal from β-glycine for (a) P and (b) S output polarizations for crystallographic face (001). Molecular simulation of the (c) dipole moment of each glycine molecule as well as molecular cluster cut off from β-glycine crystal consisting of 4 layers and 16 molecules (160 atoms) with corresponding hydrogen bonds and (d) dipole moment of the $-NH_3^+$, $-COO^-$ groups of individual (marked by green color) glycine molecule in each layer.

In order to describe the obtained polarization dependences of $I^{2\omega}(\theta)$, equation 5.3 is rewritten for the point group C_2 and crystal face (001). This gives six independent tensor components: $\chi_1 = \chi_{123} = \chi_{132}$; $\chi_2 = \chi_{113} = \chi_{131} = \chi_{311}$; $\chi_3 = \chi_{322} = \chi_{223} = \chi_{232}$; $\chi_4 = \chi_{333}$; $\chi_5 = \chi_{312} = \chi_{321}$; $\chi_6 = \chi_{213} = \chi_{231}$ and SHG intensity as a function of polarization angle can be expressed as

$$I^{2\omega}(\theta) = C_0 + C_2 \cos 2\theta + C_4 \cos 4\theta + S_2 \sin 2\theta + S_4 \sin 4\theta, \quad (5.3)$$

where C_i and S_i denote the corresponding fitting parameters in the SHG polar dependences, which are the linear combinations of nonlinear susceptibility $\chi_{ijk}^{(2)}$ and Fresnel factors.

The results of the simultaneous fitting of two curves (P-out and S-out SHG polarization) are in a good agreement with the nonlinear experimental data (Fig. 5.21a,b, solid lines), showing the amplitude of neighbor molecule oscillation, the same number of petals and their orientation. These facts confirm our conclusion about the dipole contribution of the $-COO^-$, $-NH_3^+$ molecule groups aligned along the [010] crystallographic axes and the zwitterions dipole precessions along the [100] crystallographic axes. This gives the following values of nonlinear susceptibility tensor components: $\chi_1 = 0.36$ pm/V; $\chi_2 = 0.73$ pm/V; $\chi_3 = 0.16$ pm/V; $\chi_4 = 0.28$ pm/V; $\chi_5 = 0.89$ pm/V; $\chi_6 = 7.5 * 10^{-4}$ pm/V. The absolute values were obtained using a z-cut (001) quartz with its nonlinear susceptibility tensor components equal to $\chi_1 = 0.8$ pm/V, $\chi_2 = 0.017$ pm/V [220]. However, the experimental dependences possessed a noticeable background at their minimum (theoretical curves should vanish to zero at the same points). Such deviation may arise due to several reasons, for example, it can be a result of the presence of 90^o domains [221,222] or originate from the light scattering on optical inhomogeneities.

Thus, β-glycine crystals can be used to transform infrared and visible light into UV and near-UV radiation. Not only frequency conversion [223], but also amplitude and phase modulation can be used for optical communications and interconnections, optical switching data storage, and electro-optic applications [224]. The intrinsic biocompatibility expected in glycine could be helpful for bioimaging and photothermal therapy [225], where a light conversion to the UV is required for the generation of short lived toxic oxygen radicals. The possibility of obtaining ferroelectric patterns with any given configuration at moderate tip voltages (well below 100 V) in glycine crystal can be used to create regular microdomain patterns (by the vector lithography method) for providing tunable radiation [226,227]. Further work is needed to explore the potential of glycine for these applications.

(The SHG measurements have been performed in collaboration with Prof. Elena Mishina group from Moscow State Institute of Radioengineering, Electronics, and Automation, Moscow, Russia.)

5.8. Summary

Our findings suggest that γ-glycine is a piezoelectric crystal with a unique polar axis which cannot be switched by electric field (non ferroelectric). Contrarily, the presence of domain structure and switchability with the local application of an external electric field indicates the ferroelectric nature of β-glycine.

Our experiments have shown that micro-crystals of β-glycine are uniaxial ferroelectrics with polarization vector parallel to monoclinic axis *b*. The orientation of the polar axis of the crystal has been confirmed by X-ray diffraction analysis and Raman microscopy. The domain structure of β-glycine consists of charged and neutral 180^{o} domain walls. The domain shape is dictated by the polarization screening and mediated by growth defects such as atomic steps and pits. Dynamics of these in-plane domains is studied as a function of applied voltage and pulse duration. Thermodynamic theory is applied to explain the domain propagation induced by the PFM tip. Our findings suggest that the properties of β-glycine are controlled by the charged domain walls which in turn can be manipulated by the tip-enhanced electric field.

The conducted nonlinear optical measurements were consistent with the $P2_1$ symmetry of β-glycine with spontaneous polarization parallel to the monoclinic b-axis and zwitterions dipole precessions along the a-axis. The nonlinear optical susceptibility of β-glycine is found to about 50% greater than that of well-known nonlinear material *z*-cut (001) quartz. All results show that the glycine ferroelectric crystals have potential applications in ferroelectric and nonlinear optical devices. The reported results are explained by the idealized molecular models.

Piezoresponse Force Microscopy measurements confirmed that the films of nanocrystalline β-glycine exhibit superior piezoelectricity relative to bulk β-glycine crystals and lower coercive field required reversing the polarization.

Chapter 6

Conclusions and Future Work

6.1. Conclusions

The ability to grow stable glycine crystals has allowed us to study in detail the electromechanical and nonlinear optical properties in this technologically important material. We show that the smallest amino acid glycine possesses notable piezoelectric and ferroelectric properties. This underlines the significance of biopiezoelectric and bioferroelectric phenomena in living organisms (e.g., protein formation). Furthermore, this study could bring a variety of novel applications to glycine crystals as a biocompatible ferroelectric, which could be very useful for many new biomedical and nanoelectronic applications.

On the basis of the results the following main conclusions were made:

- Crystalline glycine can exist in three polymorphic forms (α, β, and γ) with different physical properties and it is possible to create selectively one of the polymorphs by controlling the solution type and crystallization conditions. α-glycine has a centrosymmetric structure (space group $P2_1/n$) and consequently cannot have piezoelectric property while the γ- and β-glycine possess non-centrosymmetric structure. Therefore, they were studied in more details in this thesis.

- β-glycine was found as a unstable crystal against ambient conditions, therefore, a new method of stabilization of the β-phase is demonstrated based on evaporation of aqueous solution on crystalline Pt(111) substrates. We found that the interplay between the concentration of the glycine solution and crystallization effect of the surface results in the preferential growth of glycine β-phase with well-defined shape and morphology. These two parameters are supposed to be the major factors dictating the evaporation rate and growth kinetics. As a result, β-glycine needle-shaped crystals could be grown under ambient conditions. X-ray diffraction analysis and Raman spectroscopy confirmed the preferential growth and stability of β-phase.

- The growth of stable β-glycine crystals has allowed us to study in details its domain structure geometry, switchability, and dynamics of the ferroelectric domain propagation by Piezoresponse Force Microscopy (PFM). The obtained PFM images on the non-polar crystal surface have shown as-grown structure consisted of domains

separated by neutral and charged domain walls (either head-to-head or tail-to-tail). Detailed study revealed topographic features at the as-grown charged domain boundaries; in contrast, the switched domains were not associated with surface defects. Domain polarization could be switched by applying a bias to non-polar cuts via a conducting tip of atomic force microscope (AFM). Thermodynamic theory is applied to explain the domain propagation under switching. Our findings suggest that the properties of β-glycine are controlled by the charged domain walls which in turn can be manipulated by an external bias.

- Based on the molecular modelling, we found that the network of hydrogen bonds plays an essential role in arrangement of glycine molecules in the crystal structures of glycine and dictates the difference in the properties of polymorphs. Computed data and obtained switching properties for both models of γ- and β-glycine polymorphic structures were compatible with the experimental observations in PFM experiments.

- The second harmonic generation (SHG) measurements confirmed that the 2-fold symmetry is preserved in as-grown β-crystals, thus reflecting the expected $P2_1$ symmetry of the β-phase. Spontaneous polarization direction is found to be parallel to the monoclinic [010] axis and directed along the crystal length. These data are confirmed by computational molecular modeling. Optical measurements revealed also relatively high values of the nonlinear optical susceptibility (50% greater than in the z-cut quartz).

- The thin films of glycine nanoscale crystals were produced by using the simple spin-coating approach. Ensemble of glycine nanocrystals was formed on the Pt substrate as a result of self-organized growth during spin-coating. The directions of nanocrystal axes on the substrate, piezoelectric and ferroelectric properties were studied.

- All the results show that the β-glycine is a promising functional molecular crystal as a candidate for piezoelectric, ferroelectric, and nonlinear optical applications.

6.2. Future Work

Obviously, further experiments and simulations are necessary for the full understanding of the role of glycine bioferroelectricity and biopiezoelectricity in the human body which is needed for future interdisciplinary research. Additionally, the development of bioorganic artificial materials with enhanced piezoelectric and ferroelectric properties is of high importance for future biologically compatible sensors, actuators, transducers, ferroelectric-based memories, frequency conversion devices and other electronic components. However, there are still important issues that need to be addressed to move towards device applications. Accordingly, the future work should be focused on the following issues:

- High resolution PFM study of the crystals in the liquid environment should be undertaken to reveal the nature of the structural defects and domain states.

- The glycine film properties and homogeneity can be improved using different techniques for the preparation and deposition such as spin coating at a high temperature or annealing the films after preparation. Higher process temperatures can give more uniform films owing to higher solvent evaporation rate. The effect of spinning speed and concentration of glycine solution on the film properties should be investigated as well.

- Furthermore, crystals of different amino acids (*e.g.* DL-alanine) should be grown and the entire set of the measurements should be done. This would expand the class of bioorganic ferroelectrics and reveal their role in the functioning of complex biological systems.

References

1. S. Horiuchi, R. Kumai and Y. Tokura, "Hydrogen-bonding molecular chains for high-temperature ferroelectricity", *Adv. Mater*. 23, 2098 (2011).

2. B. Coste, B. Xiao, J. S. Santos, R. Syeda, J. Grandl, K. S. Spencer, S. E. Kim, M. Schmidt, J. Mathur, A. E. Dubin, M. Montal, and A. Patapoutian, "Piezo proteins are pore-forming subunits of mechanically activated channels", *Nature* 483(7388), 176 (2012).

3. S. E. Kim, B. Coste, A. Chadha, B. Cook, and A. Patapoutian, "The role of Drosophila Piezo in mechanical nociception", *Nature* 483, 209 (2012).

4. V. S. Bystrov, I. Bdikin, A. Heredia, R. C. Pullar, E. Mishina, A. Sigov and A. L. Kholkin, "Piezoelectric nanomaterials for biomedical applications: piezoelectricity and ferroelectricity in biomaterials: from proteins to self-assembled peptide nanotubes", In "piezoelectric nanomaterials for biomedical applications", Eds. G. Ciofani and A. Menciassi, Berlin Heidelberg, Springer-Verlag. pp. 187-212 (2012)**.**

5. A. A. Marino and R. O. Becker, "Piezoelectric effect and growth control in bone", Nature 228, 473 (1970).

6. I. Tasaki, "Evidence for phase transition in nerve fibres, cells and synapses", *Ferroelectrics* 220, 305 (1999).

7. J. Y. Li, Y. M. Liu, Y. H. Zhang, H. L. Cai and R. G. Xiong, "Molecular ferroelectrics: where electronics meet biology", *Phys. Chem. Chem. Phys*. 15, 20786 (2013).

8. T. Hidaka, T. Maruyama, M. Saitoh, N. Mikoshiba, M. Shimizu, T. Shiosaki, L. A. Wills, R. Hiskes, S.A. DiCarolis and J. Amano, "Formation and observation of 50 nm polarized domains in $PbZr_{1-x}\ Ti_x\ O_3$ thin film using scanning probe microscope", *Appl. Phys. Lett*. 68, 2358 (1996).

9. A. Gruverman, D. Wu, B. J. Rodriguez, S. V. Kalinin and S. Habelitz, "High-resolution imaging of proteins in human teeth by scanning probe microscopy", *Biochem. Biophys. Res. Commun*. 352, 142 (2007).

10. S. V. Kalinin, S. Jesse, B. J. Rodriguez, K. Seal, A. P. Baddorf, T. Zhao, Y. H. Chu, R. Ramesh, E. A. Eliseev, A. N. Morozovska, B. Mirman, and E. Karapetian, "Recent advances in electromechanical imaging on the nanometer scale: polarization dynamics in ferroelectrics biopolymers, and liquid imaging", *Jpn. J. Appl. Phys*. 46, 5674 (2007).

11. S. V. Kalinin, B. J. Rodriguez, J. Shin, S. Jesse, V. Grichko, T. Thundat, A. P. Baddorf, and A. Gruverman, "Bioelectromechanical imaging by scanning probe microscopy: Galvani's experiment at the nanoscale", *Ultramicroscopy* 106, 334 (2006).

12. S. V. Kalinin, B. J. Rodriguez, S. Jesse, E. Karapetian, B. Mirman, E. A. Eliseev and A. N. Morozovska, "Nanoscale Electromechanics of Ferroelectric and Biological Systems: A New Dimension in Scanning Probe Microscopy", *Annu. Rev. Mater. Res.* 37, 189 (2007).

13 V. V. Lemanov, “Piezoelectric and pyroelectric properties of protein amino acids as basic materials of Soft State Physics”, *Ferroelectrics* 238, 211 (2000).

14. V.V. Lemanov, S. N. Popov and G. A. Pankova, “Protein Amino Acid Crystals: Structure, symmetry, physical properties”, *Ferroelectrics* 285, 207 (2003).

15. A. Heredia, V, Meunier, I. K. Bdikin, J, Gracio, N, balke, S, Jesse, A, Tselev, P. K. Agarwal, B. G. Sumpter, S. V. Kalinin and A. L. Kholkin, “Nanoscale ferroelectricity in crystalline γ-glycine”, *Adv. Funct. Mater*. 22, 2996 (2012).

16. A. L. Lehninger, “Biochemistry: The molecular basis of cell structure and function”, Worth Publishers, Inc., New York (1972).

17. G. Albrecht and R. B. Corey, “The crystal structure of glycine”, *J. Am. Chem. Soc*. 61(5), 1087 (1939).

18. Y. Iitaka, “The crystal structure of γ-glycine”, *Acta Cryst*. 14, 1 (1961).

19. Y. Iitaka, “The crystal structure of β-glycine”, *Acta Cryst*. 13, 35 (1960).

20. S. A. Azhagan and S. Ganesan, “Structural, mechanical, optical and second harmonic generation (SHG) studies of gamma glycine single crystal”, *S. Int. J. Phys. Sci*. 8, 6 (2013).

21. D. Isakov, E. M. Gomes, I. Bdikin, B. Almeida, M. Belsley, M. Costa, V. Rodrigues and A. Heredia, “Production of Polar β-Glycine Nanofibers with Enhanced Nonlinear Optical and Piezoelectric Properties”, *Cryst. Growth Des*. 11, 4288 (2011).

22. A. L. Kholkin, N. A. Pertsev and A. V. Goltsev, “Piezoelectricity and crystal symmetry”, In “piezoelectric and acoustic materials for transducer applications”, Eds. A. Safari, K. Akdogan, Springer, pp. 17-38 (2008).

23. J. F. Nye, “Physical properties of crystals: their representation by tensors and matrices”, Oxford University Press, New York, (1957).

24. L. L. Hench and J. K. West, “Principles of electronic ceramics”, Wiley, New York (1990).

25. N. Setter and E. L. Colla, “Ferroelectric ceramics”, Birkhauser Verlag, Basel (1993).

26. R. W. Whatmore, S. B. Stringfellow and N. M. Shorrocks, “Ferroelectric materials for uncooled thermal imaging”, *Proc. SPIE*, 2020, 39 (1993).

27. M. E. Lines and A. M. Glass, “Principles and Applications of Ferroelectrics and Related Materials”, Clarendon press, Oxford (1977).

28. K. M. Rabe, C. H. Ahn and J. M. Triscone, “Physics of Ferroelectrics: A Modern Perspective”, Springer-Verlag, Berlin Heidelberg (2007).

29. D. Damjanovic, “Hysteresis in piezoelectric and ferroelectric materials”, In “the science of hysteresis”, Eds. I. Mayergoyz and G. Bertotti, Elsevier, pp. 337-465 (2005).

30. J. F. Scott, “Applications of modern ferroelectrics”, *Science* 315, 954 (2007).

31. V. R. Palkar, S. C. Purandare and R. Pinto, "Ferroelectric thin films of $PbTiO_3$ on silicon", *J. Phys.* D, 32, 1 (1999).

32. M. Veithen, X. Gonze and P. Ghosez, "First-principles study of the electro-optic effect in ferroelectric oxides", *Phys. Rev. Lett*. 93, 187401 (2004).

33. V. Gopalan, M. J. Kawas, T. E. Schlesinger, M. C. Gupta, and D. D. Stancil, "Integrated quasi-phase-matched second-harmonic generator and electrooptic scanner on $LiTaO_3$ single crystals", *IEEE Photonics Technol. Lett*. 8, 1704 (1996).

34. V. V. Lemanov and Yu. V. Llisavsky, "Piezoelectricity and acoustoelectronics", *Ferroelectrics* 42, 77 (1982).

35. J. F. Scott, "Ferroelectric memories", Springer-Verlag, Berlin (2000).

36. R. E. Jones, Jr., P. D. Maniar, R. Moazzami, P. Zurcher, J. Z. Witowski, Y. T. Lii, P. Chu, and S. J. Gillespie, "Ferroelectric non-volatile memories for low-voltage, low-power applications", *Thin Solid Films* 270, 584 (1995).

37. J. Valasek, "Piezo-electric and allied phenomena in Rochelle salt", *Phys. Rev*. 17, 475 (1921).

38. H. D. Megaw, "Crystal structure of barium titanate", *Nature* 155, 484 (1945).

39. B. Jaffe, R. S. Roth and S. Marzullo, "Piezoelectric properties of lead zirconate-lead titanate solid-solution ceramics", *J. Appl. Phys*. 25, 809 (1954).

40. S. Hoshino, T. Mitsui, F. Jona and R. Pepinsky, "Dielectric and thermal study of tri-glycine sulfate and tri-glycine fluoberyllate", *Phys. Rev*. 107**,** 1255 (1957)

41. S. Horiuchi, Y. Tokunaga, G. Giovannetti, S. Picozzi, H. Itoh, R. Shimano, R. Kumai and Y. Tokura, "Above-room-temperature ferroelectricity in a single-component molecular crystal", *Nature* 463, 789 (2010).

42. D. W. Fu, W. Zhang, H. L.Cai, J. Z. Ge, Y. Zhang and R. G. Xiong, "Diisopropylammonium chloride: a ferroelectric organic salt with a high phase transition temperature and practical utilization level of spontaneous polarization", *Adv. Mater*. 23, 5658 (2011).

43. D. W. Fu, H. L. Cai, Y. Liu, Q. Ye, W. Zhang, Y. Zhang, X. Y. Chen, G. Giovannetti, M. Capone, J. Li and R. G. Xiong, "Diisopropylammonium bromide is a high-temperature molecular ferroelectric crystal", *Science*, 339, 425 (2013).

44. A. K. Tagantsev, L. E. Cross and J. Fousek, "Domains in ferroic crystals and thin films", Springer, New York (2010).

45. X. Wu and D. Vanderbilt, "Theory of hypothetical ferroelectric superlattices incorporating head-to-head and tail-to-tail 180° domain walls", *Phys. Rev. B* 73, 020103 (2006).

46. E. G. Fesenko, V. G. Gavrilyachenko, M. A. Martinenko, A. F. Semenchov and I. P. Lapin, "Domain structure peculiarities of lead-titanate crystals", *Ferroelectrics* 6, 61 (1973).

47. C. L. Jea, S. B. Mi, K. Urban, I. Vrejoiu, M. Alexe, and D. Hesse, "Atomic-scale study of electric dipoles near charged and uncharged domain walls in ferroelectric films", *Nature Materials* 7, 57 (2008).

48. F. Kagawa, S. Horiuchi, N. Minami, S. Ishibashi, K. Kobayashi, R. Kumai, Y. Murakami and Y. Tokura, "Polarization switching ability dependent on multidomain topology in a uniaxial organic ferroelectric", *Nano Letters* 14 (1), 239 (2014).

49. M. Y. Gureev, A. K. Tagantsev and N. Setter, "Head-to-head and tail-to-tail 180◦ domain walls in an isolated ferroelectric", *Phys. Rev. B* 83, 184104 (2011).

50. E. Fukada and I. Yasuda, "On the piezoelectric effect of bone", *J. Phys. Soc. Jpn.* 12, 1158 (1957).

51. E. Fukada and I. Yasuda, "Piezoelectric effects in collagen", *J. Appl. Phys*. 3, 117 (1964).

52. H. Athenstaedt, "Pyroelectric and piezoelectric behaviour of human dental hard tissues", *Arch. Oral Biol*. 16, 495 (1971).

53. R. M. Zilberstein, "Piezoelectric activity in invertebrate exoskeletons", Nature, 235, 174. (1972).

54. S. B. Lang, A. A. Marino, G. Berkovic, M. Fowler and K. D. Abreo, "Piezoelectricity in the human pineal gland", *Bioelectrochem. Bioenerg*. 41, 191 (1996).

55. S. B. Lang, "Piezoelectricity, pyroelectricity and ferroelectricity in biomaterials: Speculation on their biological significance", *IEEE Trans. Dielectr. Electr. Insul*. 7, 466 (2000).

56. I. Ermolina, A. Strinkovski, A. Lewis and Y. Feldman, "Observation of liquid-crystal-like ferroelectric behavior in a biological membrane", *J. Phys. Chem. B*, 105, 2673 (2001).

57. A. C. Jayasuriya, J. I. Scheinbeim, V. Lubkin, G. Bennett and P. Kramer, "Piezoelectric and mechanical properties in bovine cornea", *J. Biomed Mater. Res.* A 66, 260 (2003).

58. S. B. Lang, "Pyroelectric effect in bone and tendon", *Nature* 212, 704 (1966).

59. S. B. Lang, "Pyroelectricity: Occurrence in biological materials and possible physiological implications", *Ferroelectrics* 34, 3 (1981).

60. H. Athenstaedt, H. Claussen and D. Schaper, "Epidermis of human skin: Pyroelectric and piezoelectric sensor layer", *Science*. 216, 1018 (1982).

61. H. R. Leuchtag, "Fit of the dielectric anomaly of squid axon membrane near heatblock temperature to the ferroelectric Curie-Weiss law", *Biophys. Chem*. 53, 197 (1995).

62. H. R. Leuchtag and V. S. Bystrov, "Ferroelectric and related models in biological systems", *Ferroelectrics* 220, 157 (1999).

63. Y. Palti and W. J. Adelman Jr, "Measurement of axonal membrane conductances and capacity by means of a varying potential control voltage clamp", *J. Memb. Biol.* 1, 431 (1969).

64. V. S. Bystrov and N. K. Bystrova, "Bioferroelectricity and optical properties of biological systems", *Proc. SPIE* 5122, 135 (2003).

65. C. Halperin, S. Mutchnik, A. Agronin, M. Molotskii, P. Urenski, M. Salai and G. Rosenman, "Piezoelectric effect in human bones studied in nanometer scale", *Nano Lett.* 4, 1253 (2004).

66. S. V. Kalinin, B. J. Rodriguez, S. Jesse, T. Thundat and A. Gruverman, "Electromechanical imaging of biological systems with sub-10 nm resolution", *Appl. Phys. Lett.*, 87, 053901 (2005).

67. B. J. Rodriguez, S. V. Kalinin, J. Shin, S. Jesse, V. Grichko, T. Thundat, A. P. Baddorf and A. Gruverman, "Electromechanical imaging of biomaterials by scanning probe microscopy", *J. Struct. Biol*. 153, 151 (2006).

68. M. Minary-Jolandan and M. F. Yu, "Nanoscale characterization of isolated individual type I collagen fibrils: polarization and piezoelectricity", *Nanotechnology*, 20, 085706 (2009).

69. C. Harnagea, M. Vallieres, C. P. Pfeffer, D. Wu, B. R. Olsen, A. Pignolet, F. Legare and A. Gruverman, "Two-dimensional nanoscale structural and functional imaging in individual collagen type I fibrils", *Biophys. J*. 98, 3070 (2010).

70. M. Pal, R. Guo and A. Bhalla, "Biological ferroelectricity in human nail samples using piezoresponse force microscopy", *Materials Research Innovations* 17, 442 (2013).

71. A. L. Kholkin, N. Amdursky, I. Bdikin, E. Gazit and G. Rosenman, "Strong piezoelectricity in bioinspired peptide nanotubes", *ACS Nano* 4, 610 (2010).

72. N. Amdursky, P. Beker, J. Schklovsky, E. Gazit and G. Rosenman, "Ferroelectric and related phenomena in biological and bioinspired nanostructures", *Ferroelectrics* 399 (1), 16, 107 (2010).

73. T. Li and K. Zeng, "Piezoelectric properties and surface potential of green abalone shell studied by scanning probe microscopy techniques", *Acta Mater*. 59, 3667 (2011).

74. T. Li, L. Chen and K. Y. Zeng, "In situ studies of nanoscale electromechanical behavior of nacre under flexural stresses using band excitation PFM", *Acta Biomaterialia*, 9, 5903 (2013).

75. T. Li and K. Zeng, "Nanoscale piezoelectric and ferroelectric behaviors of seashell by piezoresponse force microscopy," *J. Appl. Phys*. 113, 187202 (2013).

76. Y. Liu, Y. Zhang, M. J. Chow, Q. N. Chen and J. Li, "Biological ferroelectricity uncovered in aortic walls by piezoresponse force microscopy", *Phys. Rev. Lett*., 108, 078103 (2012).

77. Y. Liu, Y. Wang, M. Chow, N. Q. Chen, F. Ma, Y. Zhang and J. Li, "Glucose suppresses biological ferroelectricity in aortic elastin", *Phys. Rev. Lett*., 110, 168101 (2013).

78. A. Heredia, M. Machado, I. K. Bdikin, J. Gracio, S. Yudin, V. M. Fridkin, I. Delgadillo, and A. L. Kholkin, "Preferred deposition of phospholipids onto ferroelectric P(VDF-TrFE) films via polarization patterning", *J. Phys. D* 43, 335301 (2010).

79. S. Horiuchi and Y. Tokura, "Organic ferroelectrics," *Nat. Mater*. 7, 357, (2008).

80. H. L. Cai, W. Zhang, J. Z. Ge, Y. Zhang, K. Awaga, T. Nakamura and R. G. Xiong, "4-(cyanomethyl) anilinium perchlorate: a new displacive-type molecular ferroelectric", *Phys. Rev. Lett.* 107, 147601 (2011).

81. W. J. Hu, D-M. Juo, L. You, J. Wang, Y.-C. Chen, Y.-H. Chu and T. Wu, "Universal ferroelectric switching dynamics of vinylidene fluoride-trifluoroethylene copolymer films", *Scientific Reports*, 4, 4772 (2014).

82. G. J. Goldsmith and J. G. J. White, "Ferroelectric behavior of thiourea". *Chem. Phys*. 31, 1175, (1959).

83. K. Noda, K. Ishida, *A.* Kubono, T. Horiuchi, H. Yamada and K. Matsushige, "Remanent polarization of evaporated films of vinylidene fluoride oligomers", *J.* Appl. Phys. 93, 2866 (2003).

84. S. Chen and X. Cheng Zeng, "Design of ferroelectric organic molecular crystals with ultrahigh polarization", *J. Am. Chem. Soc*. 136, 6428 (2014).

85. K. Kobayashi, S. Horiuchi, R. Kumai, F. Kagawa, Y. Murakami and Y. Tokura, "Electronic ferroelectricity in a molecular crystal with large polarization directing antiparallel to ionic displacement", *Phys. Rev. Lett*, 108, 237601 (2012).

86. T. Hasegawa and Y. Tokura, "Molecular donor-acceptor compounds as prospective organic electronics materials", *J. Phys. Soc. Jpn*. 75, 051016 (2006).

87. S. Horiuchi, R. Kumai and Y. Tokura, "Room-temperature ferroelectricity and gigantic dielectric susceptibility on a supramolecular architecture of phenazine and deuterated chloranilic acid", *J. Am. Chem. Soc*. 127, 5010 (2005).

88. S. Horiuchi, F. Ishii, R. Kumai, Y. Okimoto, H. Tachibana, N. Nagaosa and Y. Tokura, "Ferroelectricity near room temperature in co-crystals of nonpolar organic molecules", *Nat. Mater*. 4, 163 (2005).

89. S. Horiuchi, R. Kumai and Y, Tokura, "Proton-displacive ferroelectricity in neutral cocrystals of anilic acids with phenazine", *J. Mater. Chem*. 19, 4421 (2009).

90. S. Koval, J. Kohanoff, J. Lasave, G. Colizzi and R. L. Migoni, "First-principles study of ferroelectricity and isotope effects in H-bonded KH_2PO_4 crystals", *Phys. Rev. B* 71, 184102 (2005).

91. S. Horiuchi, R. Kumai and Y. Tokura, "A supramolecular ferroelectric realized by collective proton transfer", *Angew. Chem. Int. Ed.* 46, 3497 (2007).

92. S. Horiuchi, F. Kagawa, K. Hatahara, K. Kobayashi, R. Kumai, Y. Murakami and Y. Tokura, "Above-room-temperature ferroelectricity and antiferroelectricity in benzimidazoles", *Nature Commun*. 3, 1308 (2012).

93. A. S. Tayi, A. K. Shveyd, A. C. Sue, J. M. Szarko, B. S. Rolczynski, D. Cao, T. J. Kennedy, A. A. Sarjeant, C. L. Stern, W. F. Paxton, W. Wu, S. K. Dey, A. C. Fahrenbach, J. R Guest, H. Mohseni, L. X. Chen, K. L. Wang, J. F. Stoddart and S. I. Stupp, "Room-temperature ferroelectricity in supramolecular networks of charge-transfer complexes", *Nature* 488, 485 (2012).

94. M. Yamada, M. Saitoh, and H. Ooki, "Electric-field induced cylindrical lens, switching and deflection devices composed of the inverted domains in $LiNbO_3$ crystals", *Appl. Phys. Lett*. 69, 3659 (1996).

95. A. Feisst and P. Koidl, "Current induced periodic ferroelectric domain structures in $LiNbO_3$ applied for efficient nonlinear optical frequency mixing", *Appl. Phys. Lett*. 47, 1125 (1985).

96. P. A. Franken, A. E. Hill, C. W. Peters and G. Weinreich, "Generation of optical harmonics", *Phys. Rev. Lett*. 7, 118 (1961).

97. A. M. Prokhorov and Y. S. Kuzminov, "Physics and Chemistry of Crystalline Lithium Niobate", Adam Hilger, Bristol (1990).

98. R. C. Miller, D. A. Kleinman and A. Savage "Quantitative studies of optical harmonic generation in CdS, $BaTiO_3$, and KH_2PO_4 type crystals", *Phys. Rev. Lett*. 11, 146 (1963).

99. J. Zyss, "Molecular Nonlinear Optics: Materials, Physics, Devices", Academic Press, New York (1994).

100. M. A. Khan, U. S. Bhansali and H. N. Alshareef, "High-performance non-volatile organic ferroelectric memory on banknotes", *Adv. Mater*. 24, 2165 (2012).

101. K. Asadi, M. Y. Li, P. W. M. Blom, M. Kemerink and D. M. de Leeuw, "Organic ferroelectric opto-electronic memories", *Mater. Today*, 14, 592 (2011).

102. K. Takashima, S. Horie, T. Mukai, K. Ishida and K.Matsushige, "Piezoelectric properties of vinylidene fluoride oligomer for use in medical tactile sensor applications", *Sens. Actuators, A* 144, 90 (2008).

103. S. Horie, K. Noda, H. Yamada, K. Matsushige, K. Ishida and S. Kuwajima, "Flexible programmable logic gate using organic ferroelectric multilayer", *Appl. Phys. Lett*. 91, 193506 (2007).

104. M. Lee, C. Y. Chen, S. Wang, S. N. Cha, Y. J. Park, J. M. Kim, L. J. Chou and Z. L. Wang, "A hybrid piezoelectric structure for wearable nanogenerators", *Adv. Mater*. 24, 1759 (2012).

105. C. L. Sun, J. Shi, D. J. Bayerl and X. D. Wang, "PVDF microbelts for harvesting energy from respiration", *Energy Environ. Sci*. 4, 4508 (2011).

106. D.V. Isakov, E. de Matos Gomes, B. Almeida, A. L. Kholkin, P. Zelenovskiy, M. Neradovskiy and V. Ya. Shur, "Energy harvesting from nanofibers of hybrid organic ferroelectric dabcoHReO_4" *Appl. Phys. Lett.* 104, 032907 (2014).

107. V. S. Bystrov, E. Seyedhosseini, S. Kopyl, I. K. Bdikin and A. L. Kholkin, "Piezoelectricity and ferroelectricity in biomaterials: molecular modeling and piezoresponse force microscopy measurements", *J. Appl. Phys.* 116, 066803 (2014)

108. E. Boldyreva, "Crystalline Amino Acids - A Link between Chemistry, Materials Science and Biology", In "Models, Mysteries and Magic of Molecules", Eds. J. C. A. Boeyens, J. F. Ogilvie, Springer, New York (2008).

109. J. Bernstein, "Polymorphism in molecular crystals", Oxford University Press, New York (2002).

110. V. V. Lemanov, S. N. Popov and G. A. Pankova, "Piezoelectric properties of crystals of some protein aminoacids and their related compounds", *Phys. Solid State*. 44, 1929 (2002).

111. V. V. Lemanov, S. N. Popov and G. A. Pankova, "Piezoelectricity in protein amino acids, *Physics of the Solid State* 53, 1191 (2011).

112. J. W. Mullin, "Crystallization", Butterworth-Heinemann, 4th edn., Oxford (2001).

113. J. D. Yoreo and P. G. Vekilov, "Principles of crystal nucleation and growth", *Rev. Mineral. Geochem*. 54, 57 (2003).

114. I. Weissbuch, M. Lahav and L. Leiserowitz, "Toward stereochemical control, monitoring, and understanding of crystal nucleation", *Cryst. Growth Des*. 3, 125 (2003).

115. A. Holden and P. Singer, “Crystals and Crystal Growing”, Anchor Books-Doubleday, New York (1960).

116. H. M. Gorr, J. M. Zueger, D. R. McAdams and J. A. Barnard, “Salt-induced pattern formation in evaporating droplets of lysozyme solutions”, *Colloids Surf. B* 103, 59 (2013).

117. C. Suresh and M. Vijayan, “Head-to-tail sequences and other patterns of peptide aggregation in the solid state”, *Int. J. Pept. Protein Res*. 26, 311 (1985).

118. J. E. Elsila, J. P. Dworkin, M. P. Bernstein and S. A. Sandford, “Mechanism of amino acid formation in interstellar ice analogs”, *Astrophys. J*. 660, 911 (2007).

119. J. A. Chisholm, S. Motherwell, P. R. Tulip, S. Parsons and S. J. Clark, “An ab initio study of observed and hypothetical polymorphs of glycine”, *Cryst. Growth. Des*. 5, 1437 (2005).

120. E. V. Boldyreva, V. A, Drebushchak, T. N. Drebushchak, I. E. Paukov, Y. A. Kovalevskaya and E. S. Shutova, “Polymorphism of glycine: thermodynamic aspects. Part I. relative stability of the polymorphs”, *J. Therm. Anal. Calorim*. 73 (2), 409 (2003).

121. S. V. Goryainov, E. V. Boldyreva and E. N. Kolesnik, “Raman observation of a new (ζ) polymorph of glycine?”, *Chem. Phys. Lett*. 419, 496 (2006).

122. V. A. Drebushshak, E. V. Boldyreva, T. N. Drebushchak and E. S. Shutova, “Synthesis and calorimetric investigation of unstable *β*-glycine”, *J. Cryst. Growth*, 241, 266 (2002).

123. G. L. Pervolich, L. K. Hansen and A. Bauer-Brandl, “The polymorphism of glycine. thermochemical and structural aspects”, *J. Therm. Anal. Calorim*. 66, 699 (2001).

124. E. S. Ferrari, R. J. Davey, W. I. Cross, A. L. Gillon and C. S. Towler, “Crystallization in polymorphic systems: the solution-mediated transformation of β to α glycine”, *Cryst. Growth Des*. 3, 53 (2003).

125. A. L. Markel, A. F. Achkasov, T. A. Alekhina, O. I. Prokudina, M. A. Ryazanova, T. N. Ukolova, V. M. Efimov, E. V. Boldyreva and V. V. Boldyrev, “Effects of the alpha- and gamma-polymorphs of glycine on the behavior of catalepsy prone rats”, *Pharmacology, Biochemistry and Behavior*, 98, 234 (2011).

126. R. E. Marsh, “A refinement of the crystal structure of glycine”, *Acta. Cryst*., 11, 654 (1958).

127. D. Gidalevitz, R. Feidenhans’l, S. Matlis, D. M. Smilgies, M. J. Christensen, L. Leiserowitz, “Monitoring in situ growth and dissolution of molecular crystals: towards determination of the growth units”, Angew. *Chem. Int. Ed. Engl*. 36, 955 (1997).

128. J. D. Bernal, “The crystal structure of the natural amino acids and related compounds”, *Z*. Kristallogr, 78, 363 (1931).

129. K. Srinivasan, “Crystal growth of α and γ glycine polymorphs and their polymorphic phase transformations”, *J. Cryst. Growth*, 311, 156 (2008).

130. C. J. Ksanda and G. Tunell, “The unit cell and space-group of β-glycine”, *Am. J. Sci*. A 35, 173 (1938).

131. V. A. Drebushchak, E. V. Boldyreva, T. N. Drebushchak and E. S. Shutova, "Synthesis and calorimetric investigation of unstable *β*-glycine", *J. Cryst. Growth*, 241, 266 (2002).

132. A. Sander, T. Penović and J. Šipušić, "Crystallization of β-glycine by spray drying", *Cryst. Res. Technol*. 46, 145 (2011).

133. N. V. Surovtsev, S. V. Adichtchev, V. K. Malinovsky, A. G. Ogienko, V. A. Drebushchak, A. Yu. Manakov, A. I. Ancharov, A. S. Yunoshev and E. V. Boldyreva, "Glycine phases formed from frozen aqueous solutions: revisited", *J. Chem. Phys*. 137, 65103 (2012).

134. A. Pyne and R. Suryanarayanan, "Phase transitions of glycine in frozen aqueous solutions and during freeze-drying", *Pharm. Res*. 18, 1448, (2001).

135. B. D. Hamilton, M. A, Hillmyer and M. D. Ward, "Glycine polymorphism in nanoscale crystallization chambers", *Cryst. Growth Des*. 8, 3368 (2008).

136. A. Y. Lee, I. S. Lee and A. S. Myerson, "Factors affecting the polymorphic outcome of glycine crystals constrained on patterned substrate" *Chem. Eng. Technol*. 29, 281 (2006).

137. I. S. Lee, K. T. Kim, R. A. Y. Lee and A. S. Myerson, "Concomitant Crystallization of Glycine on Patterned Substrates: The Effect of pH on the Polymorphic Outcome", *Cryst. Growth Des*. 8, 108 (2008).

138. M. N. Bhatt and S. M. Dharmaprakash, "Growth of nonlinear optical γ-glycine crystals", *J. Cryst. Growth*, 236, 376 (2002).

139. M. N. Bhatt and S. M. Dharmaprakash, "Effect of solvents on the growth morphology and physical characteristics of nonlinear optical γ-glycine crystals", *J. Cryst. Growth*, 242, 245 (2002).

140. K. Srinivasan and J. Arumugam, "Growth of non-linear optical γ-glycine single crystals and their characterization", *J. Opt. Mater*. 30, 40 (2007).

141. I. Weissbuch, L. Leiserowitz and M. Lahav, "Tailor-made and charge-transfer auxiliaries for the control of the crystal polymorphism of glycine", *Adv. Mater*. 6, 952 (1994).

142. J. E. Aber, S. Arnold, B. A. Garetz and A. S. Myerson, "Strong dc electric field applied to supersaturated aqueous glycine solution induces nucleation of γ-polymorph" *Phys. Rev. Lett*. 94, 145503 (2005).

143. J. Zaccaro, J. Matic, A. S. Myerson and B. A. Garetz, "Nonphotochemical, laser-induced nucleation of supersaturated aqueous glycine produces unexpected γ-polymorph", *Cryst. Growth Des*. 1, 5 (2001).

144. B. A. Garetz, J. Matic and A. S. Myerson, "Polarization switching of crystal structure in the nonphotochemical light-induced nucleation of supersaturated aqueous glycine solutions", *Phys. Rev. Lett*. 89, 175501 (2002).

145. G. He, V. Bhamidi, S. R. Wilson, R. B. H. Tan, P. J. A. Kenis and C. F. Zukoski, "Direct Growth of γ-Glycine from Neutral Aqueous Solutions by Slow, Evaporation-Driven Crystallization", *Cryst. Growth Des*. 6, 1746 (2006).

146. I. Gregora, Raman scattering. In "International Tables for Crystallography, Vol. D: Physical properties of crystals", Ed. A. Authier, Kluwer Academic Publishers, Norwell (2003).

147. L. E. O'Brien, P. Tammins, A. C. Williams and P. York, "Use of in situ Ft-raman spectroscopy to study the kinetics of the transformation of carbamazepine polymorphs", *J. Pharm. Biomed. Anal*. 36, 335 (2004).

148. A. Gruverman, O. Auciello and H. Tokumoto, "Imaging and control of domain structures in ferroelectric thin films via scanning force microscopy", *Annu. Rev. Mater. Sci*. 28, 101 (1998).

149. S. V. Kalinin, A. N. Morozovska, L. Q. Chen and B. J. Rodriguez, "Local polarization dynamics in ferroelectric materials, *Rep. Prog. Phys*. 73, 056502 (2010).

150. A. Kholkin, "Introduction, principles and instrumental aspects of piezoresponse force microscopy by NT-MDT", Sept 13 (2010).

151. R. Proksch and S. V. Kalinin, "Piezoresponse Force Microscopy with Asylum Research AFMs" In: Asylum Research Application Note 10.

152. E. Soergel, "Piezoresponse Force Microscopy (PFM)", *J. Phys. D: Appl. Phys*. 44, 464003 (2011).

153. S. V. Kalinin, B. J. Rodriguez, S. Jesse, J. Shin, A. P. Baddorf, P. Gupta, H. Jain, D. B. Williams and A. Gruverman, "Vector piezoresponse force microscopy", *Microsc. Microanal.* 12, 206 (2006).

154. S. Jesse, A. P. Baddorf, and S. V. Kalinin, "Switching spectroscopy piezoresponse force microscopy of ferroelectric materials", *Appl. Phys. Lett*. 88, 062908 (2006).

155. A. L. Kholkin, S. V. Kalinin, A. Roelofs, and A. Gruverman, "Review of ferroelectric domain imaging by piezoresponse force microscopy, in scanning probe microscopy: electrical and electromechanical phenomena at the nanoscale", Springer, NY, 173 (2007).

156. A. Gruverman and A. L. Kholkin, "Nanoscale ferroelectrics: processing, characterization and future trends", *Rep. Prog. Phys*. 69, 2443 (2006).

157. P. Sharma, D. Wu, S. Poddar, T. J. Reece, S. Ducharme and A. Gruverman, "Orientational imaging in polar polymers by piezoresponse force microscopy", *J. Appl. Phys*. 110, 52010 (2011).

158. N. Balke, I. Bdikin, S. V. Kalinin, and A. L. Kholkin, "Electromechanical imaging and spectroscopy of ferroelectric and piezoelectric materials: state of the art and prospects for the future", *J. Am. Ceram. Soc*. 92 1629 (2009).

159. F. Peter, B. Reichenberg, A. Rüdiger, R. Waser and K. Szot, "Sample-tip interaction of piezoresponse force microscopy in ferroelectric nanostructures", *IEEE Trans. Ultrason. Ferroelectr. Freq. Control* 53, 2253 (2006).

160. F. Peter, A. Rüdiger, R. Waser, K. Szot and B. Reichenberg, "Contributions to in-plane piezoresponse on axially symmetrical samples", *Rev. Sci. Instrum*. 76, 106108 (2005).

161. H. N. Bordallo, E. V. Boldyreva, A. Buchsteiner, M. M. Koza and S. Landsgesell, "Structure-property relationships in the crystals of the smallest amino acid: an incoherent inelastic neutron scattering study of the glycine polymorphs", *J. Phys. Chem. B*, 112, 8748 (2008).

162. Y. Iitaka, "The crystal structure of γ-glycine", *Acta Cryst*. 225, 11(1958).

163. P. Lofgren, A. Krozer, J. Lausmaa and B. Kasemo, “Glycine on Pt(111): a TDS and XPS study”, *Surf. Sci.* 370, 277 (1997).

164. X. Y. Zhao and J. Rodriguez, “Photoemission study of glycine adsorption on Cu/Au(1 1 1) interfaces”, *Surf. Sci*. 600, 2113 (2006).

165. S. M. Barlow, K. J. Kitching, S. Haq and N. V. Richardson, “A study of glycine adsorption on a Cu{110} surface using reflection absorption infrared spectroscopy”, *Surf. Sci*. 401, 322 (1998).

166. N. V. Surovtsev, S. V. Adichtchev, V. K. Malinovsky, A. G.Ogienko, V. A. Drebushchak, A. Yu. Manakov, A. I. Ancharov, A. S.Yunoshev and E. V. Boldyreva, “Glycine phases formed from frozen aqueous solutions: revisited”, *J. Chem. Phys*. 137, 65103 (2012).

167. I. S. Lee, K. T. Kim, R. A. Y. Lee and A. S. Myerson, “Concomitant crystallization of Glycine on patterned substrates: the effect of pH on the polymorphic outcome”, *Cryst. Growth Des.* 8, 108 (2008).

168. R. A. Van Santen, “The Ostwald step rule”, *J. Phys. Chem.* 88, 5768 (1984).

169. S. Herminghaus, K. Jacobs, K. Mecke, J. Bischof, A. Fery, M. Ibn-Elhaj and S. Schlagowski, “Spinodal dewetting in liquid crystal and liquid metal films”, *Science* 282, 916 (1998).

170. G. F. Harrington, J. M. Campbell and H. K. Christenson, “Crystal patterns created by rupture of a thin film”, *Cryst. Growth Des*. 13, 5062 (2013).

171. E. S. Ferrari, R. J. Davey, W. I. Cross, A. L. Gillon and C. S. Towler, “Crystallization in polymorphic systems: the solution-mediated transformation of β to α Glycine”, *Cryst. Growth Des*. 3, 53 (2003).

172. B. K. Olmsted and M. D. Ward, “The role of chemical interactions and epitaxy during nucleation of organic crystals on crystalline substrates”, *CrystEngComm*, 13, 1070 (2011).

173. K. H. Ernst and K. Christmann, “The interaction of glycine with a platinum (111) surface”, *Surf. Sci.* 224, 277 (1989).

174. F. Huerta, E. Morallon, F. Cases, A. Rodes, J. L. Vazquez and A. Aldaz, “Electrochemical behaviour of amino acids on Pt(h,k,l): a voltammetric and in situ FTIR Study. Part 1. Glycine on Pt(111)”, *J. Electroanal. Chem*. 421, 179 (1997).

175. Y. Iitaka, “The crystal structure of β-glycine”, *Acta Cryst*. 13, 35 (1960).

176. R. E. Marsh, “A refinement of the crystal structure of glycine”, *Acta Cryst*. 11, 654 (1958).

177. G. Koeckelberghs, C. Samyn, A. Miura, S. De Feyter, F. C. De Schryver, S. Sioncke, T. Verbiest, G. de Schaetzen and A. Persoons, “Polar order in spin-coated films of a regioregular chiral poly[(*S*)-3-(3,7-dimethyloctyl)thiophene]”, *Adv. Mater*. 17(6), 708 (2005).

178. E. Gomar-Nadal, J. Puigmartı´-Luis and D. B. Amabilino, “Assembly of functional molecular nanostructures on surfaces”, *Chem. Soc. Rev*. 37, 490 (2008).

179. P. A. Kralchevsky and N. D. Denkov, “Capillary forces and structuring in layers of colloid particles” *Curr. Opin. Colloid Interface Sci*. 6, 383 (2001).

180. R. Xie, A. Karim, J. F. Douglas, C. C. Han and R. A. Weiss, "Spinodal dewetting of thin polymer films", *Phys. Rev. Lett*. 81, 1251 (1998).

181. B. C. Okerberg, B. C. Berry, T. R. Garvey, J. F. Douglas, A. Karim and C. L. Soles, "Competition between crystallization and dewetting fronts in thin polymer films", *Soft Matter* 5, 562 (2009).

182. X. Zhang and B. L. Weeks, "Effects on the surface structure of organic energetic materials using spin coating", *Thin Solid Films* 550, 135 (2014).

183. S. Lei, E. A. Eliseev, A. N. Morozovska, R. C. Haislmaier, T. T. A. Lummen, W. Cao, S. V. Kalinin and V. Gopalan, "Origin of piezoelectric response under a biased scanning probe microscopy tip across a 180^{o} ferroelectric domain wall", *Phys. Rev. B* 86, 134115 (2012).

184. P. Sharma, D. Wu, S. Poddar, T. J. Reece, S. Ducharme and A. Gruverman, "Orientational imaging in polar polymers by piezoresponse force microscopy", *J. Appl. Phys.* 110, 052010 (2011).

185. R. Nath, S. Hong, J. A. Klug, A. Imre, M. J. Bedzyk, R. S. Katiyar and O. Auciello, "Effects of cantilever buckling on vector piezoresponse force microscopy imaging of ferroelectric domains in $BiFeO_3$ nanostructures", *Appl. Phys. Lett*. 96, 163101 (2010).

186. F. Kagawa, S. Horiuchi, N. Minami, S. Ishibashi, K. Kobayashi, R. Kumai, Y. Murakami and Y. Tokura, "Polarization switching ability dependent on multidomain topology in a uniaxial organic ferroelectric", *Nano Lett*. 14, 239 (2014).

187. E. G. Fesenko, V. G. Gavrilyachenko, M. A. Martinenko, A. F. Semenchov and I. P. Lapin, "Domain structure peculiarities of lead-titanate crystals", *Ferroelectrics* 6, 61 (1973).

188. C. L. Jia, S. B. Mi, K. Urban, I. Vrejoiu, M. Alexe and D. Hesse, "Atomic-scale study of electric dipoles near charged and uncharged domain walls in ferroelectric films", *Nat. Mater*. 7, 57 (2008).

189. E. A. Eliseev, A. N. Morozovska, G. S. Svechnikov, V. Gopalan and V. Ya. Shur, "Static conductivity of charged domain walls in uniaxial ferroelectric semiconductors", *Phys. Rev. B* 83, 235313 (2011).

190. F. Peter, A. Rüdiger, K. Szot, R. Waser and B. Reichenberg, "Sample-tip interaction of piezoresponse force microscopy in ferroelectric nanostructures", *IEEE Trans. Ultrason. Ferroelectr. Freq. Control* 53, 2253 (2006).

191. R. E. Newnham, "Properties of Materials: Anisotropy, Symmetry, Structure", Oxford University Press, Oxford (2005).

192. Ü. Özgür, Ya. I. Alivov, C. Liu, A. Teke, M. A. Reshchikov, S. Doğan, V. Avrutin, S.-J. Cho and H. Morkoç, "A comprehensive review of ZnO materials and devices", *J. Appl. Phys*. 98, 041301 (2005).

193. N. A. Pertsev, R. V. Gainutdinov, Ya. V. Bodnarchuk and T. R. Volk, "Blockage of domain growth by nanoscale heterogeneities in a relaxor ferroelectric $Sr_{0.61}Ba_{0.39}Nb_2O_6$", *J. Appl. Phys.* 117, 034101 (2015).

194. P. Paruch, T. Tybell and J. M. Triscone, "Nanoscale control of ferroelectric polarization and domain size in epitaxial $Pb(Zr_{0.2}Ti_{0.8})O_3$ thin films", *Appl. Phys. Lett*. 79, 530 (2001).

195. N. A. Pertsev, A. Petraru, H. Kohlstedt, R. Waser, I. K. Bdikin, D. Kiselev and A. L. Kholkin, "Dynamics of ferroelectric nanodomains in $BaTiO_3$ epitaxial thin films via piezoresponse force microscopy", *Nanotechnology* 19, 375703 (2008).

196. N. A. Pertsev and A. L. Kholkin, "Subsurface nanodomains with in-plane polarization in uniaxial ferroelectrics via scanning force microscopy", *Phys. Rev.* B 88, 174109 (2013).

197. A. V. Ievlev, D. O. Alikin, A. N. Morozovska, O. V. Varenyuk, E. A. Eliseev, A. L. Kholkin, V. Ya. Shur and S. V. Kalinin, "Symmetry breaking and electrical frustration during tip-induced polarization switching in the nonpolar cut of lithium niobate single crystals", *ACS Nano* 9, 769 (2015).

198. V. Ya. Shur, A. R. Akhmathanov, M. A. Chuvakova and I. S. Baturin, "Polarization reversal and domain kinetics in magnesium doped stoichiometric lithium tantalate", *Appl. Phys. Lett*., 105, 152905 (2014).

199. K. Kobayashi, S. Horiuchi, R. Kumai, F. Kagawa, Y. Murakami and Y. Tokura, "Electronic ferroelectricity in a molecular crystal with large polarization directing antiparallel to ionic displacement", *Phys. Rev. Lett*. 108, 237601 (2012).

200. S. Horiuchi and Y. Tokura, "Organic ferroelectrics", *Nat. Mater*. 7, 357 (2008).

201. S. Horiuchi, F. Kagawa, K. Hatahara, K. Kobayashi, R. Kumai, Y. Murakami and Y. Tokura, "Above-room-temperature ferroelectricity and antiferroelectricity in benzimidazoles", *Nat. Commun.* 3, 1308 (2012).

202. M. Molotskii, A. Agronin, P. Urenski, M. Shvebelman, G. Rosenman and Y. Rosenwaks, "Ferroelectric domain breakdown", *Phys. Rev. Lett*. 90, 107601 (2003).

203. T. R. Volk, R. V. Gainutdinov, Ya. V. Bodnarchuk and L. I. Ivlev, "Creation of domains and domain patterns on the nonpolar surface of $Sr_xBa_{1-x}Nb_2O_6$ crystals by atomic force microscopy", *JETP Lett.* 97, 483 (2013).

204. V. S. Bystrov, E. Seyedhosseini, I. Bdikin, S. Kopyl, S. M. Neumayer, J. Coutinho and A. L. Kholkin, "BioFerroelectricity: Glycine and Thymine nanostructures computational modeling and ferroelectric properties at the nanoscale", *Ferroelectrics* 475, 107 (2015).

205. M. I. Molotskii and M. M. Shvebelman, "Decay of ferroelectric domains formed in the field of an atomic force microscope", *J. Appl. Phys*. 97, 084111 (2005).

206. T. K. Song, J. G. Yoon and S. Kwun, "Microscopic Polarization Retention Properties of Ferroelectric $Pb(Zr,Ti)O_3$ Thin Films", *Ferroelectrics* 335, 61 (2006).

207. HyperChem, Tools for molecular modeling (release 7, 8). Professional edition (2002), Hypercube Inc. Gainesville, FL; http://www.hyper.com/?tabid=360.

208. K. Srinivasan, "Crystal growth of α and γ glycine polymorphs and their polymorphic phase transformations", *J. Cryst. Growth* 311, 156 (2008).

209. E. V. Boldyreva, V. A. Drebushchak, T. N. Drebushchak, I. E. Paukov, Y. A. Kovalevskava and E. S. Shutova, "Polymorphism of glycine, Part I", *J. Therm. Anal. Calorim*. 73, 409 (2003).

210. K. R. Wilson, D. S. Peterka, M. Jimenez-Cruz, S. R. Leone and M. Ahmed, "VUV photoelectron imaging of biological nanoparticles: ionization energy determination of nanophase glycine and phenylalanine-glycine-glycine", *Phys. Chem. Chem. Phys*. 8, 1884 (2006).

211. R. E. Newnham, V. Sundar, R. Yimnirun, J. Su and Q. M. Zhang, "Electrostriction: nonlinear electromechanical coupling in solid dielectrics", *J. Phys. Chem. B.* 101(48), 10141 (1997).

212. G. A. Smolenskii, V. A. Bokov, V. A. Isupov, N. N. Krainik, R. E. Pasynkov, A. I. Sokolov, N. K. Yushin, "Physics of Ferroelectric Phenomena: Ferroelectrics and related materials.", Gordon and Breach, New York (1985). (Leningrad, Nauka, in Russian).

213. R. A. Kumar, R. E. Vizhi, N. Vijayan and D. R. Babu, "Structural, dielectric and piezoelectric properties of nonlinear optical γ-glycine single crystals", *Physica B*. 406, 2594 (2011).

214. J. Zhu, K. Gao, S. Xiao, X. Qiu, H. L. Cai and X. S. Wu, "Relaxation of ferroelectric thin films of diisopropylammonium perchlorate", *Phys Chem Chem Phys*. 17(6), 2015.

215. L. Arizmendi, "Photonic applications of lithium niobate crystals", *Phys. Status Solidi A* 201, 253 (2004).

216. G. Hofmann, N. Neumann and H. Budzier, "Pyroelectric single-element detectors and arrays based on modified TGS", *Ferroelectrics* 133, 41 (1992).

217. R. Pepinsky, K. Vedam, S. Hoshino and Y. Okaya, "Ferroelectricity in Di-Glycine Nitrate $(NH_2CH_2COOH)_2.HNO_3$", *Phys. Rev*. 111, 430 (1958).

218. V. S. Bystrov, E. V. Paramonova, I. K. Bdikin, A. V. Bystrova, R. C. Pullar and A. L. Kholkin, "Molecular modelling of the piezoelectric effect in the ferroelectric polymer poly (vinylidene fluoride) (PVDF)", J. Mol. Mod. 19, 3591 (2013).

219. I. Bdikin, V. Bystrov, I. Delgadillo, J. Gracio, S. Kopyl, M. Wojtas, E. Mishina, A. Sigov and A. L. Kholkin, "Polarization switching and patterning in self-assembled peptide tubular structures", *J. Appl. Phys.* 111, 074104 (2012).

220. R. W. Boyd, "Nonlinear Optics", Academic Press, San Diego, CA. (2003).

221. V. Gopalan and R. Raj, "Domain structure and phase transitions in epitaxial $KNbO_3$ thin films studied by in situ second harmonic generation measurements", *Appl. Phys. Lett*. 68, no10, 1323 (1996).

222. E. D. Mishina, N. E. Sherstyuk, D. R. Barskiy, A. S. Sigov, Yu. I. Golovko, V. M. Mukhorotov, M. De. Santo and Th. Rasing, "Domain orientation in ultrathin *(*$(Ba,Sr)TiO_3$ films measured by optical second harmonic generation", *J. Appl. Phys*. 93, 6216 (2003).

223. V. Gopalan, M. J. Kawas, M. C. Gupta, T. E. Schlesinger and D. D. Stancil, "Integrated quasi-phase-matched second-harmonic generator and electrooptic scanner on $LiTaO_3$ single crystals", *IEEE Photonics Technol. Lett*. 8, 1704 (1996).

224. R. Salem, M. A. Foster, A. C. Turner, G. F. Geraghty, M. Lipson and A. L. Gaeta, "Signal regeneration using low-power four-wave mixing on silicon chip", *Nat. Photonics* 2, 35 (2008).

225. J. Han, J. Li, W. Jia, L. Yao, X. Li, L. Jiang and Y. Tian, "Photothermal therapy of cancer cells using novel hollow gold nanoflowers", *Int. J. Nanomedicine* 9, 517 (2014).

226. D. S. Hum and M. M. Fejer, “Quasi-phasematching”, *C. R. Phys*. 8, 180 (2007).

227. G. Rosenman, P. Urenski, A. Agronin, Y. Rosenwaks and M. Molotskii, “Submicron ferroelectric domain structures tailored by high-voltage scanning probe microscopy”, *Appl. Phys. Lett.* 82, 103 (2003).

List of publications

1. E. Seyedhosseini, M. Ivanov, V. Bystrov, I. Bdikin, P. Zelenovskiy, V. Ya. Shur, A. Kudryavtsev, E. D. Mishina, A. S. Sigov, and A. L. Kholkin; “Growth and nonlinear optical properties of β-glycine crystals grown on Pt substrates”; *Crystal Growth & Design*. 14, 2831 (2014).

2. V. Bystrov, E. Seyedhosseini, S. Kopyl, I. K. Bdikin and A. L. Kholkin; “Piezoelectricity and ferroelectricity in biomaterials: Molecular modeling and piezoresponse force microscopy measurements”; *Journal of Applied Physics*. 116, 066803-1 (2014).

3. D. Isakov, D. Petukhova, S. Vasilev, A. Nuraeva, T. Khazamov, E. Seyedhosseini, P. Zelenovskiy, V. Y. Shur and A .L. Kholkin; “In Situ Observation of the Humidity Controlled Polymorphic Phase Transformation in Glycine Microcrystals”; *Crystal Growth & Design*. 14, 4138 (2014).

4. V. Bystrov, E. Seyedhosseini, I. Bdikin, S. Kopyl, S. M. Neumayer, J. Coutinho and A.L.Kholkin; “Bioferroelectricity in Nanostructured Glycine and Thymine: Molecular Modeling and Ferroelectric Properties at the Nanoscale”; *Ferroelectrics* 475, 107 (2015).

5. E. Seyedhosseini, I. Bdikin, M. Ivanov, D. Vasileva, A. Kudryavtsev, B. J. Rodriguez, A. L. Kholkin, “Tip-induced domain structures and polarization switching in ferroelectric amino acid glycine”; *Journal of Applied Physics*. 118, 072008-1 (2015).

6. E. Seyedhosseini, D. Vasileva, S. Vasilev, A. Nuraeva, P. Zelenovskiy, V. Ya. Shur, and A. L. Kholkin; “Patterning and Nanoscale Characterization of Ferroelectric Amino Acid Beta-glycine”; *IEEE* Conference proceedings*, ISAF-ISIF-PFM* 207, (2015).